MECHANISMS OF
GRAPHITE NOZZLE EROSION IN HYBRID ROCKETS

A Dissertation
Presented to
The Academic Faculty

by

[Landon T. Kamps]

In Partial Fulfillment
of the Requirements for the Degree of
Doctor of Philosophy in the
Graduate School of Engineering

Hokkaido University
September 2019

MECHANISMS OF
GRAPHITE NOZZLE EROSION IN HYBRID ROCKETS

Approved by:

Dr. Harunori Nagata, Advisor
School of Engineering
Hokkaido University

Dr. Nobuyuki Oshima
School of Engineering
Hokkaido University

Dr. Osamu Fujita
School of Engineering
Hokkaido University

Dr. Nozomu Hashimoto
School of Engineering
Hokkaido University

Date Approved: 31st July 2019

[To the students of Hokkaido University]

ACKNOWLEDGEMENTS

This research would not have been possible without the financial and technical support of numerous organizations. These include the Japanese Ministry of Education, Science, Sports, Culture, Grant-in-Aid for Science Research (B) 15H04197 (2016), Grant-in-Aid for the Promotion of Science (JSPS) fellows 18j2087708, the matching fund program of Centers for Inter-University Collaboration from the Institute of Space and Astronautical Science (ISAS/JAXA), a collaborative research partnership with IHI Corporation, and most importantly the generous support and dedication of Tsutomu Uematsu, president of Uematsu Electric Company and co-founder of CAMUI Space Works. Tests conducted at Uematsu Electric Company were expertly managed by Mr. Hikaru Isochi, with technical support from Naoto Adachi and students of Hokkaido University. Large scale tests were designed and planned by Tor Viscor and Mitsunori Itoh of IHI Corporation, as well as Hokkaido University students Ryosuke Kawabata, Shota Hirai and Ryo Yamaguchi. Shota Hirai designed the HK/SLY-series motor, and inspired the design of the DNT-series motor. Yurika Kiyotani, Kazuhito Sakurai and Erika Uchiyama laid the groundwork for the use of nitrous oxide as an oxidizer, and Kazuhito Sakurai designed and led the CBX-series campaign. Yuji Saito was paramount to the development of the comprehensive data reduction method, and a great mentor throughout this research. I owe the success of this research to the immense knowledge and pioneering attitude of Professor Harunori who guided me as my supervisor, and inspired me as a mentor. Lastly, to my wife Sayuri, who supported me with patience and love, thank you.

TABLE OF CONTENTS

LIST OF TABLES

LIST OF FIGURES

LIST OF SYMBOLS AND ABBREVIATIONS

A	=	area, m^2
A,b,E	=	Arrhenius equation constants
a,b,c,d	=	placeholders
CEA	=	functions representative of NASA CEA operations
c_p	=	constant pressure specific heat, J/kg-K
c^*	=	characteristic exhaust velocity, m/s
d	=	diameter, m
D	=	diffusion coefficient, m^2/s
F	=	thrust, N
h	=	convective heat transfer coefficient ("convectivity"), W/m^2-K
k	=	thermal conductivity, W/m-K or heterogenous rate constant
M	=	mass remaining, kg
MW	=	molecular weight
$\dot{m}$	=	mass flow/consumption rate, kg/s
P	=	pressure, Pa
Pr	=	Prandtl number
$\dot{q}$	=	heat flux, W/m^2
R	=	gas constant J/kg-K
R_u	=	universal gas constant, J/kmol-K
r	=	radial position from nozzle centerline, m
Δr	=	radial node spacing in the nozzle mesh, m
$\dot{r}$	=	(nozzle) erosion rate, m/s
Re	=	Reynolds number
Sc	=	Schmidt number
T	=	Temperature, K
t	=	(firing) time, s
Δt	=	time step, s
U	=	uncertainty

x,y	=	arbitrary input, output
α	=	thermal diffusivity, m^2/s
$\beta_1, \beta_2, \beta_3$	=	empirical constants
δ	=	(concentration) boundary layer thickness, m
ε	=	(nozzle) expansion ratio
γ	=	specific heat ratio
η^*	=	characteristic exhaust velocity efficiency
λ	=	thrust correction factor
μ	=	kinematic viscosity, Pa-s
ξ	=	oxidizer-to-fuel-mass ratio
ρ	=	density, kg/m^3
Φ	=	equivalence ratio
Ψ,ψ	=	calculation residual terms
$\bar{}$	=	overbar, to indicate a time-averaged value

Subscripts

a	=	atmospheric
b	=	burn (time)
c	=	chamber position
calc,meas	=	distinguishes a calculated value or a measured value
e	=	nozzle exit plane position
f	=	final
fu	=	fuel
i	=	oxidizing species index, or radial node index
j	=	reaction index, or time index
n	=	nozzle
n1,n2,n3	=	thermocouple positions within the nozzle
o	=	initial
on	=	onset (of nozzle erosion)
ox	=	oxidizer, or sum of oxidizing species
t	=	nozzle throat plane position
th	=	theoretical value

w	=	nozzle throat wall position
δ	=	(concentration) boundary layer surface position

Acronyms

AIEB	=	Axial-Injection End-Burning
CAMUI	=	Cascaded Multistage Impinging-jet
CDR	=	Comprehensive Data Reduction
CEA	=	(NASA) Chemical Equilibrium with Applications
GFRP	=	Glass Fiber-Reinforced Plastic
GOX	=	Gaseous Oxygen
GTO	=	Geostationary Transfer Orbit
HDPE	=	High-Density Polyethylene
HRM	=	Hybrid Rocket Motor
IA	=	IHI Aerospace Company (Japan)
ISAS	=	Institute of Space and Astronautical Science (Japan)
JAXA	=	Japan Aerospace Exploration Agency
LOX	=	Liquid Oxygen
NASA	=	National Aeronautics and Space Administration (USA)
NIST	=	National Institute of Standards and Technology (USA)
NTRT	=	Nozzle Throat Reconstruction Technique
PMMA	=	Polymethyl Methacrylate
SRM	=	Solid Rocket Motor
TTRT	=	Throat Temperature Reconstruction Technique

SUMMARY

This study elucidates the mechanisms of thermochemical erosion in hybrid rocket nozzles for the first time by analyzing data from 60 hybrid rocket firing tests at various scales and thrust classes ranging from motors that are 50 mm to 300 mm in diameter at thrusts from 10 N to 2,000 N, respectively. This was only possible through the development and validation of a new data reduction methodology that enabled the determination of time-resolved nozzle throat erosion, oxidizer-to-fuel-mass ratio, and nozzle throat wall temperature from measurements of thrust, chamber pressure, oxidizer mass flow rate, overall fuel mass consumption, final nozzle throat diameter, and two thermocouple measurements from within the nozzle body. Empirical analysis led to the formulation of a predictive model for nozzle erosion rate based on heterogeneous combustion theory and turbulent mass transport theory. This work is introduced in the following six chapters: (1) Nozzle Erosion in Chemical Rockets; (2) Model of Chemical Erosion; (3) Comprehensive Data Reduction; (4) Hybrid Rocket Motor Operation; (5) Static Firing Test Results; (6) Impact on Hybrid Rocket Development; and ends with Concluding Remarks.

CHAPTER 1. NOZZLE EROSION IN CHEMICAL ROCKETS

Nozzle erosion is the deterioration and regression of the surface of a nozzle due to oxidizing (chemical) reactions with, and/or physical abrasion by condensed phase particles contained within the combustion gas flowing over it. The use of the term "erosion" may be misleading because in other context erosion is a gradual, often mechanical, removal of solid material from an object within a fluid flow. The polishing of a stone in a river bed or the deepening of a canyon by the flow of a river come to mind as more commonplace examples of erosion. In chemical rockets, the erosion of the nozzle surface is rapid, intense, and, depending on the internal ballistic conditions of the rocket, more so the result of chemical reactions than physical abrasion by the combustion gas flow. Nonetheless, the term "erosion" has been widely used as a generalization of the nozzle surface regression phenomena observed during the operation of a chemical rocket. When erosion is primarily the result of chemical reactions it is referred to as "chemical" erosion or "thermochemical" erosion. When erosion is primarily the result of physical abrasion of liquid or solid phase particles in the combustion gas, it is referred to as "mechanical" erosion.

1.1 Thermal Management of Chemical Rocket Nozzles

Chemical rocket nozzles are converging-diverging ducts shaped to convert the internal energy of high-pressure combustion gas to kinetic energy. A simplified depiction of a combustion chamber and nozzle is shown in Figure 1. Gas accelerates from a low velocity in the chamber to the speed of sound at the nozzle throat, the bridge between converging and diverging sections, and beyond the speed of sound in the diverging section. Bartz demonstrated experimentally in the late 1950s and early 1960s that the convective

heat transfer coefficient, h [W/m^2-K], in a chemical rocket nozzle is maximum at the nozzle throat where it generally reaches values on the order of ~10^4 W/m^2-K [1][2]. The adiabatic flame temperature of common chemical rocket propellant combinations is upwards of 3500 K, and the temperature decrease between the combustion chamber and the nozzle throat is usually less than 20% (i.e. less than 700 K), such that heat flux, $\dot{q}$ [W/m^2], can reach values on the order of ~10^7 W/m^2.

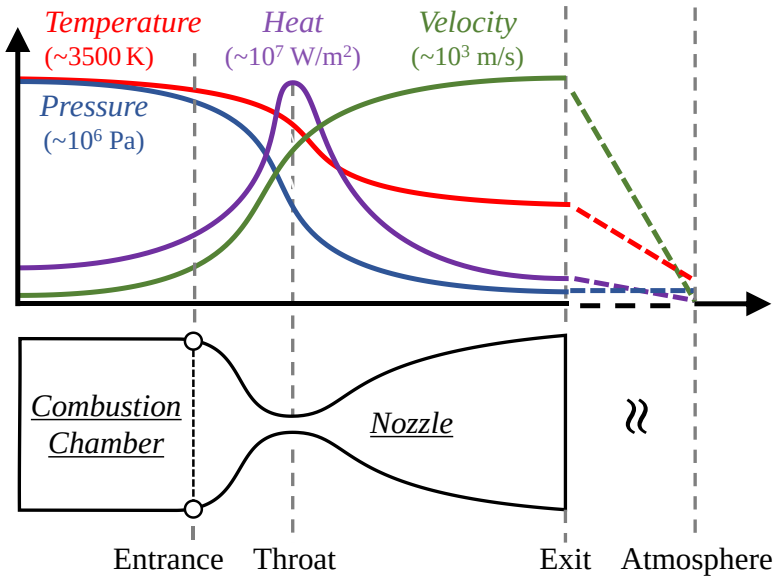

Figure 1. Conversion of internal energy to kinetic energy in a rocket nozzle.

Sutton and Biblarz summarized the most common approaches to dealing with the high heat transfer rates observed in chemical rocket combustion chambers in two categories: "steady-state" and "transient" heat transfer methods, and consider film-cooling as an "auxiliary" method [3](pp. 289). Steady-state methods include convective cooling using a coolant, and radiation cooling to the surroundings. Transient methods include heat storage in the chamber material itself, and the use of ablative materials that are consumed

away during operation. The scale, operating time, payload restrictions, and internal ballistic conditions of the rocket affect what defines the best thermal management method. At the nozzle throat, where heat transfer rate is largest, regenerative cooling is the most feasible steady-state method and ablative cooling is the most feasible transient method.

The use of an ablative material in the nozzle is synonymous with nozzle erosion. Nozzle erosion is used in a negative context, referring to the degradation of the nozzle resulting in a loss of rocket performance. The term ablative cooling is used when nozzle erosion is accepted as a necessary loss for the preservation of the combustion chamber. Thus, the premise underlying this study is that nozzle erosion is the unavoidable consequence of rocket designs that use ablative cooling to manage thermal loads at the nozzle. Note that when an ablative is used upstream of the nozzle to invade the boundary layer at the nozzle entrance with cooler, less erosive product gas, this is considered "film cooling." As suggested by Sutton and Biblarz in [3], film cooling is an auxiliary method that is easily implemented in conjunction with regenerative cooling and ablative cooling.

1.1.1 Regenerative Cooling of Liquid Rocket Nozzles

Liquid rockets have the option of using regenerative cooling because one of the propellants, usually the fuel, can be passed through cooling channels that encase the nozzle throat prior to being supplied to the combustion chamber. According to a recent report by Kato et al., regenerative cooling is still the most common thermal management technique in leading commercial liquid rocket engines, including the largely successful Raptor engine of SpaceX [3]. Two exceptions are the LE-8 and 30kN-class liquid rockets currently being developed by IHI Aerospace Co., Ltd. (IA), which employ ablative cooling even though

regenerative cooling is a technically feasible alternative. Seeing that IA has been Japan's primary solid rocket manufacturer, the reason for the use of ablative cooling even though regenerative cooling was a reasonable alternative may be matters of (technological) heritage and cost-reduction through technology transfer within the company.

Most operational liquid rockets are regeneratively cooled by the fuel, rather than the oxidizer. The two reasons the fuel is used as the coolant over the oxidizer is that most fuels have a higher heat capacity than the oxidizers they are paired with, and fuels have very little risk of chemical interaction with the components of the feed system. In short, there is no added benefit to using the oxidizer over the fuel, whereas there is an added risk of corrosion and/or explosion within the feed system. The particulars of this tradeoff came into focus in previous research by Price [4]. Price conducted experimental investigations of regenerative cooling using liquid oxygen (LOX) as the coolant in LOX/RP-1 rocket engines with the aim of improving regenerative cooling. The motivation for running trials with LOX was that when RP-1 was used as the coolant, carbon "coke" formed along the surface of the cooling channels reducing the heat transfer efficiency and increasing the risk of thermal failure at the throat. It is not clear if similar issues have been observed in other cases. In his report, Price expressed concern over the potential hazard of LOX leaking through cracks that form in the combustion chamber and react with fuel (soot) films near the inner chamber wall when hydrocarbons such as RP-1 are used as fuel, although this was not an issue in his initial trials. Follow-on research by Price and Masters [5], and later by Armstrong [6] and Yuasa et al. [7], concluded that LOX could safely be used as the coolant for regenerative cooling even in liquid rockets using hydrocarbon fuels such as RP-1.

1.1.2 Mechanical Failure in Erosion-Resistant Nozzles

Regenerative cooling is not an option for solid rockets because the propellants are stored within the combustion chamber in the solid phase. Whereas high-conductivity copper serves as a universally adopted throat liner for regeneratively cooled nozzles, there is no material parallel in the case where no regenerative cooling is used. If there was a light-weight, anti-erosion, material capable of handling the thermal stress at the throat, solid rockets may not need to be "cooled" at all. Unfortunately, no such material has been discovered yet. In early deliberations, ceramics and refractory metals showed promise for their resistance to erosion and high melting temperatures. Olcott and Bachelor revealed that dense tungsten alloys are highly resistant to chemical erosion and demonstrate satisfactory resistance to thermal stress [8]. However, concurrent work by Johnston et al. lasting several years, in which an extensive inventory of refractory metals, refractory metal-carbines, graphites, ceramics, cermets, and fiber-reinforced plastics were tested as nozzle throat inserts in three distinct sub-scale solid rocket motors, revealed that no one material was best suited for all conditions [9]. The refractory metals and refractory compounds (i.e. metal-carbides, cermets and ceramics) were resistant to chemical erosion, but either melted or failed mechanically due to abrasion and thermal stress fractures, whereas the graphites and plastics were susceptible to chemical erosion. It is important to state that thermal-stress cracking occurred in all refractory compounds, but the nozzles remained in place and intact during operation.

Klopp summarized the major categories of materials available for use at the nozzle throat when regenerative cooling is not used in [10]. Figure 2 depicts these trade-offs, primarily in terms of the required operating pressure and size of the rocket under

consideration. Carbon-based compounds are suitable for use at the throat because they can bear the pressure, thermal gradients and temperatures under most circumstances. In special cases, such as in tactical missiles etc., very high pressures must be endured for a short duration, in which case refractory metals are more adept to handle the mechanical and thermal loads at the throat. At scales so large that nozzle erosion leads to negligible changes to nozzle throat area, erosion-prone materials such as fiber-reinforced plastics are the most economically feasible.

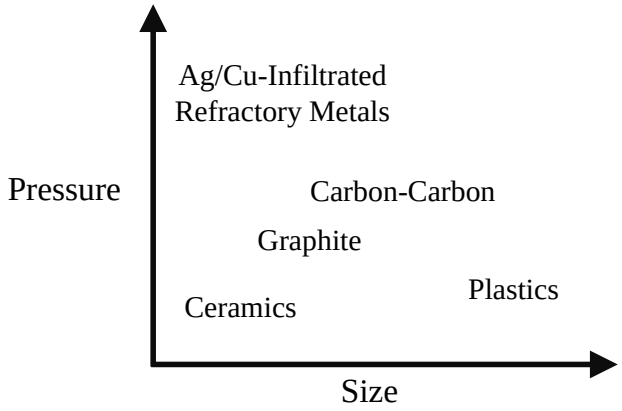

Figure 2. Material selection for the nozzle throat based on pressure and size.

1.1.3 Nozzle Erosion as Ablative Cooling in Solid Rocket Nozzles

Currently, the materials most commonly used at the nozzle throat in solid rockets are carbon-based, i.e. graphite, carbon-carbon, carbon phenolic etc. The main drawback of such materials is that they are prone to chemical erosion/oxidation [11](pp. 209). This is why, as Sutton and Biblarz state [3](pp. 567), “Almost all solid rocket nozzles are ablatively cooled.” In retrospect, the decision to move forward with ablatively cooled nozzles was a necessary compromise given that no reasonable alternative anti-erosion material was on the shelf.

Shortly after carbon-based compounds were adopted as the primary material of choice for the nozzle throat, Parks and Bailey proposed a way to reduce solid rocket development and operation costs through the refurbishment of ablative nozzles for reuse between firings [12]. A decade later, as part of the Alternate Nozzle Ablative Materials Program at NASA Marshall Space Flight Center and the Jet Propulsion Laboratory [13], Powers and Bailey reported the results of five firing tests that included 20 alternative carbon phenolic materials for various sections of the nozzle under consideration for use in the space shuttle solid rocket booster [14]. They concluded that Fiberite K411 Staple PAN, a graphite form carbon phenolic, is best for the nozzle throat, which in their studies had an erosion rate of only 0.05 mm/s at a chamber pressure of 6 MPa. The erosion rate of the other nine materials tested at the throat ranged from 0.09 mm/s to 0.4 mm/s.

1.1.4 Considerations for the Thermal Management of Hybrid Rocket Nozzles

In the 20th century, hybrid rockets were the subject of numerous research and development projects [15], however the focus of the chemical rocket industry as a whole was mostly split between liquid rockets and solid rockets. As a result, hybrid rocket projects were often limited to small-scale testing, with a focus on the fundamental phenomena of hybrid rocket combustion. Nozzle erosion and other topics related to the thermal management of hybrid rocket nozzles are known to be topics of importance to the success of hybrid rockets, as listed by the late Professor Kenneth Kuo in his discussion of "Major Challenges in Hybrid Rocket Propulsion" in [16], but little work has been dedicated to addressing these issues.

In a hybrid rocket, one of the propellants is supplied to the combustion chamber as a gas or liquid droplet stream and the other propellant is stored in the combustion chamber as a solid. All major commercial hybrid rockets currently under development supply the oxidizer as the liquid and the fuel as the solid. Thus, regenerative cooling in the traditional sense, using a liquid fuel as the coolant, is not an option. The studies by Price, Price and Bailey, Armstrong, and Yuasa et al. introduced in Section 1.1.1 (see [4]-[7]) on the use of LOX as a coolant demonstrate that it is technically feasible to use liquid oxidizers as the coolant, but there are no examples of this being done in practice.

In the absence of industry-proven regenerative cooling systems that use liquid oxidizers as the coolant, hybrid rocket developers, with a few exceptions, adopted ablative nozzle designs from solid rockets. One exception is the 1U CubeSat (100 mm cube) hybrid rocket thruster designed and patented by Eilers et al., which uses liquid nitrous oxide (N_2O) as the oxidizer and nozzle coolant in an annular plug nozzle [17]. Quigley and Lyne also recently developed and tested a 3D-printed liquid-cooled nozzle design [18]. Their demonstration of the successful use of 3D printing for the manufacture of liquid-cooled hybrid rocket nozzles is invaluable, however they used water as their coolant and air as the oxidizer, meaning that the adiabatic flame temperature was much lower than in a typical hybrid rocket and regenerative cooling was not an option. Several years prior to Eilers et al.'s thruster design, Lemieux demonstrated experimentally that liquid nitrous oxide has an adequate cooling capability for small-scale hybrid rockets nozzles [19]. Most recently, Ercole et al. applied Lemieux's findings in the preliminary design of the spike for a N_2O-cooled aerospike nozzle design [20]. Kumar et al. also reported on the improved cooling

capability of supercritical N_2O versus saturated N_2O in hybrid rocket applications [21], but have not made any working verification of their predictions.

Outside of these specific examples, hybrid rocket developers have been using nozzles made of carbon-based materials. In this sense, hybrid rockets greatly benefited from the extensive work on solid rockets. Unfortunately, the most common hybrid rocket-propellant combinations contain higher concentrations of oxidizing species than the typical solid rocket, amplifying the severity of chemical nozzle erosion. Bianchi and Nasuti show this in a numerical investigation of graphite nozzle erosion under common hybrid rocket propellant combinations, concluding that erosion rates may range from 0.05 mm/s when using N_2O as oxidizer to 0.12 mm/s when using LOX (at 1 MPa), where the erosion rate in a comparable solid rocket would be less than 0.04 mm/s [22]. The reason that the erosion rate is reduced when using N_2O as the oxidizer versus LOX, is that the presence of (inert) nitrogen in the combustion gas of N_2O and a hydrocarbon dilutes the concentrations of the oxidizing species. The mechanisms of these chemical interactions are the main topic of this research and will be discussed in detail throughout.

Before moving on, it is worth discussing regenerative, ablative and film cooling techniques as applied to the case of hybrid rockets. Figure 3 depicts a generalized hybrid rocket design with and without regenerative cooling. If regenerative cooling is not employed, a large carbon-based nozzle insert is necessary to allow for chemical erosion to take place. If regenerative cooling is employed in the traditional sense, the nozzle wall will be made of tubular channels for oxidizer to flow through, and the interface at the nozzle throat will be a high-conductivity metal, such as (oxygen-free) copper, which is labelled "*Conventional*," in Figure 3. The nozzle throat design labelled "*New Concept*" is a

combination of regenerative and ablative cooling. This type of cooling has not been introduced in open literature, but seems like an appropriate compromise if the oxidizer fails to match the cooling performance of liquid rocket fuels. Film cooling by a cool burning insulator can be applied to either case as is shown in the figure. Given that film cooling techniques have been applied to both liquid and solid rockets in the past, it is reasonable to expect that similar techniques will be viable for hybrid rockets as well.

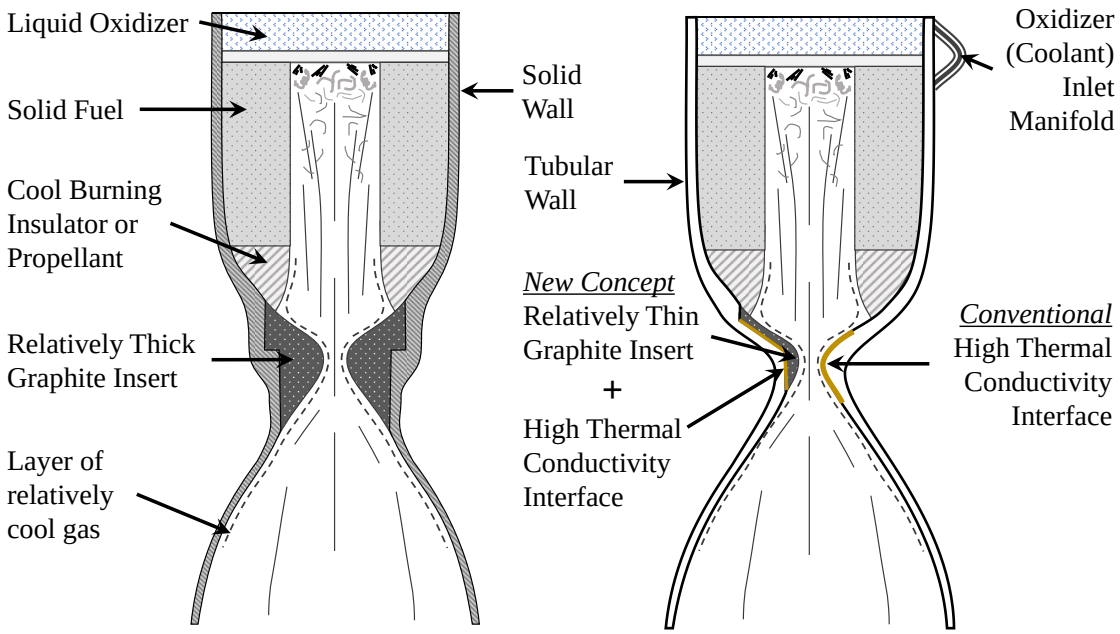

Figure 3. Thermal management concepts for (left) uncooled hybrid rocket nozzle, (right) regeneratively cooled hybrid rocket nozzles.

1.2 Impact of Nozzle Erosion on Rocket Performance

For a given propellant flow rate, $\dot{m}$ [kg/s], and characteristic exhaust velocity, c^* [m/s], nozzle throat erosion, i.e. an increase in the nozzle throat cross-sectional area, A_t [m^2], results in a decrease in chamber pressure, P_c [Pa]. Characteristic exhaust velocity is a fictional velocity that represents the energy conversion potential of the combustion gas. It is defined by a fictional momentum balance between the pressure force acting on the wall opposite the nozzle throat opening and the velocity at which combustion gas would exit from the nozzle if the pressure at the throat was zero. This balance is depicted in Figure 4, and captured by Eq. (1-1):

$$P_c = \dot{m}c^* / A_t \tag{1-1}$$

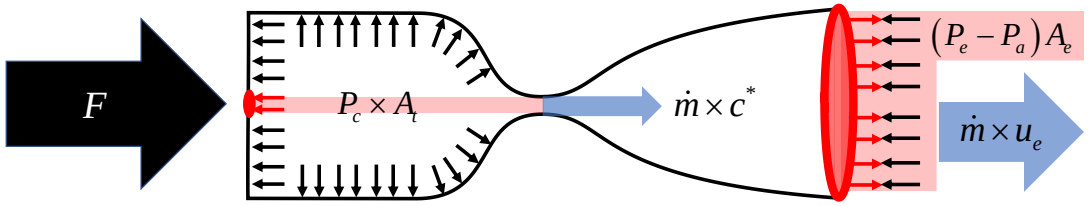

Figure 4. Momentum balance of a rocket nozzle. ***pressure forces in red and momentum forces in blue; note: c* momentum is fictional.***

It is important to point out that the theoretical value for c^* is a function of the combustion gas constant, R [J/kg-K], (stagnation) chamber temperature, T_c [K], and specific heat ratio, γ, according to Eq (1-2):

$$c_{th}^{*} = \sqrt{\frac{RT_c}{\gamma}\left(\frac{\gamma+1}{2}\right)^{\frac{\gamma+1}{\gamma-1}}} = CEA(\xi, P_c) \approx CEA(\xi) \tag{1-2}$$

where the subscript "th" designates this as a "theoretical" value for c^*. The combustion gas properties R, T_c, and γ are determined by the chemical equilibrium composition of combustion gas. In this research, chemical equilibrium calculations are carried out using the NASA Chemical Equilibrium with Applications computer program, denoted by *CEA* in Eq. (1-2) [23]. The dependency of the equilibrium composition of the combustion gas on P_c is negligibly small, meaning that the decrease in P_c that results from nozzle erosion does not directly cause a change in c^*. The thrust, F [N], will be affected by the decrease in P_c and reduction in the expansion ratio of the nozzle, ε, which is the ratio of nozzle exit area, A_e [m^2], to the nozzle throat area. The momentum balance that describes F is also depicted in Figure 4, and captured by Eq (1-3):

$$F = \lambda \dot{m} u_e + \left(P_e - P_a\right) A_e \tag{1-3}$$

where λ is an empirical correction factor that accounts for non-isentropicity of gas expansion in the diverging section of the nozzle, as well as the axial-direction momentum losses due to friction and two-dimensional flow of gas at the nozzle exit. The term P_e is the nozzle exit pressure in pascals, and the term P_a is the surrounding atmospheric pressure in Pa. In a vacuum P_a is zero. The term u_e is the nozzle exit velocity in m/s, and is determined by Eq. (1-4):

$$u_e = c^* \sqrt{\frac{2\gamma^2}{\gamma-1}\left(\frac{2}{\gamma+1}\right)^{\frac{\gamma+1}{\gamma-1}}\left(1-\left(\frac{P_e}{P_c}\right)^{\frac{\gamma-1}{\gamma}}\right)} \tag{1-4}$$

The nozzle exit pressure is a function of ε according to Eq. (1-4):

$$\left(\frac{P_e}{P_c}\right)^{\frac{1}{\gamma}}\left(\frac{\gamma+1}{2}\right)^{\frac{1}{\gamma-1}}\sqrt{\frac{\gamma+1}{\gamma-1}\left(1-\left(\frac{P_e}{P_c}\right)^{\frac{\gamma-1}{\gamma}}\right)} = \frac{1}{\varepsilon} = \frac{A_t}{A_e} \tag{1-5}$$

To gain an understanding of the effect that nozzle erosion has on the nominal performance of a rocket, it is important to consider the secondary effects of the P_c decrease (that results from erosion according to Eq. (1-1)) on the propellant mass consumption rate $\dot{m}$. These secondary effects depend on the type of rocket under consideration. Three representative cases are introduced in Table 1: a solid rocket motor (SRM), axial-injection end-burning (AIEB) hybrid rocket motor, and a conventional hybrid rocket (HRM). If we assume values for λ, P_a, and A_e of 1, 0 Pa, and 0.00785 m^2, respectively, and a nozzle throat erosion rate, $\dot{r}_t$ of 0.00005 m/s (i.e. 0.05 mm/s), we can solve the system of equations (1-1) to (1-5) and numerically integrate for nozzle throat diameter, d_t [m], in time.

The results for specific impulse, I_{sp} s, and P_c for a 100 s burn are plotted in Figure 5. In all three cases nozzle erosion leads to decreases in P_c and I_{sp}, both of which are detrimental to the success of a chemical rocket. However, the severity of the performance decrease varies between cases. The SRM has the smallest percentage decrease in I_{sp} at just under 6% the initial value, but the largest decrease in P_c at more than 95%. In the SRM, any decrease in I_{sp} is solely the result of a decrease in the effectiveness of the expansion of

gas beyond the nozzle throat because ξ (i.e. c^*) is fixed. The HRM has the second smallest decrease in I_{sp} at just over 7%, and the smallest decrease in P_c at 65%. The slightly larger loss in I_{sp} than in the SRM case is due to a minor shift in ξ away from the optimal value. In a conventional HRM, the oxidizer mass flow rate, $\dot{m}_{ox}$ [kg/s], depends on the pressure drop across the injector, which will increase with a decrease in P_c due to nozzle erosion. Thus, erosion leads to a larger $\dot{m}_{ox}$, which in turn leads to a recovery of P_c, and increase in fuel mass consumption, $\dot{m}_{fu}$ [kg/s]. The AIEB has the largest decrease in I_{sp} at 50%, due to the large deviation from the optimal ξ. In the AIEB, the oxidizer is a choked flow, meaning that erosion will not lead to an increase in $\dot{m}_{ox}$. When $\dot{m}_{fu}$ decreases due to a decrease in P_c, the value of ξ increases by the inverse of that decrease. Overall, the conventional hybrid rocket fairs the best in the face of nozzle erosion.

Table 1. Propellant mass flow rate dependencies on P_c for plots in Figure 5.

Figure 5 Designation	Description	Mass Flow Rate Dependencies*	Equilibrium Gas Properties**
SRM	Constant burning surface area (e.g. star grain) solid rocket	$\dot{m} = aP_c^n$ $= \left(2.52\times10^{-5}\right)P_c^{0.6}$	$\gamma, c^* =$ constant $\rightarrow 1.2,\ 1600$ m/s
AIEB	Axial-injection End-burning hybrid rocket. Oxidizer: GOX Fuel: Polyethylene	$\dot{m}_{fu} = aP_c^n$ $= \left(1.36\times10^{-8}\right)P_c$ $\dot{m}_{ox} =$ constant $= 0.1794$ kg/s	$\gamma, c^* = CEA\left(\xi, P_c\right)$ $CEA\left(2, 6\text{ MPa}\right)$ $\rightarrow 1.18,\ 1781$ m/s
HRM	Conventional hybrid rocket: Oxidizer: LOX Fuel: Polyethylene	$\dot{m}_{fu} = a\dot{m}_{ox}^n$ $= \left(0.322\right)\dot{m}_{ox}^{0.8}$ $\dot{m}_{ox} = c_v\sqrt{P_{up} - P_c}$ $= \left(0.322\right)\sqrt{10^7 - P_c}$	$CEA\left(3, 6\text{ MPa}\right)$ $\rightarrow 1.13,\ 1759$ m/s $CEA\left(4, 6\text{ MPa}\right)$ $\rightarrow 1.13,\ 1671$ m/s

* $\dot{m} = \dot{m}_{fu} + \dot{m}_{ox}$, where subscripts "fu" and "ox" stand for "fuel" "oxidizer"

** $\xi = \dot{m}_{ox}/\dot{m}_{fu}$ and c^* is taken to be the theoretical value (see Eq. (1-2))

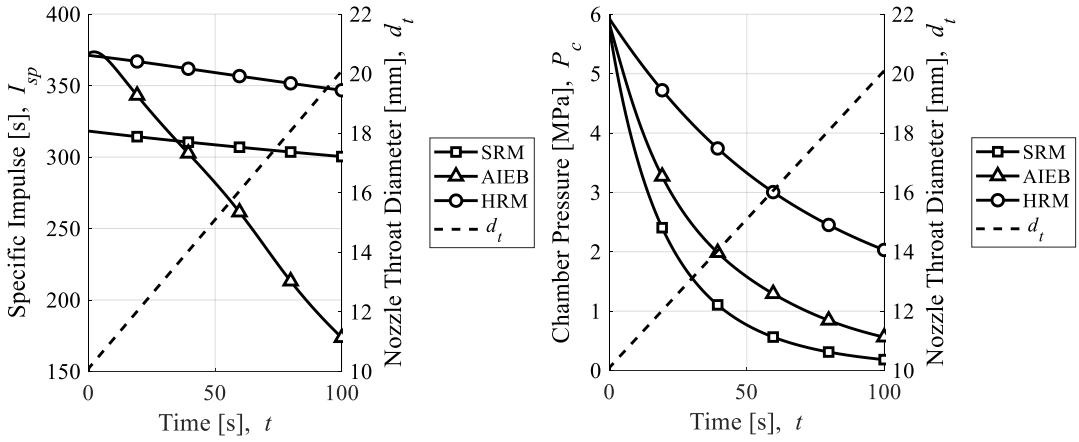

Figure 5. Effect of nozzle throat erosion on (left) the I_{sp} and (right) the P_c of three types of chemical rockets.

1.3 Review of Research on the Chemical Erosion of Graphite Nozzles

Previous research confirms that the erosion of the throat is predominantly chemical in nature, even when erosion elsewhere along the nozzle surface is mechanical. This may be inferred intuitively, because in a converging-diverging nozzle the throat is the location where the contour of the nozzle wall is parallel to the flow direction and the flow is moving near the speed of sound. Thus, even if abrasive particles exist in the combustion gas, only particles that enter the boundary layer will be driven to collide with the nozzle wall, and this collision will be not be head-on. For these reasons, chemical erosion has remained the focus of previous research, and the term "nozzle erosion" in this research will by default refer to nozzle "chemical erosion" unless otherwise specified.

The foundation of research on nozzle erosion can be thought of as starting in the mid-20th century by two separate groups of researchers. Meyer [24], Strickland-Constable [25][26], and Binford and Erying [27], examined the oxidation of carbon samples in chambers containing high temperature CO_2, O_2, N_2O and H_2O vapor. Their research documents the rates of oxidation in ambient conditions, and includes analysis of the Arrhenius constants for activation energy and reaction order. Roughly two decades later three papers that focused on the erosion of graphite nozzle inserts in solid rockets based on diffusion and chemical kinetic theory were published by: Delaney et al. [28], McDonald and Hedman [29], and Mayberry et al. [30]. The analytical model introduced in CHAPTER 2 of this thesis is essentially an extension of Delaney et al.'s model in [28], which in the greater context of current combustion theory would be referred to as a "one-film model," referring to [31] (pp. 532). McDonald and Hedman analyze the chemical-kinetic-limited and diffusion-limited erosion rates of graphite separately, and bridge the two with the

electrical circuit analog. Mayberry et al. carry out a purely empirical correlation based on key non-dimensional parameters from transport theory, including: Sherwood number, Sh, as non-dimensional erosion rate, Reynolds Number, Re, and Schmidt Number, Sc, as the main dependent variables, and Fourier Number, Fo, and blowing number as scaling parameters. Each of these studies shows some agreement between the model proposed and the overall nozzle erosion observed in static firing tests of solid rockets, however, the number of curve fitting constants that were adjusted for correlation were proportionally large given the limited number of firing test data available. For example, in [30] Mayberry et al. use the least squares method to determine 9 fitting constants with only 40 data.

In the 1980s, Keswani et al. [32], and Jones et al. [33], conducted experimental firing tests using solid rocket motors and reported empirical correlations of the form $\dot{r}_t \propto X_i P^n$, where the subscript X_i represents the mole fraction of oxidizing species (such as H_2O, O_2 etc.), and the pressure exponent is $0.8 < n < 1$. In these reports it is not clear if the timing of the onset of erosion was predicted because time histories of the erosion progression are not postulated, but the form of the empirical correlation suggests that this is not possible. In many cases the chamber pressure reaches its design value seconds before erosion begins, meaning that these models would overestimate the erosion rate for these times. Borie et al. conducted three static firing tests using solid rocket motors and modeled the erosion rates according to the electrical circuit analog [34]. In their study, the progression of erosion could be inferred from the increase in throat diameter between the tests because the combustion time increased between tests and the shortest test had nearly no erosion. The electrical circuit analog captured the temperature dependency of the Arrhenius equation

which meant that times of negligibly small erosion were predicted in the beginning of firing, however the predicted erosion onset time was earlier than the measured value.

In the 2000s, Acharya and Kuo [35], and Thakre and Yang [36], conducted numerical analysis of graphite nozzle erosion using computational fluid dynamics techniques. Acharya and Kuo reconstructed the throat erosion history of two static firing tests of different propellent compositions through measurements of pressure and thrust, and compared the results of their numerical model to these histories. They found a relatively good agreement with one solid rocket propellant, but not the other. Thakre and Yang compared their numerical predictions against Borie et al.'s results in [34], and observed a similar level of agreement to the original electrical circuit analog model, slightly overestimating the rate and timing of the onset of erosion. A few years later, Bianchi et al. conducted a detailed numerical analysis of solid rocket static firing tests conducted by Geisler et al. [37]. They conclude that the throat erosion rate of a nonmetallized propellant is predominately the result of chemical reactions with H_2O in the combustion gas. The mass fraction of H_2O in the combustion gas, Y_{H_2O}, decreased five-fold, from 15% to 3%, with only a two-fold increase in Al content, from 15% to 27%. This decrease in Y_{H_2O} correlates with the observed decrease in erosion rate at the throat from 0.35 mm/s (for 15% Al) to 0.07 mm/s for (27% Al). Furthermore, the numerical analysis program predicted the time-averaged regression rates of five of Geisler et al.'s tests to within 4%.

The only work known to the authors that investigates graphite nozzle erosion in hybrid rocket combustion gas is a follow-on work to [37], by Bianchi and Nasuti [22]. Here, the numerical model that was validated in [37] was used to predict erosion rates for

the 12 hybrid rocket propellant combinations that result from forming pairs out of the three fuels: Hydroxyl-terminated Polybutadiene (HTPB), Polyethylene (PE) and wax; and four oxidizers: oxygen (O_2), nitrogen tetroxide (N_2O_4), hydrogen peroxide (H_2O_2), and nitrous oxide (N_2O). Unlike in a solid rocket, which has a fixed propellant composition, in a hybrid rocket the oxidizer-to-fuel-mass ratio, ξ, changes in time. This makes the prediction of nozzle erosion in hybrid rockets even more demanding than in the case of solid rockets. The results of [22] greatly elucidate the major trends in chemical erosion that can be expected in hybrid rockets. First, Bianchi et al. report that erosion rates should have a global maximum in slightly oxidizer-rich conditions, in the region of equivalence ratio, $0.6 < \Phi < 1$. This is a region where adiabatic flame temperature is close to its maximum value while there is also a relatively high mass fraction of the oxidizing species CO_2, H_2O and O_2. The mass fraction of oxidizing species will continue to increase as Φ decreases, however the flame temperature will sharply decrease, driving down the erosion rate. The opposite happens with increasing Φ. The maximum flame temperature is expected in the region $1 < \Phi < 1.2$, and for values of Φ greater than this region the mass fraction of oxidizing species is many times lower than when $\Phi < 1$. Lastly, Bianchi et al. show that the erosion rate of any of the 12 hybrid rocket propellant combinations is greater than that expected of a conventional solid rocket propellant. The reason for this being that the mass fraction of oxidizing species is larger in the hybrid rocket propellant combustion gas. Furthermore, when O_2 is used as the oxidizer the erosion rate is expected to be roughly twice as high as that when using N_2O as the oxidizer. The erosion rates when using N_2O_4 or H_2O_2 as the oxidizer fall in between these extremes. The fuel selection is expected to have very little influence on erosion rate.

The most recent research on graphite nozzle erosion was conducted by Kamps et al. partly in collaboration with Bianchi et al. Kamps et al. developed an innovative measurement technique for determining the histories of d_t and ξ in hybrid rocket static firing tests from the commonly measured values F, P_c, $\dot{m}_{ox}$, Δm_{fu} and Δd_t [38]. The results agreed well with the prediction by Bianchi et al. in [22]. A maximum erosion rate was observed in slightly oxidizer rich conditions, and erosion rate increased linearly with chamber pressure. A joint paper in which Bianchi et al.'s numerical model was applied to Kamps et al.'s static firing tests revealed a general agreement in time-averaged erosion rates, but a disagreement in temporal changes in erosion rate [39]. The reason for this discrepancy was most likely the result of the assumption in Bianchi et al.'s model that the nozzle temperature was steady-state, even though, due to the short duration of firing tests conducted, the nozzle temperature was increasing rapidly in time.

1.4 The Contributions of this Research to Understanding Nozzle Erosion

The effect that nozzle erosion has on the performance of a rocket depends on the type of rocket under consideration. In solid rockets, propellants often contain significant weight percentages of metals, such as Al, that form oxides in the combustion gas and reduce the concentration of oxidizing species, reducing the severity of thermochemical erosion. However, the impact that nozzle erosion has on performance is more pronounced, because propellant mass flow rate depends on the chamber pressure, which decreases with nozzle throat erosion. In hybrid rockets, the oxidizer is supplied to the chamber as a gas or droplet stream, and fuel is stored within the combustion chamber as a solid. The impact that nozzle erosion has on performance is reduced because propellant mass flow rate is only partially

dependent on chamber pressure, however nozzle erosion is more severe because the combustion gas tends to contain high concentrations of oxidizing species.

Small studies conducted over the past five decades have established models for predicting nozzle erosion, however the number of data and range of conditions tested for was limited. The cost of experimentation is high, and when using solid rockets to test for erosion, the range of propellant combinations that can be tested is limited by the number of separate fuel grains that can be produced and fired. One large discrepancy in the body of previous research is the lack of time-resolved erosion analysis. Exceptions to this are the work previously introduced as [35], as well as the doctoral work conducted by Evans [40]. The most extensive collection of time-resolved erosion histories in previous research probably belongs to Evans, who used X-ray radiography to record the throat erosion history of dozens of solid rocket firing tests. The main drawbacks of Evans' measurement technique and test apparatus were the limited scale of the tests that could be conducted due to the requirement for X-ray equipment, and the lack of nozzle temperature measurement paths. As a result, Evans' final correlation took the same form as that of Keswani et al.'s correlation in [32] and Jones et al. in [33], relating the time-averaged nozzle throat erosion rates with the mass fraction of oxidizing species and chamber pressure.

Most recently, Kamps et al. demonstrated a low-cost, highly-versatile method for conducting basic research on the mechanisms of graphite nozzle erosion through the operation of hybrid rocket test motors. The use of a hybrid rocket motor with the new measurement method means that a wide range of mixture ratios can be examined with fewer tests. Hybrid rockets are also much easier to design and manufacture due to ease of handling, low-toxicity and non-explosive nature of hybrid rocket fuels. Numerous data for

nozzle erosion rate can be obtained from a single firing test since the history of nozzle throat radius can be determined using Kamps et al.'s experimental method. Thus, the knowledge gaps in our current understanding of nozzle erosion and the associated contributions expected by this research can be summarized as follows:

Knowledge Gap 1: Empirical models from previous studies fail to adequately predict the onset of erosion, or discuss the specific conditions that should be avoided to prevent chemical erosion, for example through cooling.

Expected Contribution: Nozzle temperature histories will be determined in conjunction with erosion rate histories to quantify the activation temperature of graphite. Furthermore, tests will be conducted in which the time of shutdown is the independent variable, allowing for confirmation of the erosion onset conditions: surface features, pressure etc.

Knowledge Gap 2: There is a lack of data for erosion rate under the wide range of combustion gas compositions that are possible with hybrid rockets.

Expected Contribution: Through numerous static firing tests with hybrid rocket motors data is collected for erosion rate under a wide range of gas compositions, including combustion gas rich with molecular oxygen, or rich with unburned fuel.

CHAPTER 2. MODEL OF CHEMICAL EROSION

Nozzle erosion can be summarized qualitatively as a process that begins when the nozzle has reached a temperature high enough for chemical reactions to be "activated," and continues so long as the rate that new molecules are supplied to the nozzle surface matches the rate at which oxidizing species are being consumed. The concentration gradient for a given oxidizing species *i* is labeled as Y_i. The key mechanisms involved in this process are depicted in Figure 6. Nozzle erosion will not occur at significant rates when the nozzle temperature is sufficiently low, even if the concentration of oxidizing species at the nozzle surface is high. The same is true when the supply of oxidizing species to the surface is sufficiently low, and the nozzle temperature is high.

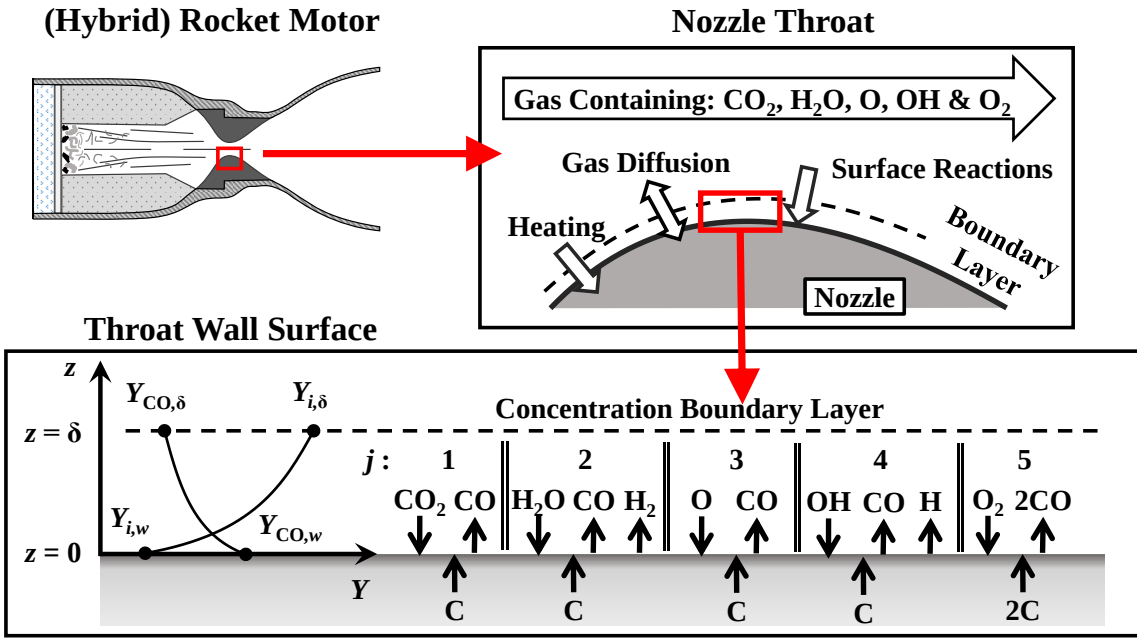

Figure 6. Oxidizing species gas diffusion at the nozzle throat during erosion.

2.1 Governing Equations of Chemical Kinetics and Mass Diffusion

Nozzle erosion is the result of heterogenous chemical reactions between the nozzle surface and the combustion gas passing over it, predominately CO_2, H_2O, O, OH and O_2. Thus, the erosion rate $\dot{r}$ at the nozzle surface can be calculated by Eq. (2-1):

$$\dot{r} = \sum \dot{r}_i \qquad i: \text{ oxidizing species} \tag{2-1}$$

Here $\dot{r}_i$ is the contribution to erosion rate from the *i*-th oxidizing species. The erosion contribution of each oxidizing species may be calculated according to an Arrhenius equation of the form in Eq. (2-2):

$$\rho_n \dot{r}_i = k_j p_i^{n_j} \qquad j: \text{ chemical reaction} \tag{2-2}$$

Here, k_j and n_j are the heterogenous rate constant and pressure exponent of the *j*-th chemical reaction, p_i is the partial pressure of species *i* at the nozzle wall, and ρ_n is the nozzle density. The rate constants are typically only a function of the nozzle wall temperature T_w, according to Eq. (2-3):

$$k_j\left(T_w\right) = A_j T_w^{b_j} \exp\left(\frac{-E_j}{R_u T_w}\right) \qquad A_j, b_j, E_j: \text{ empirical constants} \tag{2-3}$$

where R_u is the universal gas constant (R_u = 8.314 J/mol-K), and A_j, b_j and E_j are Arrhenius constants. The values for the Arrhenius constants that were reported by Bradley et al. in [41] and Chelliah in [42] are summarized in Table 2. For the reaction of O_2 with the nozzle, Eqs. (2-2) and (2-3) are not valid. The contribution of O_2 to nozzle throat erosion can be

determined by Eq. (2-4). When applying the constants in Table 2 to Eqs. (2-2) to (2-4), partial pressures should be input in units of atm, and the wall temperature in units of K.

$$\rho_n \dot{r}_{O_2} = \left(\frac{k_{5a} p_{O_2} Z}{1 + k_{5b} Z} \right) + k_{5c} p_{O_2} (1 - Z) \quad \text{where } Z = \left(1 + \frac{k_{5d}}{k_{5c} p_{O_2}} \right)^{-1} \tag{2-4}$$

Table 2. Heterogeneous rate constants and reaction order with graphite*.

Reaction**	j	ξ_j	A_j	E_j/R_u, K	b_j	n_j
$C_s + H_2O \rightarrow CO + H_2$	1	3.67	480,000	34,640	0.0	0.5
$C_s + CO_2 \rightarrow 2CO$	2	1.50	9,000	34,280	0.0	0.5
$C_s + O \rightarrow CO$	4	1.33	665.5	0.0	-0.5	1.0
$C_s + OH \rightarrow CO + H$	3	1.42	361	0.0	-0.5	1.0
$C_s + \frac{1}{2} O_2 \rightarrow CO$	5a	1.33	2,400	15,107	0.0	0.0
	5b		21.3	-2,065	0.0	0.0
	5c		0.0535	7655	0.0	0.0
	5d		18,100,000	48,845	0.0	0.0

*values taken from [41],[42].

**subscript "*s*" denotes the "solid" phase

To predict the nozzle erosion rates according to the Arrhenius equations described above, the partial pressure of oxidizing species at the wall must be known. The partial pressure of oxidizing species in the bulk combustion gas at the throat can be estimated through chemical equilibrium analysis, however, when nozzle erosion is taking place, the product gas CO is generated and a concentration gradient forms between the bulk fluid flow and the nozzle wall. Thus, some additional analysis is necessary to estimate the partial pressures of oxidizing species at the wall.

In the case when only the diffusion of a single oxidizing species "*i*" in the negative *z*-direction and CO in the positive *z*-direction are considered, as shown in Figure 6, the solution for surface (erosion) mass flux can be determined analytically through the integration of Fick's Law. The boundary conditions of integration are: @ $z = 0$, $Y_i = Y_{i,w}$; and @ $z = \delta$, $Y_i = Y_{i,\delta}$, as depicted in the lower left-hand side of Figure 6. The symbol *Y* is mass fraction, and the symbol δ is the boundary layer thickness in meters. Equation (2-5) is the solution to this integration. The derivation of similar problems can be found in [31](pp. 533-545) and in [43](pp. 551-553).

$$\rho_n \dot{r}_i = \frac{\left(\rho D_{CO,i}\right)_w}{\delta_i} \ln\left(\frac{1 + Y_{i,\delta}/\xi_j}{1 + Y_{i,w}/\xi_j}\right) \tag{2-5}$$

where density, ρ [kg/m^3], and diffusivity, D [m^2/s], were chosen to be the value of the gas mixture and binary diffusion coefficient of CO and "*i*" at the nozzle wall temperature, respectively. Similarly, the boundary condition was selected to be the concentration boundary thickness of species "*i*". The term ξ_j is the stoichiometric oxidizer-to-fuel-mass ratio of the "*j*-th" reaction – see Table 2. The binary diffusion coefficients can be predicted from the Chapman-Enskog theory. This procedure is detailed in [31](pp. 708-709). For the sake of the reader, the necessary equations and reference values will be introduced here. The governing equation for the binary diffusion constant of arbitrary gases "A" and "B" is Eq. (2-6):

$$D_{A,B} = \frac{0.0752 T^{3/2}}{P\Omega\left(\sigma_A + \sigma_B\right)^2} \sqrt{\frac{1}{MW_A} + \frac{1}{MW_B}} \tag{2-6}$$

where σ [Å], is hard-sphere collision diameter, *MW* [kg/kmol], is molecular weight, and Ω is the dimensionless collision integral calculated according to Eq. (2-7):

$$\Omega = \frac{1.06036}{\left(T^*\right)^{0.15610}} + \frac{0.19300}{\exp\left(0.47635T^*\right)} + \frac{1.03587}{\exp\left(1.52996T^*\right)} + \frac{1.76474}{\exp\left(3.89411T^*\right)} \qquad (2\text{-}7)$$

The term T^* is a dimensionless temperature defined by Eq. (2-8):

$$T^* = \frac{T}{\sqrt{\Lambda_A \Lambda_B}} \qquad (2\text{-}8)$$

where Λ [K], is the Lennard-Jones parameter. The values of σ and Λ for the gases pertinent to this research have been summarized in Table 3.

Table 3. Lennard-Jones parameters for diffusion coefficient calculation*.

Species	σ_i , Å	Λ_i , K	Species	σ_i , Å	Λ_i , K
Air	3.711	78.6	N_2	3.798	71.4
C_2H_4	4.163	224.7	N_2O	3.828	232.4
CO	3.690	91.7	O	3.050	106.7
CO_2	3.941	195.2	O_2	3.467	106.7
H_2O	2.641	809.1	OH	3.147	79.8

*values taken from [31].

The (concentration) boundary layer thickness of the "*i*-th" oxidizing species is estimated from the equation by Gilliland-Sherwood for diffusion of vapors into air streams in pipe flow [44], Eq (2-9):

$$\delta_i = \frac{d}{0.023\,\mathrm{Re}^{0.83}\,\mathrm{Sc}_i^{0.44}} \qquad (2\text{-}9)$$

where Re is the Reynold's number of the bulk fluid flow, calculated according to Eq. (2-10):

$$\mathrm{Re} = \frac{d\rho\sqrt{\gamma RT}}{\mu} \tag{2-10}$$

and Sc_i is the Schmidt number of the "*i*-th" oxidizing species, calculated according to Eq. (2-11):

$$\mathrm{Sc}_i = \frac{\mu}{\left(\rho D_{CO,i}\right)_w} \tag{2-11}$$

Other Sherwood number correlations are available, as listed in [45]. The improvement of the boundary layer thickness correlation is one possible outcome from this study.

2.2 Functional Dependencies of Erosion Rate

In recent years, Ozawa et al. estimated nozzle erosion rates of graphite nozzles in a computationally effective way by equating "*i*-th" erosion mass flux terms of Eqs. (2-2) and (2-5) [46]. The same procedure will be followed in this section, with the goal of identifying the key (mathematical) functional dependencies of pressure, temperature, oxidizing species concentration and scale on the overall erosion rate. Treating the reaction-diffusion balance of each species separately approximates the more complex diffusion process of the multi-component gas mixture, but it will allow for the development of an informed empirical model for experimental validation. The comparison of this simple analytical estimate of nozzle erosion rate and the experimental results of this research will be a valuable

contribution to the field. This research is the first to make a meaningful assessment of the accuracy and applicability of Ozawa et al.'s erosion rate prediction.

The values of pertinent gas properties in the combustion gas chamber can be estimated using NASA CEA and saved to a database:

$$\mu, \rho_c, T_c, R, X_i = CEA(\xi, P_c)$$

For computational purposes, the temperature, pressure and density decrease between the chamber and throat will be determined according to equations for isentropic expansion, (2-12) to (2-14):

$$P_t = \left(\frac{2}{\gamma + 1} \right)^{\frac{\gamma}{\gamma - 1}} P_c \tag{2-12}$$

$$T_t = \left(\frac{2}{\gamma + 1} \right) T_c \tag{2-13}$$

$$\rho_t = \left(\frac{\gamma + 1}{2} \right)^{\frac{1}{1 - \gamma}} \rho_c \tag{2-14}$$

Here the subscript "*t*" distinguishes the bulk fluid property at the "throat," from that of "*c*" in the chamber. The density of gas close to the nozzle wall is approximated by Eq. (2-15):

$$\rho_w \cong \left(\frac{T_t}{T_w} \right) \rho_t \tag{2-15}$$

Since T_t is greater than T_w, ρ_w will be greater than ρ_t. The properties of γ, μ, R, X_i (and Y_i) are assumed to be frozen during expansion from the chamber to the throat. The mass fraction of oxidizing species is related to the mole fraction through the relationship in Eq. (2-16):

$$Y_i = \frac{MW_i}{MW} X_i = \frac{R}{R_u} MW_i X_i \tag{2-16}$$

Now, a single implicit equation for the erosion rate can be deduced for each separate oxidizing species. The system of equations can be summarized as follows:

$$\rho_n k_j \left(\frac{MW_{mix}}{MW_i} P Y_{i,w} \right)^n = \frac{\left(\rho D_{\mathrm{CO},i}\right)_w}{\delta_i} \ln\left(\frac{1 + Y_{i,\delta}/\xi_j}{1 + Y_{i,w}/\xi_j} \right) \qquad \text{for } j\text{: 1 to 4}$$

$$\rho_n \left(\left(\frac{k_{5a} p_{\mathrm{O}_2} Z_w}{1 + k_{5b} Z_w} \right) + k_{5c} p_{\mathrm{O}_2} \left(1 - Z_w\right) \right) = \frac{\left(\rho D_{\mathrm{CO},\mathrm{O}_2}\right)_w}{\delta_{\mathrm{O}_2}} \ln\left(\frac{1 + Y_{\mathrm{O}_2,\delta}/\xi_5}{1 + Y_{\mathrm{O}_2,w}/\xi_5} \right) \qquad \text{for } j\text{: 5}$$

In each equation, the only unknown is the mass fraction of the oxidizing species at the wall, $Y_{i,w}$. Summing these equations results in the total erosion rate. The important thing to point out is that this system of equations can be solved for a given oxidizer/fuel propellant combination with just five inputs:

$$\dot{r} = f\left(d_t, P, \rho_n, T_w, \Phi\right)$$

Of these five inputs, the role of ρ_n is the least convoluted because it only appears once on the left-hand side of the equations [as in Eq. (2-2)], it's dependency is linear, and it is a constant in time. For these reasons, the four terms: d_t, P_c, T_w and Φ will be the focus of parametric analysis. The symbol Φ is equivalence ratio, and has been used instead of ξ. This representation of mixture ratio is more intuitive, because $\Phi < 1$ corresponds to the oxidizer-rich combustion, and $\Phi > 1$ corresponds to fuel-rich combustion. Of the four independent variables under analysis (d_t, P_c, T_w and Φ), Φ is the only variable which is expected to lead to a global maximum erosion rate. In the following sections the

dependencies of the other three variables will be investigated together with Φ as a two-dimensional parametric analysis. The results of this analysis are shown in Figure 7.

It is clear from Figure 7 that there are three distinct functional dependencies that emerge for d_t, P and T_w. The nozzle throat diameter exhibits a negative logarithmic functional dependency, the chamber pressure exhibits a power-law functional dependency, and the nozzle wall temperature exhibits a Sigmoid-type functional dependency. The results of curve fitting of plots in Figure 7 are summarized in Table 4. The functional dependency of erosion rate on Φ can be inferred from Table 4 because the same functional form of Φ appears in the results for all three parameters. This function is a modified form of the Gamma distribution:

$$\text{Gamma Distribution: } \beta(\Phi) = \frac{\beta_1 \Phi^{\beta_2 - 1}}{\Gamma(\beta_2)} \exp\left(-\frac{\Phi}{\beta_3}\right) \equiv \beta_1 \Phi^{\beta_2} \exp(\beta_3 \Phi)$$

In the gamma distribution, $\beta(\Phi)$, constants β_1, β_2, and β_3 can be adjusted such that a global maximum exists, and the function tends to zero towards the origin and towards infinity. The reason that this type of functional dependency emerged is clear from Figure 8, which plots the results of a detailed analysis of the Φ dependencies. The solid lines without markers represent the total erosion rate, whereas the lines with markers show the contribution to erosion rate from each oxidizing species. The dashed lines in the lower plots is the best fit of $\beta(\Phi)$ to the total erosion rates of the upper figures.

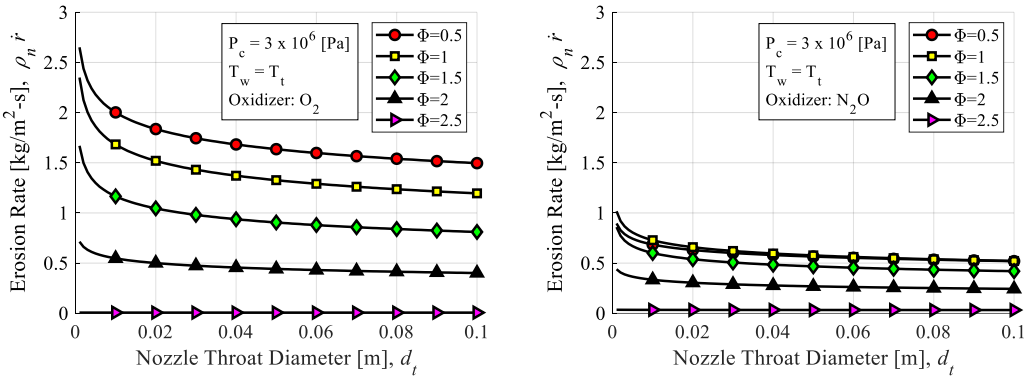

(a) Erosion rate decreases logarithmically with increasing nozzle throat diameter

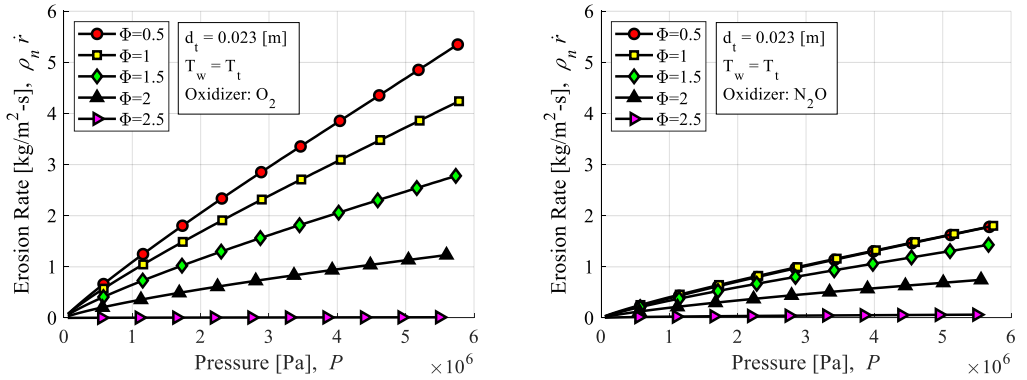

(b) Erosion rate increases nearly linearly with increasing chamber pressure

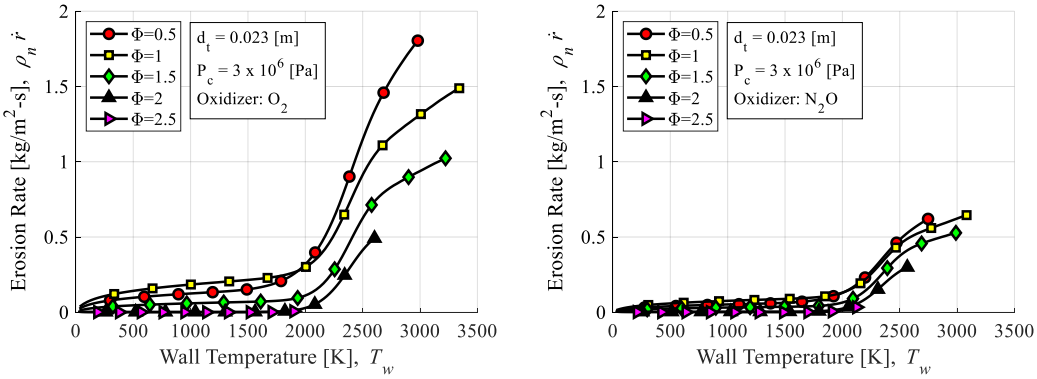

(c) Erosion is activated by a Sigmoid-type function near 2000 [K].

Figure 7. Erosion rate dependencies on: (a) d_t, (b) P_c, (c) T_w and Φ in the analytical model. *Left-hand figures for LOX/HDPE; right-hand figures for N2O/HDPE.*

Table 4. Functional dependencies of parametric analysis in Figure 7.

Parameter	Best Fit Functions for Figure 7	
	LOX/HDPE	N_2O/HDPE
d_t	$(14)\Phi^{2.6}\exp(-3.6\Phi)\left[1-\ln(d_t)\right]$	$(1.4)\Phi^{1.8}\exp(-2.2\Phi)\left[1-\ln(d_t)\right]$
P_c	$\left(2.4\times10^{-4}\right)\Phi^{2.7}\exp(-3.7\Phi)P^{0.9}$	$\left(2.1\times10^{-5}\right)\Phi^{1.8}\exp(-2.3\Phi)P^{0.9}$
T_w	$\dfrac{(0.052)\Phi^{0.6}\exp(-1.5\Phi)T_w^{0.6}}{1+\exp\left(-\dfrac{1}{180}(T_w-2320)\right)}$	$\dfrac{(0.017)\Phi^{0.7}\exp(-1.2\Phi)T_w^{0.6}}{1+\exp\left(-\dfrac{1}{170}(T_w-2280)\right)}$

The values of β_1, β_2, and β_3 from Figure 8 (c), agree well with those for the results of d_t in Table 4. Furthermore, the prediction of a maximum erosion rate in oxidizer rich conditions agrees with the findings from previous research [22][38].

Another conclusion that can be drawn from the plots in Figure 8 is that there is an obvious correlation between the magnitude of erosion rate and the mass fraction of oxidizing species. All of the subplots in Figure 7 and Figure 8 were made to have the same axis so that the difference in magnitude of erosion rate when using O_2 and N_2O would be obvious. The reason that erosion rate does not continue to increase with increasing concentrations of oxidizing species – in the region of $\Phi < 0.5$ – is because the temperature of combustion gas sharply decreases. Gas temperature is plotted in Figure 8 (a).

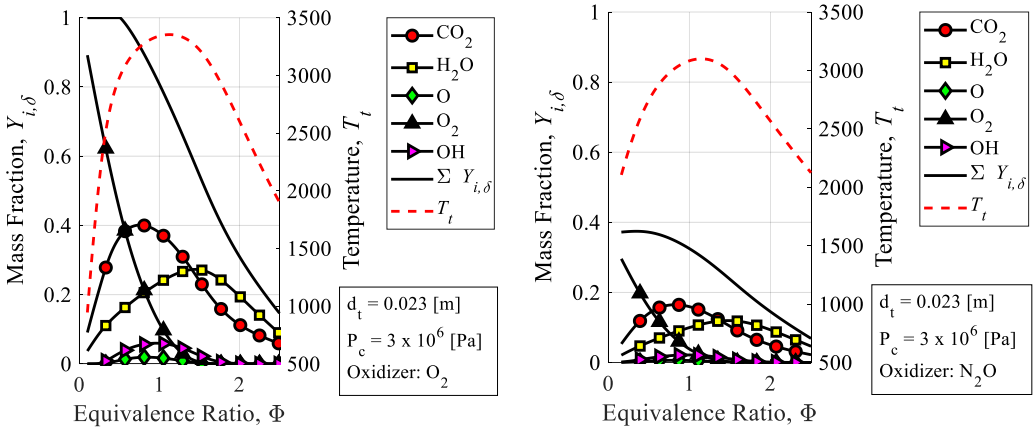

(a) The total mass fraction of oxidizing species increases with decreasing Φ

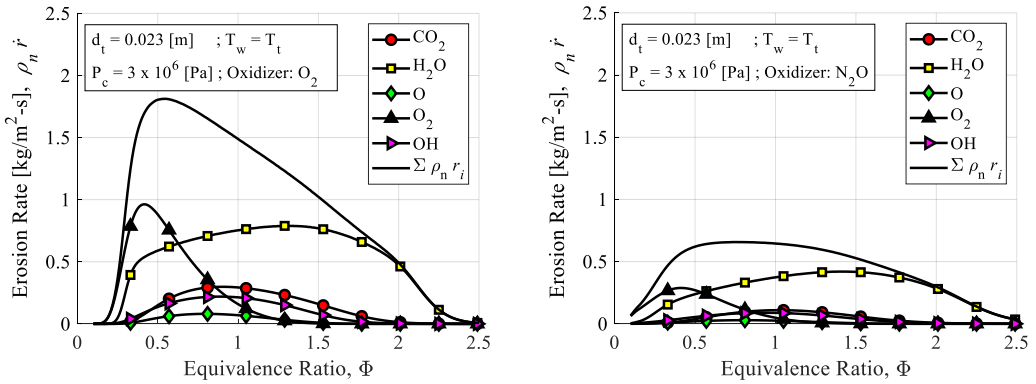

(b) Erosion rate dependency matches oxidizing mass fraction dependency in (a)

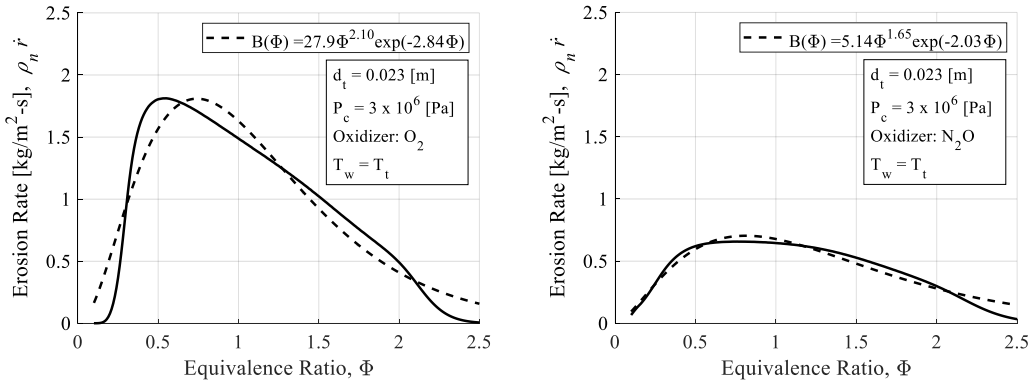

(c) Gamma distribution adequately mimics dependency of erosion rate on Φ

Figure 8. Strong dependency on concentration of oxidizing species and temperature. *Left-hand figures for LOX/HDPE; right-hand figures for N2O/HDPE.*

2.3 Novel Empirical Formulas

From an experimental point of view, it is not clear how to improve upon the analytical model of Section 2.2 without resorting to finding new formulations for the Arrhenius equations or mass diffusion constants from previous research. However, generalized formulas for empirical correlations can be developed based on the functional dependencies that were observed in the parametric analysis and through a qualitative understanding of the reaction-diffusion process that leads to nozzle erosion. Three models will be introduced in this section. The first is a purely mathematical interpretation of the results of Section 2.2. The second is a generalization of the circuit analogy in which the chemical and diffusion erosion rates are defined as separate conductors. The third is a modified Arrhenius equation that approximates the mass fraction of oxidizing species at the nozzle wall by a factor of mass diffusivity of oxidizing species in the bulk fluid flow. All formulas treat the combustion gas in the nozzle as a single oxidizing agent, and use a Gamma-distribution to replicate the effect of equivalence ratio on the bulk fluid behavior.

2.3.1 Formula Based on Functional Dependencies of Erosion Rate

The trend in functional dependencies of the analytical model can be summarized by the empirical formula, Eq. (2-17):

$$\rho_n \dot{r} = \frac{\beta(\Phi) T_w^b P^n \left[1 - \ln(d_t)\right]}{1 + \exp\left(-\left(T_w - E_1\right)/E_2\right)} \tag{2-17}$$

Where β_1, β_2, β_3, b, n, E_1 and E_2 can be determined experimentally for a give propellant combination. Based on the results as shown in Table 4, initial guesses for these constants

should be 10^{-4}, 3, 1/3, 0.6, 0.9, 2300 K and 180 K, respectively. One challenge that may emerge from this correlation, is that the units of β_1 depend on the values of *b* and *n*. This is mostly because the equation is not non-dimensional. This empirical correlation requires data for ρ_n, $\dot{r}$, Φ, *P*, T_w, and d_t, however, it is clear from the analysis of Section 2.3 that the correlation should focus on the parameters Φ, *P*, and T_w. Moreover, since the formula relies on Φ, separate correlations are needed for when different oxidizers are used.

The minimum number of data necessary for a statistically meaningful correlation can be surmised as follows. For β_1, β_2, β_3, at least 5 data are needed, for *b* and *n* an additional 3 each, and for E1 and E2 at least 5: 5 (for β's), x 3 (for *n*) x 3 (for *b*) x 5 (for *E*'s) = 225. Any set of data smaller than 225 will render at least one of the empirical constants meaningless. Increasing the statistical significance of the correlation requires even larger sets of data. For example, just increasing the number of data for each relationship by one point yields: 6 (for β's), x 4 (for *n*) x 4 (for *b*) x 6 (for *E*'s) = 576, more than twice the minimum value.

2.3.2 Formula Based on the Electrical Circuit Analog

In the analytical model of Section 2.2, equating terms from Eqs. (2-2) and (2-5) led to a system of implicit (transcendental) equations of $Y_{i,w}$. It is difficult to examine or interpret the transition between chemical kinetic-limited and diffusion-limited erosion regimes because of the implicit dependency on $Y_{i,w}$. Here the electrical circuit analog will be invoked to develop an alternative empirical formula to that of Eq. (2-17). The erosion rate is treated as the "current" running through a circuit consisting of two resistors, and the

voltage drop is the change in mass fraction of oxidizing species, ΔY, as shown in Figure 9.

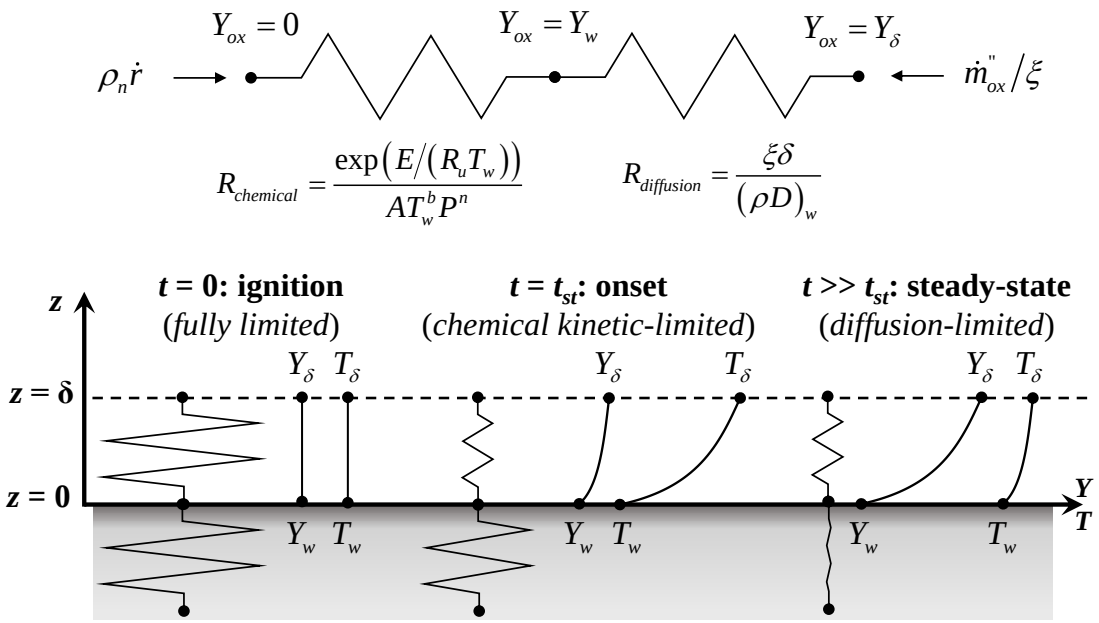

Figure 9. Depiction of chemical erosion "circuit" and phases of erosion.

The resistances, $R_{chemical}$ and $R_{diffusion}$, represent the inverse of the chemical kinetic-limited erosion rate and the diffusion-limited erosion rate, which can be thought of as "conductors". Therefore, the total erosion rate can be related to the chemical according to Eq. (2-18):

$$\rho_n \dot{r} \equiv I_{erosion} = \frac{\Delta Y}{R} = \frac{Y_\delta - 0}{R_{chemical} + R_{diffusion}} \tag{2-18}$$

This circuit analog concisely, and visually, explains the three main phases of erosion that can be expected to occur. Just after ignition, combustion is incomplete, and the nozzle

remains at room temperature, thus both resistances are quite high. Shortly after ignition, the combustion gas may be mixing and reacting efficiently, rich with oxidizing species diffusion at high temperatures, whereas the nozzle has not had enough time to heat up. In this case the diffusion resistance is much smaller than the chemical kinetic resistance, and erosion is said to be chemical kinetic-limited. Well into the firing duration, the nozzle may reach a steady-state temperature such that the chemical kinetic resistance is much smaller than the diffusion resistance. This is the diffusion-limited case.

In order to form an empirical model of this circuit analog function, we must identify what components of each erosion contribution serve as fitting parameters. The strategy taken here is to treat the bulk fluid flow at the nozzle throat as a single oxidizing agent that has a first-order dependency on mass fraction of the oxidizing species. In this way the chemical erosion rate, $\dot{r}_{chemical}$, takes on the form of Eq. (2-19).

$$\rho_n \dot{r}_{chemical} \cong A T_w^b \exp\left(-\frac{E}{R_u T_w}\right) P^n Y_w \tag{2-19}$$

where the empirical constants *A*, *b*, *E* and *n*, represent the behavior of the (bulk) oxidizing agent that is the combustion gas mixture at the throat. The mass fraction term, Y_w, is the sum of all oxidizing species at the nozzle wall. In Eq. (2-19), a first-order dependency was assumed for the mass fraction of oxidizing species, however, for the sake of empirical correlation, the pressure exponent was preserved. Now the chemical kinetic erosion resistance can be approximated by Eq. (2-20):

$$R_{chemical} = \frac{\Delta Y_{chemical}}{\rho_n \dot{r}_{chemical}} \cong \frac{Y_w - 0}{AT_w^b \exp\left(-\frac{E}{R_u T_w}\right) P^n Y_w} = \frac{\exp\left(E/\left(R_u T_w\right)\right)}{AT_w^b P^n} \qquad (2\text{-}20)$$

The diffusion erosion rate and its resistance will be formulated under the approximation that the mass fraction of oxidizing species at the wall, Y_w, is relatively small. In this way the diffusion erosion rate, $\dot{r}_{diffusion}$, takes on the form of Eq. (2-21):

$$\rho_n \dot{r}_{diffusion} = \frac{\left(\rho D\right)_w}{\delta} \ln\left(\frac{1 + Y_\delta/\xi}{1 + Y_w/\xi}\right) \cong \frac{\left(\rho D\right)_w}{\delta}\left(\frac{Y_\delta + Y_w}{\xi + Y_w}\right) \qquad (2\text{-}21)$$

The main approximation made in Eq. (2-21) is that of the logarithm term was assumed to be equal to the mass transfer term within the logarithm, as shown here:

$$\ln\left(\frac{1 + Y_\delta/\xi}{1 + Y_w/\xi}\right) = \ln\left(1 + \frac{Y_\delta - Y_w}{\xi + Y_w}\right) \cong \frac{Y_\delta - Y_w}{\xi + Y_w}$$

This approximation is generally valid, because the mass transfer term is much less than one. Now the diffusion resistance term can be approximated by Eq. (2-22):

$$R_{diffusion} = \frac{\Delta Y_{diffusion}}{\rho_n \dot{r}_{diffusion}} \cong \frac{Y_\delta + Y_w}{\frac{\left(\rho D\right)_w}{\delta}\left(\frac{Y_\delta + Y_w}{\xi + Y_w}\right)} = \frac{\xi + Y_w}{\left(\rho D\right)_w/\delta} \cong \frac{\xi\delta}{\left(\rho D\right)_w} \qquad (2\text{-}22)$$

The average stoichiometric oxidizer-to-fuel-mass ratio of oxidizing reactions is $\xi \approx 2$, so this approximation is relatively inaccurate when $Y_w > 0.2$, but the simplification that this

approximation provides is necessary for conducting empirical correlations. Substituting Eqs. (2-20) and (2-22) into Eq. (2-18), yields the empirical formula shown by Eq. (2-23):

$$\rho_n \dot{r} = \frac{Y_\delta / R_{diffusion}}{1 + \dfrac{R_{chemical}}{R_{diffusion}}} \cong \frac{\left((\rho D)_w / \xi\delta \right) Y_\delta}{1 + \dfrac{\exp\left(E/\left(R_u T_w\right)\right)}{A T_w^b P^n} \dfrac{(\rho D)_w}{\xi\delta}} \tag{2-23}$$

This formula has four empirical constants: *A*, *E*, *b* and *n*. One major benefit of Eq. (2-23) is that it can easily be nondimensionalized by dividing out the diffusion mass flux term, $(\rho D)_w / \delta$. The non-dimensional form of Eq. (2-23) is:

$$\frac{\rho_n \delta \dot{r}}{(\rho D)_w} = \frac{Y_\delta / \xi}{1 + \dfrac{\exp\left(E/\left(R_u T_w\right)\right)}{A T_w^b P^n} \dfrac{(\rho D)_w}{\xi\delta}}$$

The major downside to the correlation is that it is not clear if the numerous approximations made related to the oxidizing species mass fraction were appropriate or not. It is also doubtful that the Arrhenius constant *A* can be treated as a constant given that the concentration of oxidizing species is a function of Φ, which varies during a firing test. Thus, an experiment-friendly simplification of the circuit analog formula is that shown by Eq. (2-24):

$$\frac{\rho_n \delta \dot{r}}{(\rho D)_w} \cong \frac{Y_\delta / 2}{1 + \dfrac{\exp\left(E/T_w\right)}{\beta_1 \Phi^{\beta_2} \exp\left(\beta_3 \Phi\right) T_w^b P^n} \dfrac{(\rho D)_w}{\delta}} \tag{2-24}$$

Here, the Gamma distribution-type function was used to modify the Arrhenius equation constants to account for the effect of Φ on gas composition. Thus, there are six empirical constants: β_1, β_2, β_3, *b*, *n*, and *E* that can be determined experimentally. The functional dependency of the numerator is shown in Figure 10, which was determined using the method of Section 2.2. It is evident that erosion rate can be expected to depend nearly linearly on the mass fraction of oxidizing species at the edge of the concentration boundary layer. Based on these results, and the values for temperature dependency as shown in Table 4, initial guesses for β_1, β_2, β_3, *b*, *n*, and *E* will be 1, 2, 3, -0.5, 0.5 and 2000 K, respectively.

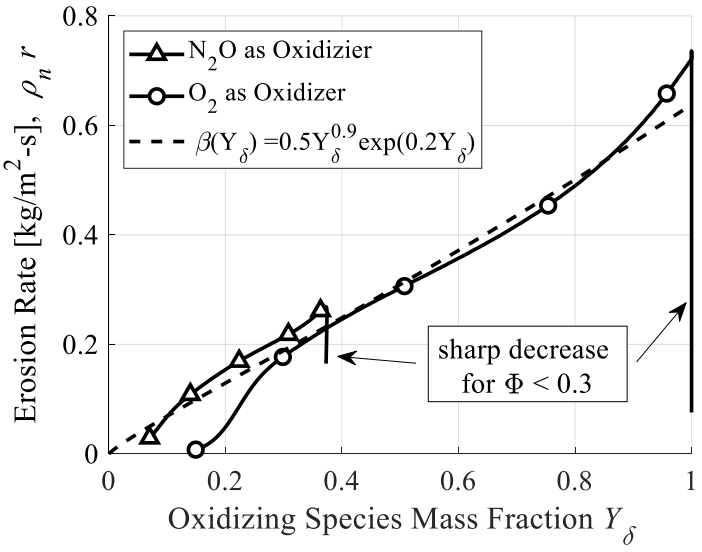

Figure 10. Dependency of erosion rate on mass fraction of oxidizing species.

2.3.3 Formula Based on Modified Chemical Kinetic Erosion Equation

The results of the parametric analysis in Section 2.2 (Table 4) show that diffusion-limited erosion is not expected to occur until $T_w > 2750$. This is because the exponent term in the denominator is larger than 0.1 for $T_w < 2750$. For temperatures larger than 2750 K, the diffusion mass flux should be the sole contributor to any further increases in temperature, for which the functional dependency is represented by the numerator of Eq. (2-17), as well as by the numerator of Eq. (2-24). Kamps et al. showed that a modified form of the chemical erosion (Arrhenius-type) equation satisfactorily replicates the complicated reaction-diffusion behavior during nozzle erosion [47]. This is done by scaling the chemical kinetic-limited erosion formula of Eq. (2-19) by the product of diffusion mass flux of the bulk fluid flow at the throat and the turbulent Sherwood number. This is, in essence, the product of Eqs. (2-19) and (2-21), in terms of equivalence ratio, as shown by Eq. (2-25):

$$\rho_n \dot{r} = \beta(\Phi) T_w^b \exp\left(-\frac{E}{R_u T_w}\right) P^n \left(D \,\mathrm{Re}^{0.8}\, \mathrm{Sc}^{0.4}\right) \tag{2-25}$$

To nondimensionalize Eq. (2-25), and remove the dependency on equivalence ratio, the additional term δ/ρ needs to be multiplied to the left-hand side. The resulting empirical formula is Eq. (2-26):

$$\frac{\rho_n \delta \dot{r}}{(\rho D)_t} = \beta(\Phi) T_w^b \exp\left(-\frac{E}{R_u T_w}\right) P^n \tag{2-26}$$

There are six empirical constants: β_1, β_2, β_3, b, E, and n, the Gamma distribution-function constant β_1 carries units $K^{-b}Pa^{-n}$. The initial guesses for these constants should be: 1, 1, 0, 0.6, 2300, and 0.6, respectively. The main benefit of this formula is that it is a single term. Any grouping of terms can be correlated directly, making it easy to work with in empirical correlations. The main drawback is that the diffusion-limited regime is not clearly distinguishable from the transition regime. The chemical-kinetic-limited regime is defined by the exponential dependency of temperature for very low temperatures, but one the temperature exceeds E/R_u, the transition between modes of erosion is blurred.

CHAPTER 3. COMPREHENSIVE DATA REDUCTION (CDR)

It was shown in Chapter 2 that it is necessary to collect hundreds of data points for $\dot{r}$, Φ, P, and T_w, for a statistically meaningful empirical correlation that can capture the complex turbulent mass diffusion and chemical-kinetic interactions of a multispecies (combustion) gas mixture and the nozzle wall. The only reasonable way to collect hundreds of data points is to measure the histories of these parameters, and ensure that some parameters change in time during a test. If a solid rocket motor were selected as the test apparatus, the value of Φ would remain constant during each test. This means that separate tests would be necessary for each data point. This is not true for a hybrid rocket motor, which has a shift in Φ during firing in response to nozzle erosion. Furthermore, it was shown in Chapter 1 that the chamber pressure and propellant mass flow rate drop much faster in response to nozzle erosion in a solid rocket motor than in a conventional hybrid rocket motor. This means that the maximum firing durations of a solid rocket test apparatus will be restricted by the pressure loss resulting from excessive nozzle erosion. The logistical and safety costs associated with solid rocket propellant manufacturing and handling is also a limiting factor. Not only is it cheaper to conduct experiments using a hybrid rocket, but it is also safer and easier to scale up or down in size.

The main drawback to using a hybrid rocket is that determining the history of fuel mass consumption of a firing test requires some additional effort. Even in the simplest solid fuel grain designs, hybrid rocket motors are prone to a shift in Φ as the burning surface area changes during firing. The non-linear relationship between Φ, burning surface area, and solid fuel regression complicates attempts to determine the composition of gas at the

nozzle entrance. In short, it is the same complicated burning mechanisms that gives hybrid rocket motors their advantages and disadvantages for their use as experimental apparatus for conducting nozzle erosion research.

Decades of research and development on solid and hybrid rockets have led to the emergence of numerous techniques for the direct measurement of solid propellant regression [48]. These methods include but are not limited to ultrasound, x-ray radiography, microwave radiography, plasma capacitance gauge (PCG), and (embedded) resistance-based measurements. Although these techniques have been proven to be useful in certain cases, they all share a critical drawback from the perspective of this research. The first is that none of these methods is suitable for motors with complex grain geometries, which were crucial to this study. Second, except for x-ray radiography, with some tinkering and a simple fuel grain geometry, no technique is capable of measuring both the fuel regression rate and nozzle throat regression rate simultaneously using a single apparatus. Lastly, the cost-effectiveness and accuracy of employing these techniques at larger scales is either unknown or beyond consideration with the resources available for this research. There is only one category of techniques that overcomes the limitations of the others in the context of this research.

Of the multitude of measurement techniques introduced in previous research, the latest versions of the data reduction methods referred to as ballistic reconstruction techniques offer the most effective means of pursuing this research in a cost-effective and expedient way. In general, ballistic reconstruction techniques only require some combination of the following commonly measured experimental values: (1) oxidizer mass

flow rate, $\dot{m}_{ox}$; (2) chamber pressure, P_c; (3) thrust, F; (4) overall fuel mass consumed, Δm_{fu}; and (5) final nozzle throat diameter, $d_{t,f}$. This means that the same measurement equipment can be used regardless of fuel design, configuration, or scale. This is done by using either the c^* equation [Eq. (1-1)], thrust equation [Eq. (1-3)], or both, in an iterative algorithm to determine instantaneous values of the oxidizer-to-fuel mass ratio, ξ (i.e. Φ); c^* efficiency, η^* – i.e. the ratio of c^*/c^*_{th}; thrust correction factor, λ; and, recently, nozzle throat area, A_t. The first ballistic reconstruction techniques were introduced by researchers Wernimont and Heister [49], and Nagata et al. [50], which used the c^* equation to determine fuel mass consumption under the assumption that η^* is constant and nozzle throat erosion does not occur. Carmicino and Sorge [51], and Nagata et al. [52], alleviated the need to treat η^* as a constant by measuring thrust and incorporating the thrust equation, but their techniques also require that nozzle throat erosion does not occur. The first technique to successfully determine the histories of nozzle throat erosion and oxidizer to fuel mass ratio with an acceptable level of uncertainty was reported by Kamps et al. [38]. Their method was titled, the "Nozzle Throat Reconstruction Technique" or "NTRT." Kamps et al., demonstrated in a follow-on study how to solve the heat equation iteratively to determine the wall temperature histories using two thermocouple measurements from within the nozzle [53]. This follow-on technique was titled the "Throat Temperature Reconstruction Technique" or "TTRT."

When operating in fuel-rich conditions, the NTRT has a range of multiple solutions. More specifically, at any given time, there may be up to three values of Φ that close the system of equations governing the NTRT. This issue existed in previous techniques as well. Nagata et al. [52]. and Saito et al. [54], made a linear approximation of c^* in the region of

multiple solutions to overcome this issue, and showed that the loss in accuracy was acceptable in the tests under examination. Kamps et al. report that when N_2O is used as the oxidizer, this region of multiple solutions is larger and more sensitive than when O_2 is used, and developed an alternative to the NTRT titled, the "NTRT Plus," and labeled, $NTRT^+$ [55]. The concept of the $NTRT^+$ is to determine the fuel mass consumption history, and therefore the Φ history some other way, while still using the $NTRT^+$ to determine the nozzle throat erosion history. The major drawback to the $NTRT^+$ is that, in order to avoid multiple solutions, an alternative fuel mass consumption measurement technique must be considered. Kamps et al. suggest a simple compromise in test procedure to avoid having to incorporate any additional measurement equipment. They show that, if tests are relatively repeatable, fuel mass consumption history could be inferred from end-point data – i.e. the change in fuel mass consumption before and after firing. This is done by conducting multiple tests which start at the same initial conditions but shut down at different times.

Kamps et al. refer to the combination of testing and analysis through the NTRT, or $NTRT^+$ and the TTRT as "Comprehensive Data Reduction" [55]. The information flow of comprehensive data reduction is depicted in Figure 11. The Tiers of the operation represent places where data enters or exits a program. The left-hand side represents the original NTRT, and the right-hand side the $NTRT^+$. The NTRT is a Tier I operation because it can be carried out if a test has been conducted. The $NTRT^+$ requires multiple tests to be completed, and a time trace of fuel mass consumption to be resolved in a prior operation, which is why it is listed as a Tier II operation. However, the governing equations to all operations are the same.

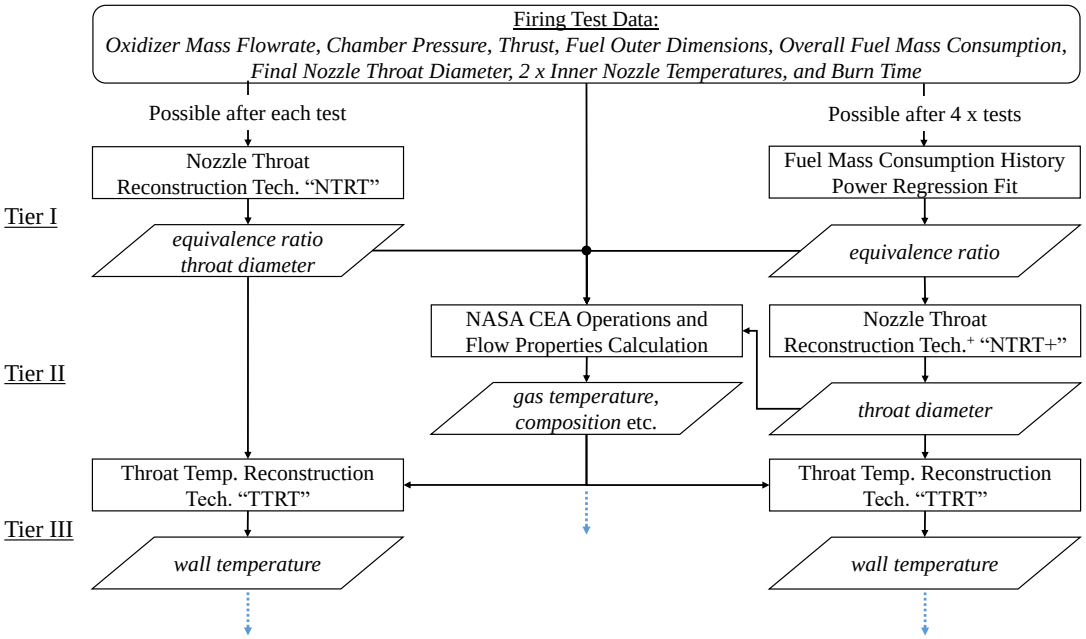

Figure 11. Flowchart of comprehensive data reduction operations.

3.1 The Nozzle Throat Reconstruction Techniques

In this research, only the NTRT and NTRT+ are used to evaluate the nozzle throat erosion rate. Since both techniques have the same governing equations, they will be introduced in tandem. The calculations of each technique can be summarized by the flowchart depicted in Figure 12. The key assumptions underlying the NTRT is that η^* and λ are constants in time, whereas in the NTRT$^+$ only λ is assumed to be constant. The algorithm underlying the NTRT and NTRT$^+$ is the minimization procedure of the residual term labeled as Ψ_{NTRT}. This residual term is defined by Eq. (3-1) for both techniques.

$$\Psi_{NTRT} = \begin{cases} \sqrt{\left(1-\dfrac{\sum \dot{m}_{fu}\Delta t}{\Delta m_{fu}}\right)^2 + \left(1-\dfrac{d_t(t_f)}{d_{t,f}}\right)^2} = f(\lambda,\eta^*) & \text{for the NTRT} \quad (3\text{-}1a) \\ \sqrt{\left(1-\dfrac{d_t(t_f)}{d_{t,f}}\right)^2} = f(\lambda) & \text{for the NTRT}^+ \quad (3\text{-}1b) \end{cases}$$

The summation term under the square root sign of the NTRT residual is the numerical integration of the calculated value of fuel mass flow rate, and the term Δm_{fu} is the measured value of fuel mass consumption. The term $d_t(t_f)$ is the calculated value for final nozzle throat diameter, and the term $d_{t,f}$ is the measured value. The NTRT residual is the discrepancy between calculated and measured results for overall fuel mass consumption and overall nozzle throat erosion, which is minimized through the iteration of efficiency terms, λ and η^*.

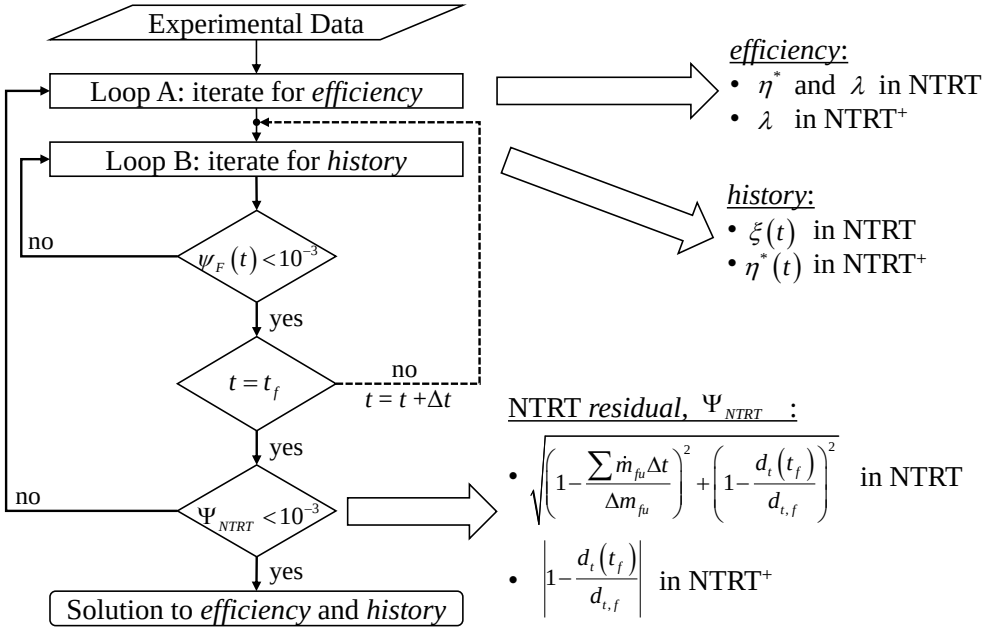

Figure 12. Flowchart of the NTRT and NTRT+ calculations.

The thrust residual term, ψ_F is essentially the same in both the NTRT and NTRT$^+$ except for which "history" is being solved for, according to Eq (3-2):

$$\psi_F(t) = \left| 1 - \frac{\lambda \dot{m}(t) u_e(t) + \left(P_e(t) - P_a\right) A_e}{F(t)} \right| = \begin{cases} f\left(\xi(t)\right) & \text{for the NTRT} \quad (3\text{-}2a) \\ f\left(\eta^*(t)\right) & \text{for the NTRT}^+ \quad (3\text{-}2b) \end{cases}$$

The NTRT solves for $\xi(t)$ while the NTRT$^+$ solves for $\eta^*(t)$ using the thrust equation. The term $F(t)$ in the denominator of Eq. (3-2) is the measured history of thrust, while the numerator is the calculated value resulting from the NTRT or NTRT$^+$ operation. Please refer to CHAPTER 1, Eqs. (1-1) to (1-5) for how to calculate specific terms within Eq. (3-2).

3.2 The Throat Temperature Reconstruction Technique

The TTRT procedure is less complicated than the NTRT or NTRT$^+$ procedure, and similar temperature calculations have been done in previous research on rocket nozzles. Mehta reported results from a technique where the heat flux at the nozzle wall is iterated for until the temperature profile history is solved for at every time step [56]. Mehta's procedure only requires one thermocouple calculation at the boundary, making it susceptible to computational instabilities. Narsai et al. also performed a similar calculation to Mehta, and took additional thermocouple measurements to check the accuracy of the calculated profiles [57]. It is also clear from Narsai et al.'s results that the indirect calculation of nozzle temperature profiles through the iteration of wall heat flux is prone to instabilities. This means that the position and response time of thermocouples must be accurately matched to the computational stability criteria. The method referred to as TTRT

by Kamps et al. alleviates these sensitivities through the input of additional thermocouple data. Instead of iterating for wall heat mass flux, Kamps et al. iterate wall temperature. The iteration criterion is the agreement in temperature of a secondary thermocouple placed between an outer thermocouple and the wall. At every time step, *j*, the nozzle temperature profile, T_n [K], is solved for according to Eq. (3-3):

$$\begin{bmatrix} T_{w+\Delta r}^{j+1} \\ T_{w+2\Delta r}^{j+1} \\ \vdots \\ T_{r_{n,2}-2\Delta r}^{j+1} \\ T_{r_{n,2}-\Delta r}^{j+1} \end{bmatrix} = \begin{bmatrix} b_{w+\Delta r}^{j} & c_{w+\Delta r}^{j} & 0 & 0 & 0 \\ a_{w+2\Delta r}^{j} & b_{w+2\Delta r}^{j} & c_{w+2\Delta r}^{j} & 0 & 0 \\ 0 & \ddots & \ddots & \ddots & 0 \\ 0 & 0 & a_{r_{n,2}-2\Delta r}^{j} & b_{r_{n,2}-2\Delta r}^{j} & c_{r_{n,2}-2\Delta r}^{j} \\ 0 & 0 & 0 & a_{r_{n,2}-\Delta r}^{j} & b_{r_{n,2}-\Delta r}^{j} \end{bmatrix}^{-1} \left(- \begin{bmatrix} d_{w+\Delta r}^{j} T_{w+\Delta r}^{j} \\ d_{w+2\Delta r}^{j} T_{w+2\Delta r}^{j} \\ \vdots \\ d_{r_{n,2}-2\Delta r}^{j} T_{r_{n,2}-2\Delta r}^{j} \\ d_{r_{n,2}-\Delta r}^{j} T_{r_{n,2}-\Delta r}^{j} \end{bmatrix} - \begin{bmatrix} a_{w+\Delta r}^{j} T_{w}^{j} \\ 0 \\ \vdots \\ 0 \\ c_{r_{n,2}-\Delta r}^{j} T_{n,2}^{j} \end{bmatrix} \right) \quad (3\text{-}3)$$

T_w at $j+1$ — Stiffness Matrix — T_w at j — Boundary

$$\begin{aligned} a_i^j &= 2\alpha^j r_i \Delta t - \alpha \Delta r \Delta t \\ b_i^j &= -\left(4\alpha^j r_i \Delta t + 2 r_i \Delta r^2\right) \\ c_i^j &= \alpha^j \Delta r \Delta t + 2\alpha^j r_i \Delta t \\ d_i^j &= 2 r_i \Delta r^2 \end{aligned}$$

where Δt is a time step, Δr is the radial mesh spacing, subscript *i* is the radial node index, and superscript *j* is the time index. A depiction of the radial mesh is shown in Figure 13, and the computation algorithm is depicted in Figure 14. In Eq. (3-3), the temperature profile vector at time "*j*+1" is the value that is being solved for, and the temperature profile vector at time "*j*" is the solution from the previous time step. The iteration for $T_w(t)$ ends when the inner thermocouple temperature residual, i.e. TTRT residual, $\Psi_{TTRT}(t)$ is close to zero, according to Eq. (3-4):

$$\Psi_{TTRT}(t) = \sqrt{\left(1 - \frac{T_n(r_1, t)}{T_{n,1}(t)}\right)^2} \quad (3\text{-}4)$$

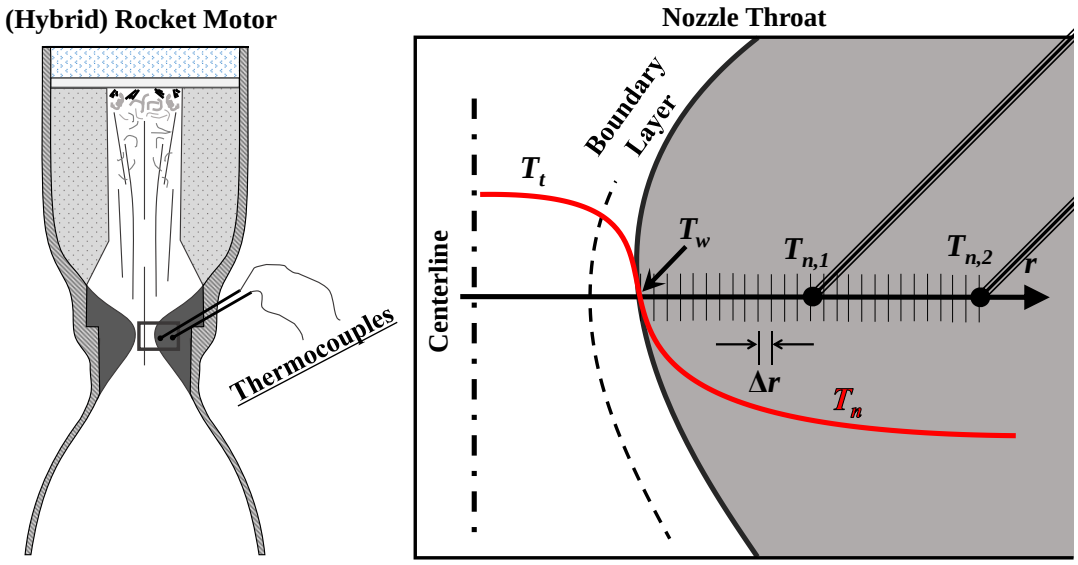

Figure 13. Radial mesh and thermocouple positions for TTRT calculations.

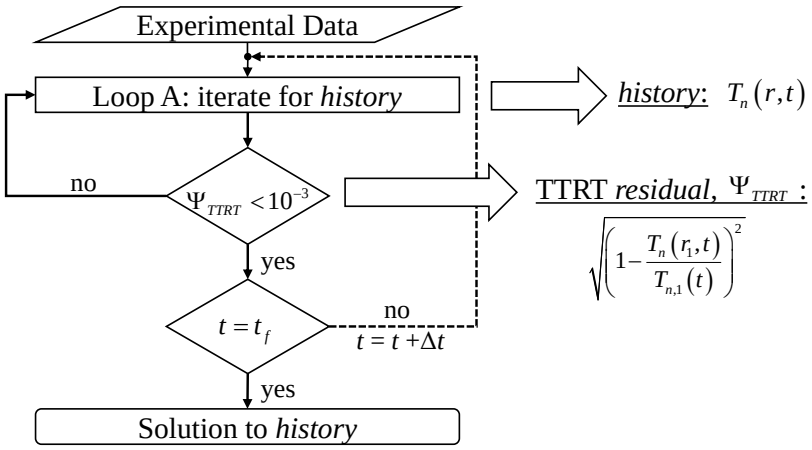

Figure 14. Flowchart of the TTRT calculations.

TTRT calculations are possible because we can assume at the beginning of combustion that entire nozzle temperature is the value of the thermocouple at position "2" (i.e. $T_{n,2}$). After this initial calculation has been completed, the solution can serve as the initial condition for the next time step.

CHAPTER 4. HYBRID ROCKET MOTOR OPERATION

Hybrid rocket static firing tests for this research were conducted continuously over the span of nearly three and a half years, from the fall of 2015 to the winter of 2018, at two separate facilities, one at Hokkaido University and one at Uematsu Electric Company, with teams of student members. Consequently, the test apparatus and operation procedures improved in time. The two test facilities today are far better organized and equipped to monitor and record more test data than before. Explaining these incremental improvements would be an unwarranted distraction from the main topic of study. The main objective of this chapter is to describe how the core set of measurements for employing the Comprehensive Data Reduction methods of CHAPTER 3 were obtained, and how experimental uncertainties in these measurements were quantified and/or overcome.

4.1 Experimental Apparatus

The test setup at Hokkaido University was designed to accommodate hybrid rocket motors that produce 500 N of thrust or less, although most of the tests conducted for this research had thrusts of 100 N or lower. The test setup at Uematsu Electric Company was designed to handle hybrid rocket motors that produce 30,000 N (i.e. 30 kN) of thrust or less, although most of the tests conducted for this research had thrust of 2 kN or lower. A generalized depiction of these test setups is shown in Figure 15, and screen captures of static firing tests are shown in Figure 16. Although the sizes of the test stands are not the same, both stands mount the hybrid rocket motor to a sled that is suspended on rails so that thrust can be measured using a load cell, and oxidizer mass flowrate can be measured using an orifice plate. Both test facilities have the equipment for supplying either liquid or

gaseous oxidizer to the motor. When a liquid is used as the oxidizer, it is stored in the "liquid reservoir," which is pressurized by an inert gas – usually He, but sometimes Ar. The pressurizing gas forces the liquid through a baffle and into the main feed line. When gaseous oxidizer is used, the flow is choked at the orifice to improve the accuracy of the flow rate measurement and prevent pressure instabilities. Ignition is achieved by heating the fuel with a coil of nichrome wire prior to supplying oxidizer to the motor. Shut down is achieved by cutting off the supply of oxidizer and purging the system with an inert gas, such as nitrogen (N_2). If the motor and test stand are not purged with an inert gas, the fuel of the hybrid rocket motor will continue to smolder, combusting with ambient air and/or oxidizer left in the feed system.

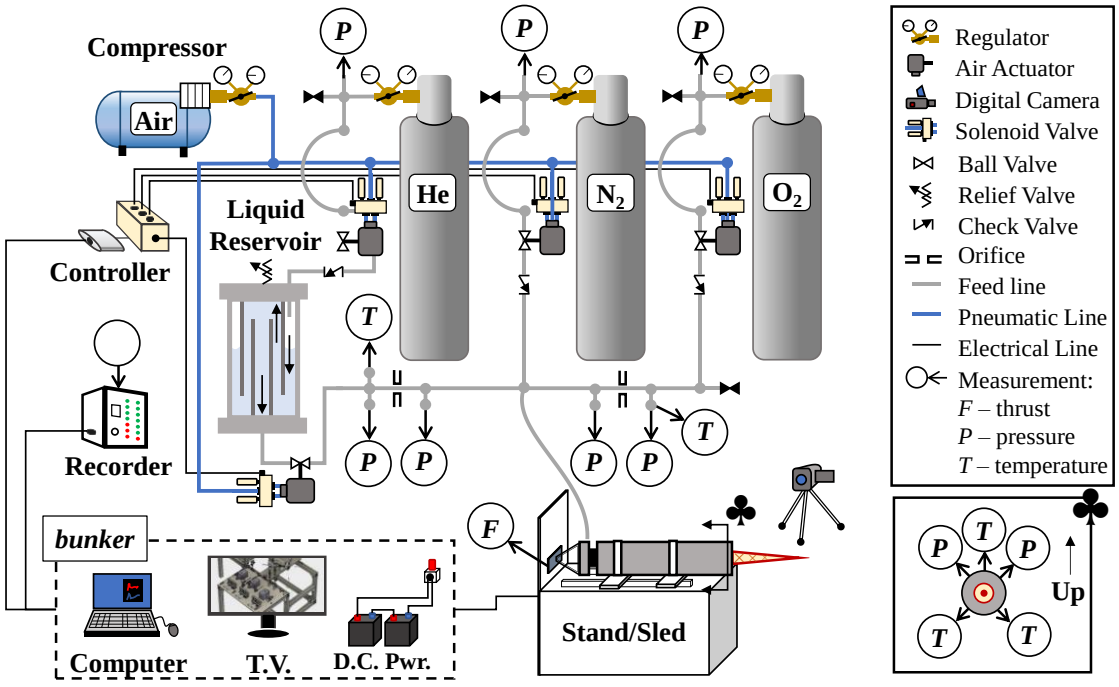

Figure 15. Generalized depiction of the test setup(s) used in this study.

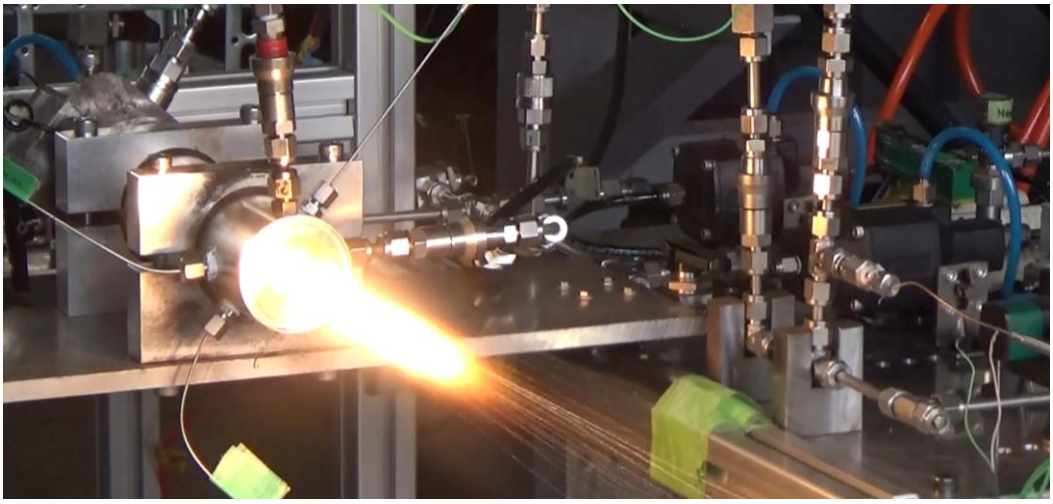

(a) Static firing test at Hokkaido University (see QE-5, CHAPTER 5)

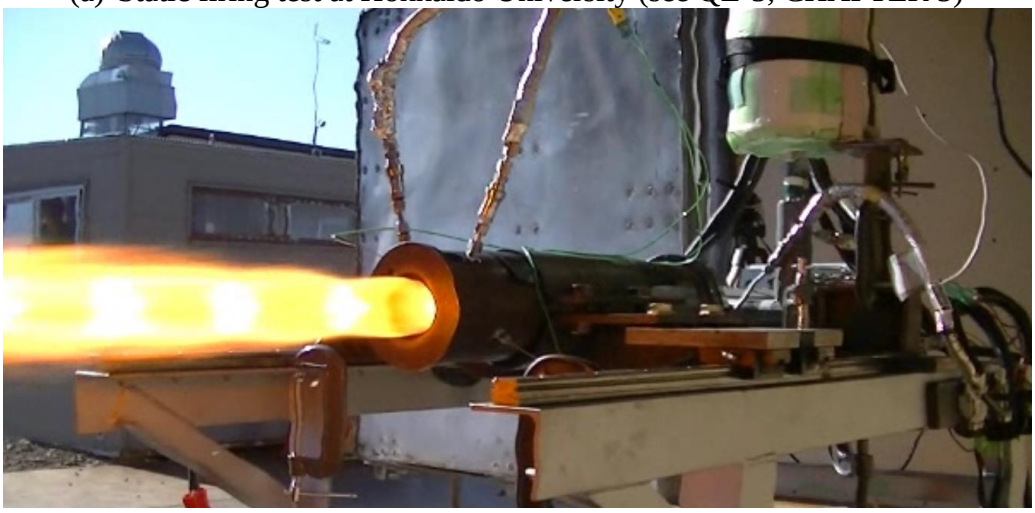

(b) Static firing test at Uematsu Electric Company (see ERM-2, CHAPTER 5)

Figure 16. Screen captures of hybrid rocket static firing tests.

All tests were conducted using high-density polyethylene (HDPE | formula: C_2H_4 | density 955 kg/m^3) as the fuel. Tests conducted at Uematsu Electric Company used a Cascaded Multistage Impinging-jet (CAMUI) type fuel grain, where most tests conducted at Hokkaido University used a conventional tubular fuel grain. The same general hybrid rocket motor design was used for all tests conducted at Hokkaido University, whereas two different designs were for tests conducted at Uematsu Electric Company. These three

hybrid rocket motors are depicted in Figure 17, Figure 18, and Figure 19, respectively. The easiest way to distinguish these designs is by geometric scale. The Hokkaido University motor, although adjustable to some degree, was 60 mm in diameter and 300 mm long when assembled. The first of two designs at Uematsu Electric Company, referred to by its experiment series name, the "ERM" design is roughly twice the size of the Hokkaido University motor. When assembled the outer diameter and length were 150 mm and 600 mm, respectively. The second of two designs at Uematsu Electric Co., the "MSS" design is approximately the same length as the ERM motor, but it has twice the outer diameter, at over 300 mm when assembled. Note that the thrust class of the ERM and MSS motors is the same, 2000 N or 2 kN, thus the nozzle throat diameters are roughly the same as well.

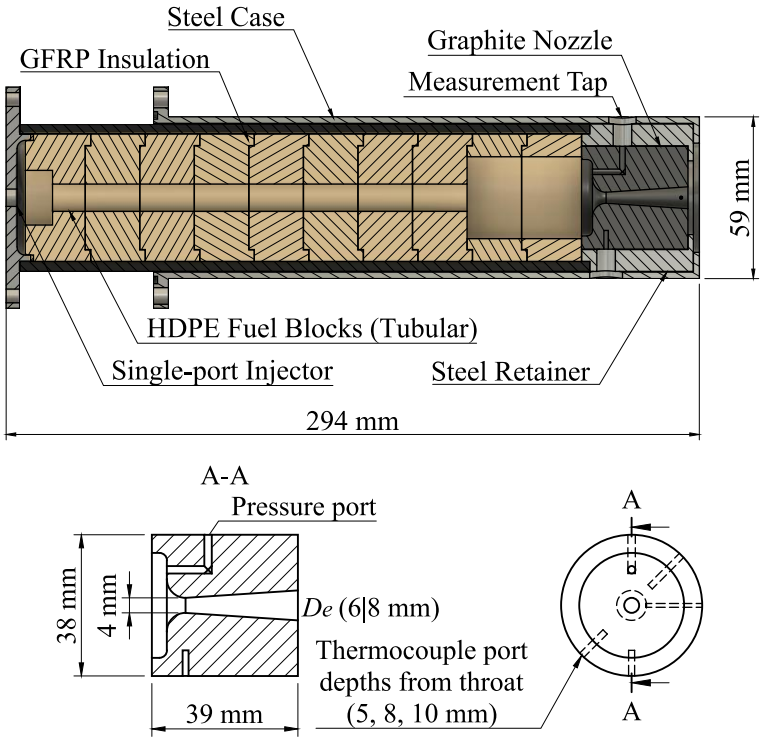

Figure 17. Hybrid rocket motor for the Hokkaido University test stand.

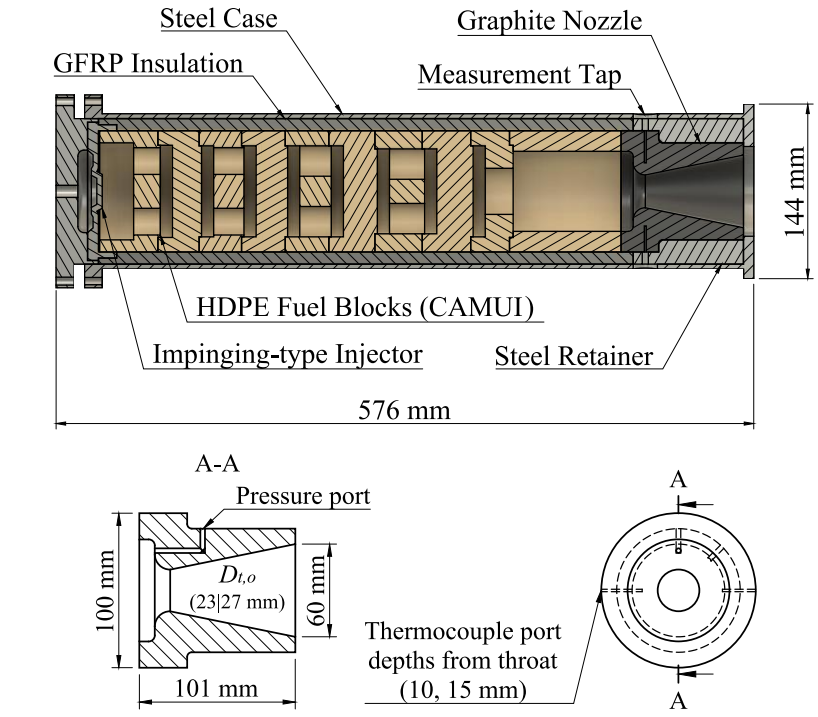

Figure 18. ERM series motor for the Uematsu Electric Company test stand.

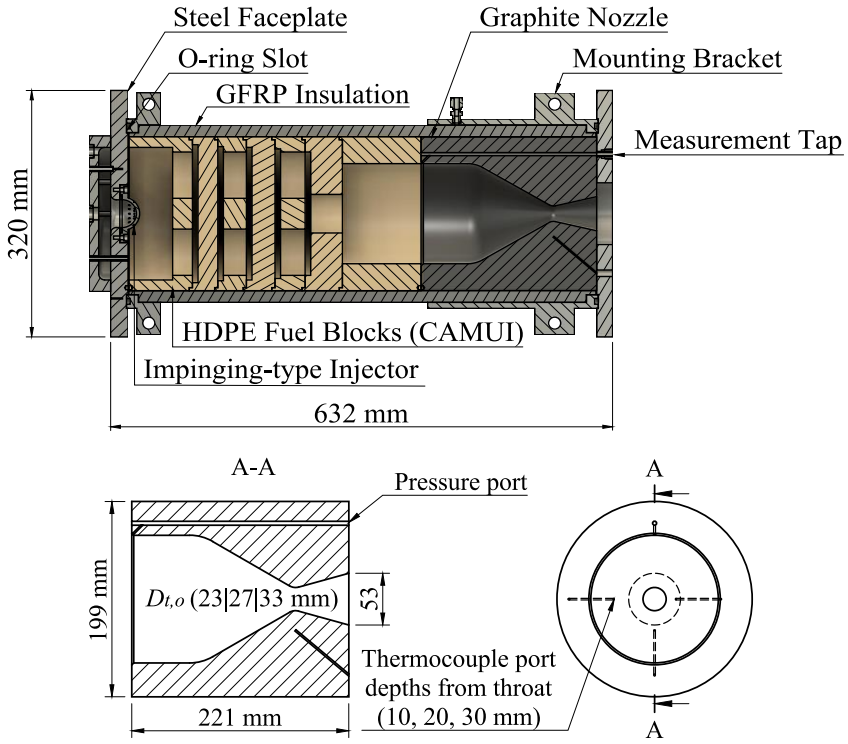

Figure 19. MSS series motor for the Uematsu Electric Company test stand.

Fuel grains in all tests were assembled from multiple short cylindrical blocks of fuel, which allowed for the correlation of fuel burning rates based on local mass flux and mixture ratio to assist in the test design process. After assembly, fuel grains were loaded into glass fiber-reinforced plastic (GFRP) insulating tubes and sealed in a steel motor case. The nozzles used in all tests were manufactured using the same grade of isotropic graphite, Tokyo Tokai Carbon Ltd. G347. The density and thermal conductivity at atmospheric conditions are listed by the manufacturer to be ρ_n = 1850 kg/m^3 and k = 116 W/m-K, respectively [58]. The temperature dependency of these and other properties of G347 graphite are not specified by the manufacturer, so values were referenced from previous research on similar high-density graphite. An empirical correlation of data for thermal conductivity based on Fig. 1 in [59] yields:

$$k_n\left(T_n\right) = 3712 T_n^{-0.602} \text{ W/m-K for } 200 \text{ K} < T_n < 2500 \text{ K}$$

An empirical correlation of data for specific heat based on Fig. 1 in [60] yields:

$$c_{p,n}\left(T_n\right) = 651 \ln\left(T_n\right) - 2877 \text{ J/kg-K for } 200 \text{ K} < T_n < 3000 \text{ K}$$

4.2 Data Acquisition and Processing

As required for the NTRT and TTRT, multiple dynamic and static measurements were taken during the experiments conducted in this study. Pressures were measured using KYOWA DCS-10 MPa and KYOWA DCS-5 MPa pressure sensors with rated accuracies of ±0.040 MPa and ±0.028 MPa, respectively. In tests at Hokkaido University thrust was

measured using a KYOWA LMB-A-200N load cell with a rated accuracy of ±3.5 N, and in tests at Uematsu Electric Company thrust was measured using a KYOWA LCTB-A-30kN load cell with a rated accuracy of ±16 N. These instruments were calibrated by the manufacturer such that the rated accuracies account for uncertainty due to nonlinearity, hysteresis, low-temperature conditions, and external loading. Nozzle temperatures were measured using RC Pro k-type thermocouples rated up to a maximum temperature of 1100 °C with a response time of 0.3 s. Due to the low level of thrust – generally less than 100 N – produced by the Hokkaido University motors, a preload of around 50 N was applied to the injector plate using two short bungee cords (visible in Figure 16 (a)). Dynamic measurements were recorded at either 200 Hz or 1000 Hz using DCS-100A series software, and later filtered using a 20-point moving average. The reason for applying a moving average was to reduce the presence of oscillations in reconstructed nozzle throat erosion histories, which ultimately lead to undiscernible linear approximations for nozzle throat erosion rate. The uncertainty introduced by applying such moving averages is considerably smaller than the precision limits of the sensors used.

When liquid oxidizer was used, $\dot{m}_{ox}$ was calculated by the pressure drop across the orifice, ΔP [Pa], according to Eq. (4-1):

$$\dot{m}_{ox} = c_d A_{or} \sqrt{2\rho\Delta P} \tag{4-1}$$

Where c_d is a dimensionless orifice discharge coefficient determined experimentally, A_{or} is the orifice cross-sectional area in m^2, and ρ is the oxidizer density upstream of the orifice. These calculations were done in a computer program so that density could be ascertained

through measurements of pressure and temperature upstream of the orifice. Formulas for the temperature dependencies of liquid N_2O and liquid O_2 density were created based on values from the National Institute of Standards and Technology (NIST) Chemistry Webbook (liquid). The formula for liquid N_2O density, ρ_{N2O} [kg/m^3], is:

$$\rho_{N_2O}(T) = aT^6 + bT^5 + cT^4 + dT^3 + eT^2 + fT + g$$

$$\begin{aligned} a &= -6.533\times10^{-7} & e &= 0.042801 \\ b &= 3.9166\times10^{-5} & f &= -5.11433 \\ c &= -6.266\times10^{-4} & g &= 906.6779 \\ d &= -0.002521 \end{aligned}$$

And the formula for liquid O_2 density, ρ_{O2} [kg/m^3] is:

$$\rho_{O_2}(T) = 1630.7 - 5.445T$$

When gaseous oxidizer was used, the flow was choked so that $\dot{m}_{ox}$ could be calculated using Eq. (4-2):

$$\dot{m}_{ox} = c_d A_{or} P \sqrt{\left(\frac{\gamma}{RT}\right)\left(\frac{2}{\gamma+1}\right)^{\frac{\gamma+1}{\gamma-1}}} \qquad (4\text{-}2)$$

where P and T are the pressure and temperature upstream of the orifice, R is the gas constant in J/kg-K, and γ is the specific heat ratio. For gaseous oxygen stored at room temperature the terms under the square root are: T = 293 K, R = 259.8 J/kg-K, and γ = 1.395; and Eq. (4-2) reduces to:

$$\dot{m}_{ox} = 0.00248 c_d A_{or} P \quad \text{for gaseous oxygen at 293 K}$$

Initial and final throat diameter of Hokkaido University nozzles were determined using the image analysis software ImageJ [61]. An example of this process is shown in Figure 20. A photograph of the nozzle is taken from 2 meters away using 42x optical zoom. This photograph is loaded through the software ImageJ, and a length scale is set using a reference grid places next to the nozzle. The area of "particles" at the throat can be measured by making the photograph "binary" and "inverting" the black and white pixels. The nozzle throat diameter/radius is backed out of the throat area according to Eq. (4-3):

$$d_t \cong \sqrt{\frac{4}{\pi} A_d} \tag{4-3}$$

(left) setting the scale using grid paper; (right) measuring area of particles at throat

Figure 20. Throat area measurement using ImageJ (test DNT-2, CHAPTER 5).

Initial and final throat diameters of the ERM and MSS nozzles were measured by hand using a Mitutoyo NTD14-20PMX digital caliper. These measurements were repeated

a minimum of 12 times, at angles of 0, 45, 90 and 135 degrees with respect to the chamber pressure measurement port. This measurement procedure is depicted in Figure 21.

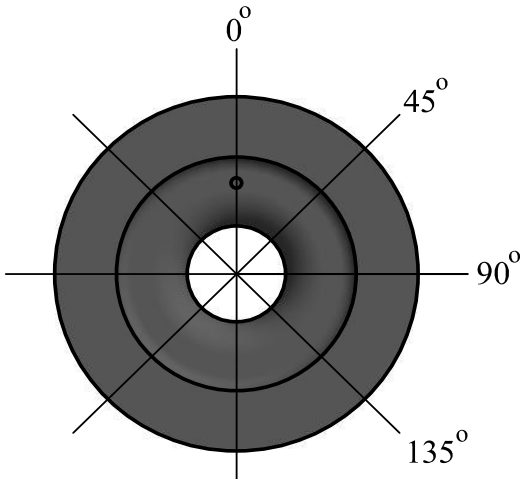

Trial	0°	45°	90°	135°
1	28.46	28.46	28.47	28.37
2	28.46	28.45	28.47	28.38
3	28.47	28.47	28.48	28.37

measurements in mm

Figure 21. Throat diameter measurement using a digital caliper (test ERM-4, CHAPTER 5).

Uncertainty in the experimental measurements of thrust, pressure etc. propagate through the NTRT, the intermediary property calculations and ultimately to the results of the TTRT. The details of this process can be summarized by Eq. (4-4), which expresses the overall uncertainty U_y in some NTRT/TTRT output y as a function of the inputs x_i:

$$U_y = \sqrt{\sum \left(\frac{\partial y}{\partial x_i} U_{x_i} \right)^2} \tag{4-4}$$

where the U_{x_i} terms on the right-hand side represent the uncertainty in the x_i measurement. The partial derivative terms in Eq. (4-4) represent the sensitivity of the reconstructed

solution to each input. Since the algorithm in the NTRT/TTRT is a coupled non-linear problem, the partial derivative terms are approximated by Eq. (4-5):

$$\frac{\partial y}{\partial x_i} \cong \frac{y\left(101\%x_i\right) - y\left(100\%x_i\right)}{1\%x_i} \tag{4-5}$$

Here, the numerator is the change in NTRT/TTRT solution y given that the input parameter x_i has been perturbed by the amount of 1% of the nominal value.

CHAPTER 5. STATIC FIRING TEST RESULTS

A total of 60 successful hybrid rocket static firing tests were conducted for this research over the course of three and a half years from 2015 to 2019. A description of the test series, the timeframe during which the series were active, and a brief description of the series objectives and strategies are summarized in Table 6. The results of direct measurements necessary for carrying out comprehensive data reduction have been summarized in Table 7, and key results of comprehensive data reduction have been summarized in Table 8. These tables were placed together in APPENDIX A for convenience. Although calculations were maintained in the standard S.I. base units, the units in the tables and figures have been selected for the ease of tabulation. Nozzle throat radius, r_t, diameters, $d_{t,o}$ and $d_{t,f}$, average erosion rate, $\bar{\dot{r}}_t$, and mass diffusivity D_w at the wall are listed in units of (length of) millimeters. Boundary layer thickness, δ is listed in units of (length of) micrometers. Overall fuel mass consumption, Δm_{fu} , and average oxidizer mass flowrate, $\bar{\dot{m}}_{ox}$, are listed in units (of mass) of grams per second. Average chamber pressure, $\bar{P}_c$, average throat pressure, $\bar{P}_t$, and throat pressure histories, P_t, have been listed in MPa. Static firing tests can be separated into three groups: tests using gaseous oxygen (GOX) as the oxidizer, tests using liquid nitrous oxide (N_2O) as the oxidizer, and tests using liquid oxygen (LOX) as the oxidizer. These groups are sub-titled within the tables. An examination of the approximations of the comprehensive data reduction method is carried out in APPENDIX B, which shows that these assumptions result in an acceptably low amount of experimental uncertainty.

5.1 Overview of the Test Campaign and CDR Results

The test campaign was conducted in multiple series, which are listed in chronological order in Table 6 to highlight the evolution in the approach taken to investigate the mechanisms of erosion. The event that triggered this research is listed in the beginning of the table as excessive nozzle erosion in the 15kN-thrust class of the CAMUI hybrid rocket, which had been under development in collaboration between Hokkaido University and Uematsu Electric Company since the early 2000s. Static firing tests of the 15kN-thrust class CAMUI rocket were conducted between the summers of 2014 and 2015 at Uematsu Electric company, at which time there were no publications in open literature that reported on the erosion of graphite in hybrid rockets, nor was there an affordable way to measure both the equivalence ratio and nozzle throat erosion histories of a firing test. Based on previous research, it was clear that the equivalence ratio would dictate the severity of erosion in the sense that lower equivalence ratios would result in increased mass fractions of oxidizing species, however a quantitative assessment was not available for reference.

5.1.1 Breakdown of Results by Test Series

The ERM series was initiated in the Spring of 2015 to collect data on the erosion rate of graphite over a wide range of equivalence ratios. The ERM motor design was essentially a scaled-down version of the 15kN-thrust class flight motor. ERM-1 suffered from a burn through of the motor casing, and the thrust measurement of ERM-7 was compromised by a bad grounding wire. ERM-2 thru -6 and ERM-8 thru -10 were successful, however the excessive erosion of ERM-9 is due in part to mechanical failure.

This can be seen in the photographs of the ERM-9 nozzle post firing in APPENDIX C. The results of CDR are summarized in Figure 22. The main drawback of the ERM series tests was that the burn time was limited by the oxidizer reservoir storage capacity to roughly five seconds. The exception is ERM-10, which was run at half the nominal oxidizer flow rate to double the burn time. One advantage of the CAMUI-type fuel grains used in the ERM series is a natural shift in equivalence ratio in time, and ability to adjust the value of equivalence ratio by the ratio of CAMUI-type fuel blocks to conventional tubular type fuel blocks. For this reason, the ERM series tests resulted in the largest span of equivalence ratios of all tests series.

The HK series was initiated as a low-cost and high-turnaround follow-on to the ERM series. The scale of the HK series was reduced to the 30N-thrust class, and the fuel grain design was simplified to conventional tubular fuel grains. Moreover, the firing duration was increased to twenty seconds to increase the amount of data that could be collected from a single test. By the time the HK series was initiated, the first versions of the NTRT procedure had been conceived and tested on the ERM series test data with success. For this reason, the effort was made to create a new test stand at Hokkaido University to allow for the measurement of thrust, multiple temperatures from within the nozzle and chamber pressure through the nozzle. The first seven HK series tests were unsuccessful, because of an issue with clogging of the chamber pressure port during firing. After increasing the size of the ignition wire leads, this was no longer an issue, and the following seven tests (HK-8 thru -14) were successful. The results of CDR are summarized in Figure 23. The motor, test stand and test procedures of the HK series tests were implemented in the DNT, SLY, QE and CBX series tests.

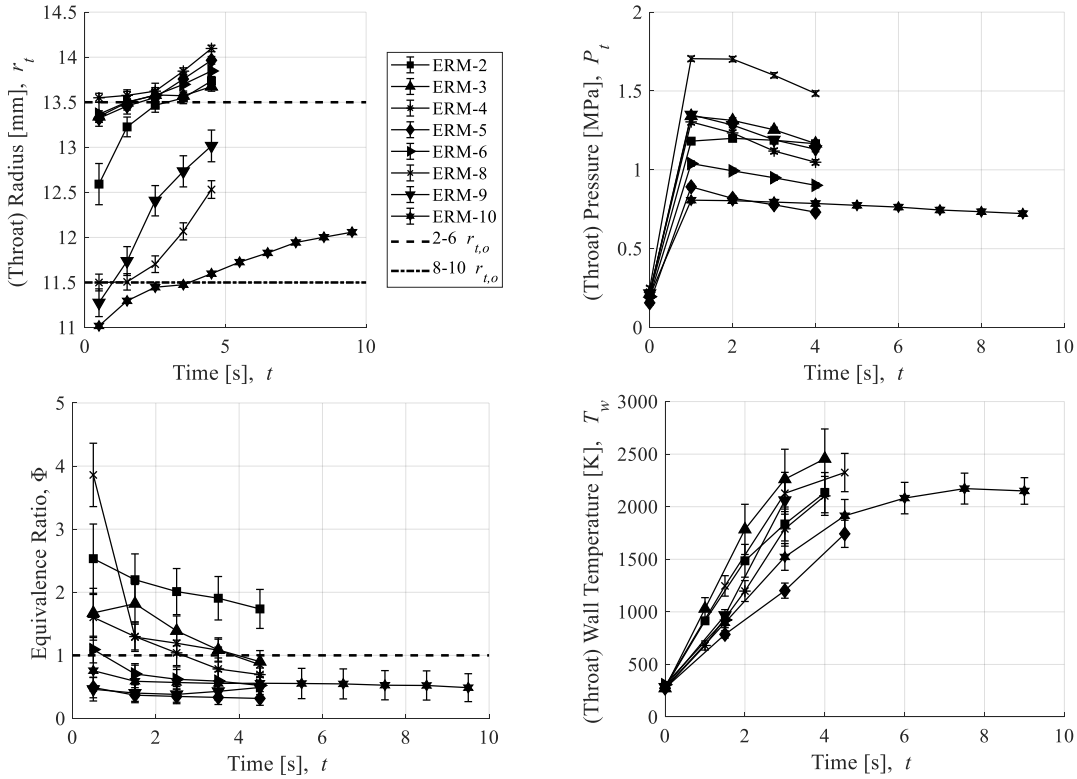

Figure 22. Results of CDR in ERM series tests.

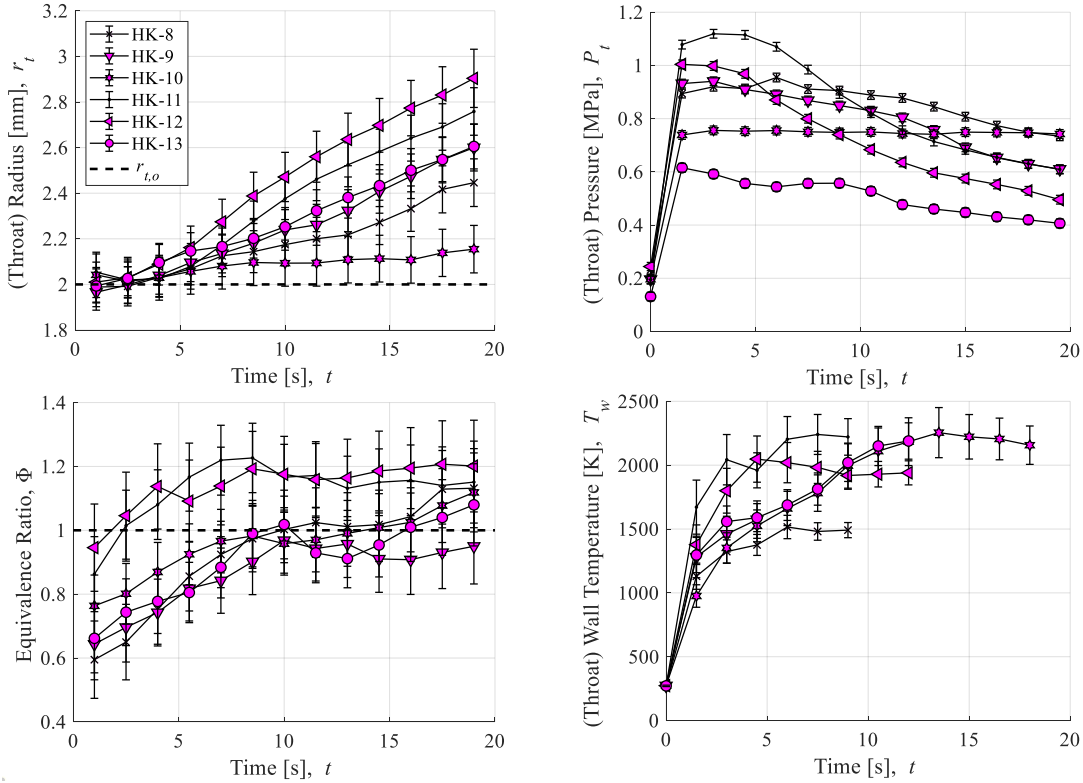

Figure 23. Results of CDR in HK series tests.

The NTRT was used to evaluate nozzle erosion in the HK series tests, which demonstrated very low c^* efficiencies, η^*. Since the NTRT operates on the assumption that η^* is constant during firing, it was not clear whether the results of the NTRT were accurate when using the HK series motor and fuel design. The DNT series tests aimed to investigate the accuracy and applicability of the NTRT by repeating tests with the same initial conditions and shutting down the tests at different times to confirm whether or not the NTRT results in the same value for η^* regardless of firing duration. Twenty-one DNT series tests were conducted, sixteen of which are considered successful. DNT-1 failed due to a leak at the pressure measurement tap, and DNT-7 thru -9 resulted in unacceptably low values of $0.5 < \eta^* < 0.6$. DNT-2 thru -6, and DNT-10 thru -20 were successful. The DNT series tests have been split into two sub groups for plotting purposes, the results of which are shown in Figure 24 and Figure 25, respectively. The lower DNT-series tests, i.e. DNT-3, 4, 6, 10 & 11, were tested with a fixed oxidizer mass flow rate of 11-12 g/s, and the upper DNT-series, i.e. DNT-12, 13, 14, 16, 17 & 18, were tested with a fixed oxidizer mass flow rate of 8-9 g/s. One informative conclusion may be drawn from these results. Even though the initial conditions of the test subgroups were similar, the timing of the onset of erosion varied between tests. The test with the most delayed onset of erosion, DNT-3, also had the lowest wall temperature history. Similarly, the wall temperature in DNT-16 thru -18 is lower than in DNT-13 and -14, which may explain the difference in erosion rates between these tests. However, DNT-2, which had the earliest onset and highest erosion rate of all tests also had a relatively low wall temperature. In DNT-2, the check thermocouple failed just after ignition, so a confirmation of this temperature history was not possible.

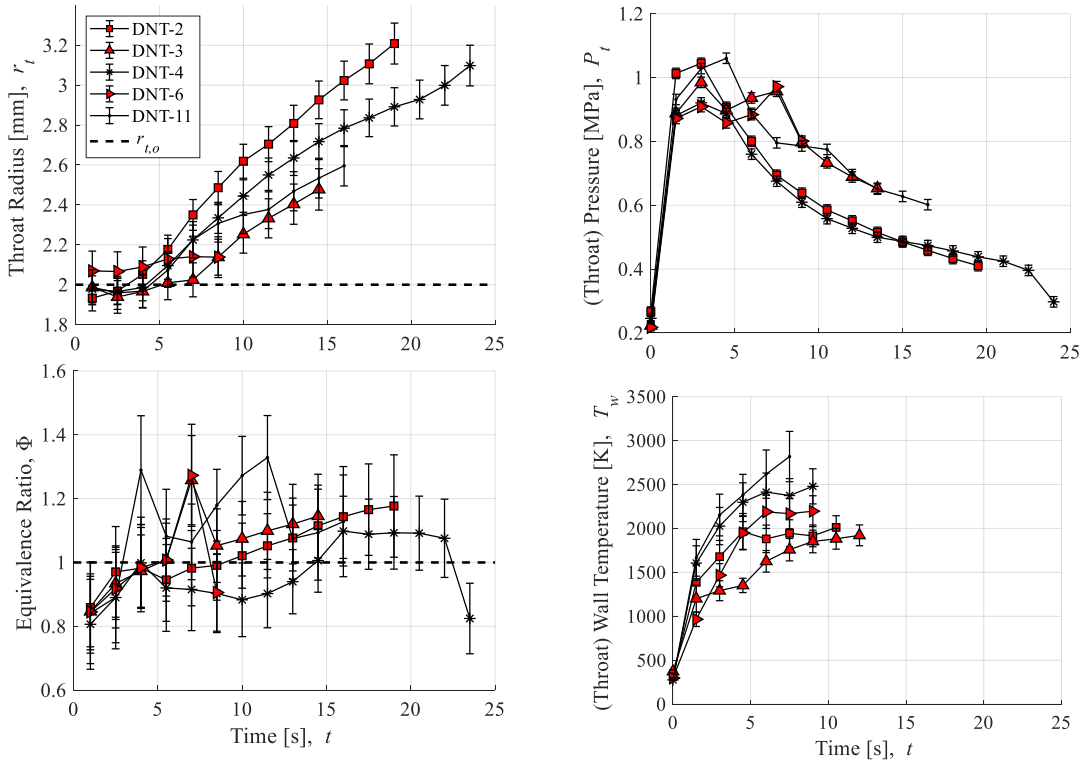

Figure 24. Results of CDR in the lower DNT series tests.

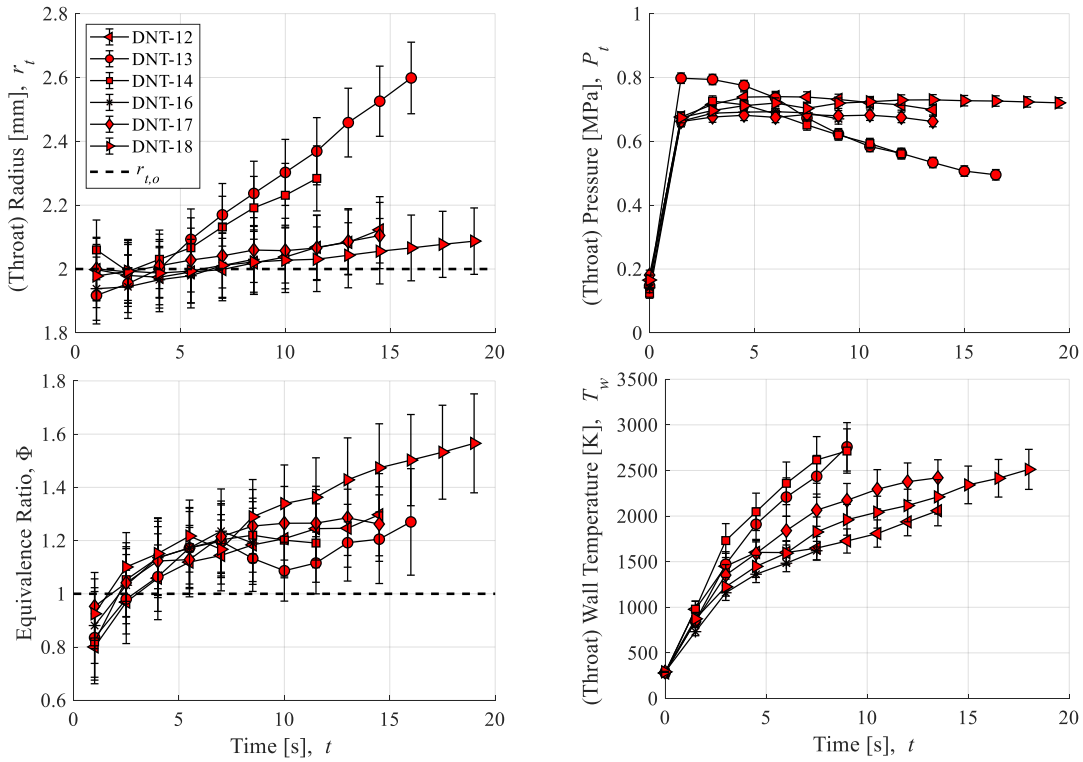

Figure 25. Results of CDR in the upper DNT series tests.

The SLY series tests were initiated in October 2016 after concluding, through the analysis of DNT series tests, that the NTRT can be used to determine the nozzle throat diameter and equivalence ratio histories with an acceptable level of experimental uncertainty. Each SLY series test used a different fuel grain design. The purpose of this variation in fuel design was two-fold: to increase the range of data collected for equivalence ratios, and to observe the effect that axial variations in fuel port diameter have on η^* and low-frequency (LF) pressure oscillations during firing. Although oxidizer mass flow rates were varied in the HK series tests, Φ only varied from 0.9 to 1.2 between tests. Due to the scale and shape of the tubular fuels, increasing the oxidizer mass flow rate resulted in a nearly identical increase in fuel mass consumption rate, thus limiting the span of equivalence ratios. In the SLY series tests, the LEGO-like fuel blocks designed for DNT series tests were mixed to create fuel grains that had variable port diameters in the axial direction. Six of the seven SLY tests were successful; SLY 4 failed to ignite and was repurposed as SLY 5. The results of CDR are shown in Figure 26. As expected, by altering the fuel shape, a larger span of equivalence ratios ($0.6 < \Phi < 1.4$) was observed than in the HK or DNT series tests. SLY-6 may explain some of the issues facing the GOX tests. SLY-6 used a 2-step increase from the main fuel port of 10 mm to an aft chamber of 30 mm. The result was a value of η^* ~85%, the largest of the GOX tests. This large efficiency may explain why the nozzle heated up faster than other tests, and erosion proceeded faster than other tests at similar pressure and equivalence ratio. It may also be possible that the efficiency is not a cause, but rather a consequence of a more turbulent flow field, which is the reason the erosion rate was larger than in other tests.

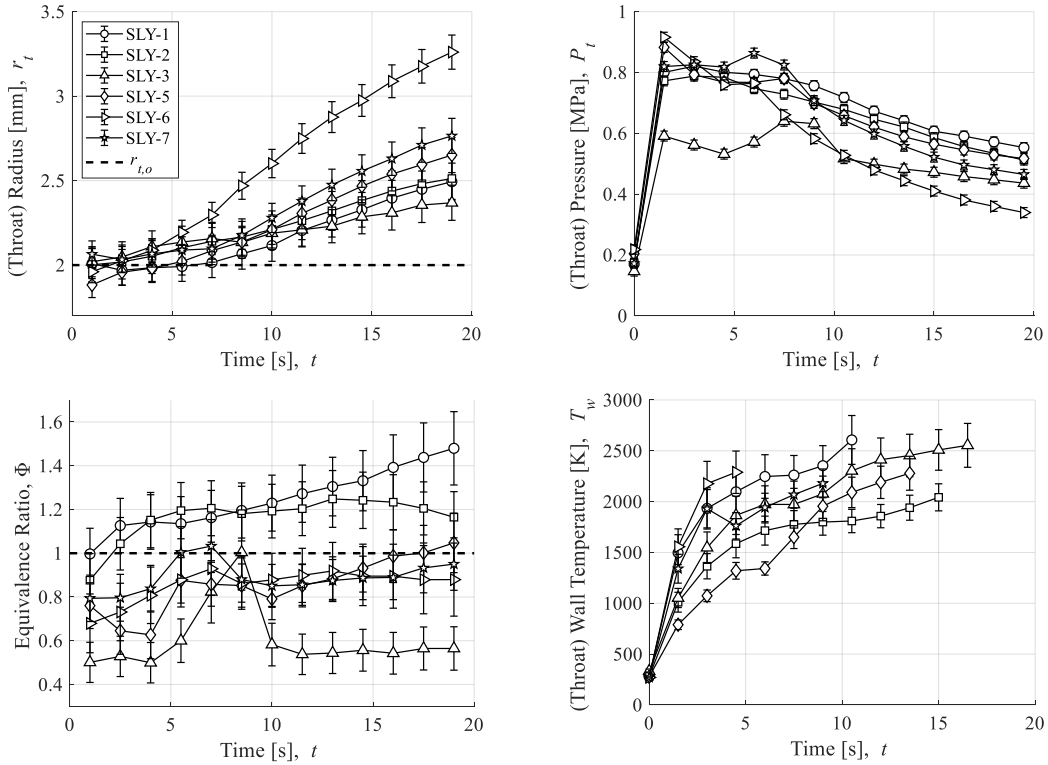

Figure 26. Results of CDR in the SLY series tests.

A review of ERM, HK, DNT and SLY tests revealed a shared tendency among all tests with measurable amounts of erosion for a conspicuous, on/off switch-like, moment when the nozzle throat diameter begins to increase by a measurable amount. Moreover, even when the test conditions were relatively similar between tests, as in the DNT tests, the time of the onset of erosion varied between tests. The QE series tests were conducted to pinpoint the conditions that lead to the onset of erosion, not by repeating tests with the same firing conditions as in the DNT tests, but by varying the flowrate between tests. Five tests were conducted, three of which are used in this study (QE-3 thru -5). QE-1 and -2 were a failed attempt to insulate the surface of the inlet of the nozzle perpendicular to the gas flow using zirconia with the aim of guaranteeing that heat conduction in the body of the nozzle would be one-dimensional in the radial dimension. The results of CDR are

shown in Figure 27. Two DNT series tests, DNT-19 and DNT-20, were adopted for comparison with the QE tests, and for this reason were not listed in the previous figures. It is clear from the plots that the conditions were very carefully controlled for. In fact, the only variation between tests is the oxidizer mass flow rate, from 8 g/s in DNT-20 to 16 g/s in QE-5. The result is a very gradual decrease in equivalence ratio and gradual increase in the heating rate of the nozzle wall. However, with the right combination of pressure, temperature and equivalence ratio, the onset of erosion in QE-5 occurred earlier and erosion proceeded more rapidly than in the tests leading up to QE-5. The next greatest erosion rate occurred in DNT-19, which had the next highest nozzle wall temperature (after 3 s), and next lowest equivalence ratio. Thus, the careful investigation of erosion onset in QE series tests confirmed our expectations.

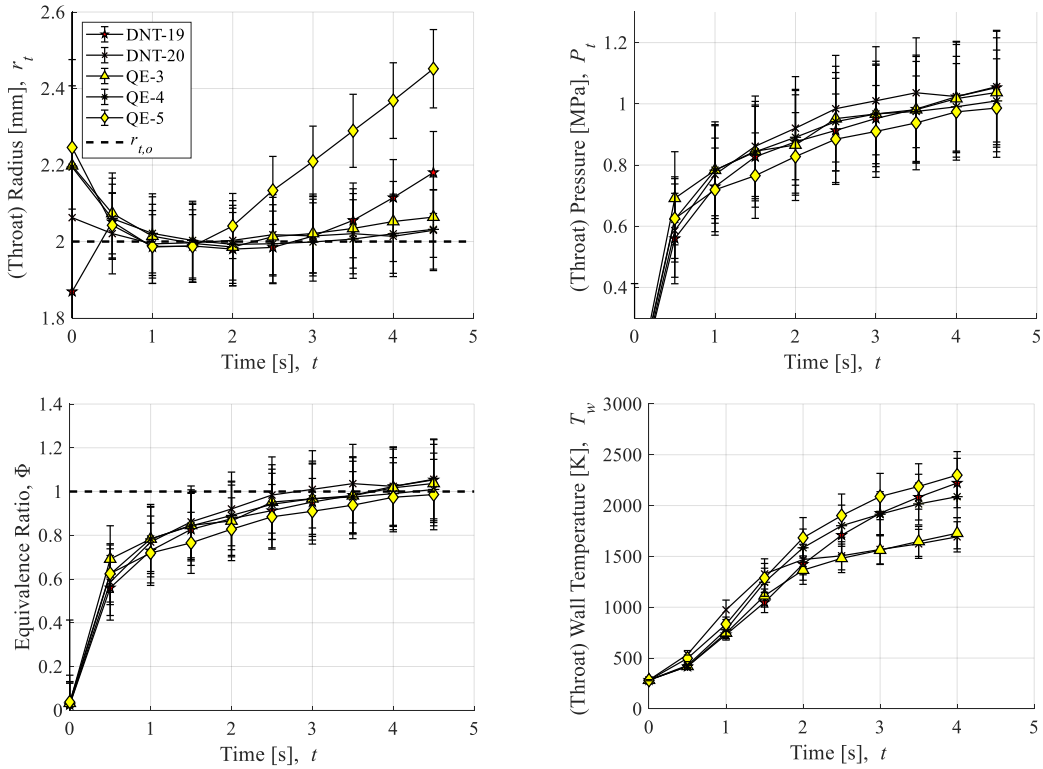

Figure 27. Results of CDR in the QE series tests.

Another interesting finding comes from the QE-4 test, which had negligibly small erosion, but appears to have been shut down just at the onset of erosion. Even though the nozzle erosion was not great enough to result in a significant increase in throat diameter, it can be seen from Figure 28 the throat has increased roughness and gouging similar to cases where a measurable amount of nozzle erosion has taken place.

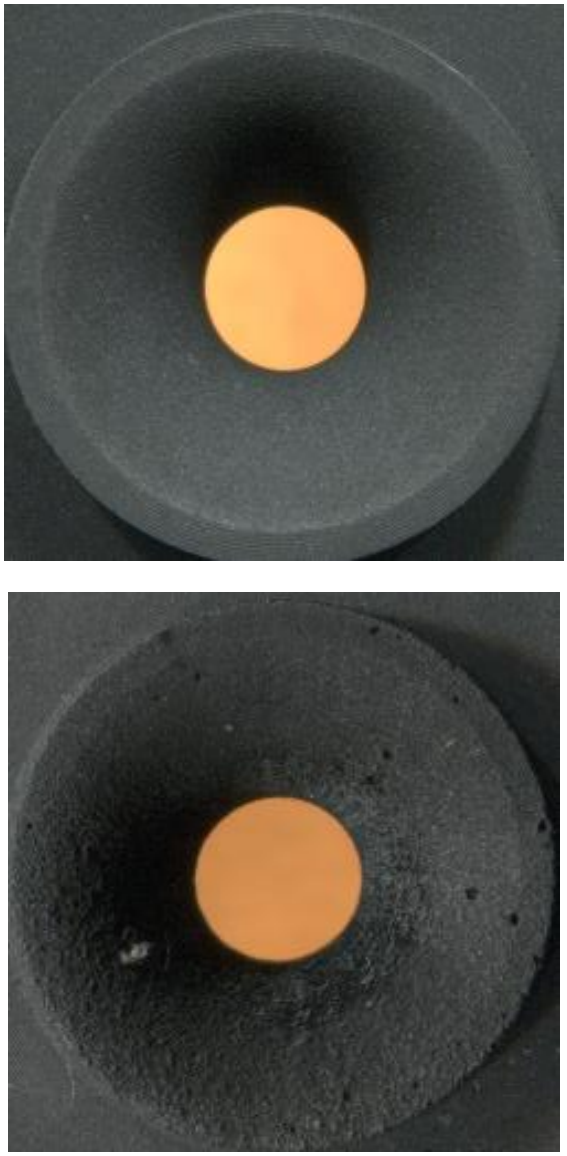

Figure 28. Increase in roughness at the nozzle throat in QE-4 before (upper) and after (lower) firing. Note: *onset appears to begin at the end of QE-4*.

The MSS series was a return to the 2kN-thrust class scale, but with the ability to conduct firing tests lasting more than twenty seconds. This was accomplished by using a more massive fuel grain, and larger oxidizer reservoir. The MSS tests were also an attempt to operate at the high-performance level necessary for flight operations. This means that the motor was designed for improved mixing, and had an enlarged aft chamber mixing space to increase residence time – i.e. designed to improve η^*. The motors were also designed to operate near the optimal Φ for maximizing I_{sp}, roughly $1.4 < \Phi < 1.6$. In this region of Φ, the mass fraction of oxidizing species is greatly reduced, meaning that nozzle erosion was expected to take place at a slower rate than in the previous series. However, when erosion did occur in the MSS series tests, it caused a positive feedback that increased oxidizer mass flowrate faster than fuel mass consumption rate, leading to decreases in Φ, which in turn further increased the erosion rate. This was a consequence of the feed system and fuel design. Nine of ten MSS tests were successful, MSS-1 failed due to the thermal failure of an O-ring in the injector manifold. MSS-2 thru -7 were conducted with the DNT series test procedure, whereas MSS-8, -9 and -12 were isolated tests. Nozzle temperatures were not measured in MSS-2 thru -6. However, due to the high repeatability of MSS-2 thru -7, the temperatures measurements of MSS-7 were substituted into MSS-2 thru -6 analysis. MSS-10 and -11 were planned for but never carried out due to time and budget constraints. The results of CDR are shown in Figure 29. The MSS tests benefited from a combination of the equivalence ratio shift of CAMUI-type fuel grains, as well as the erosion progression analysis of the DNT series tests. The erosion rate increases in time even when pressure decreases, because the pressure decrease causes an oxidizer flow rate increase, which in turn decreases the equivalence ratio. As the equivalence ratio moves towards the oxidizer

rich region, the erosion rate continues to increase. The result is a simultaneous loss of specific impulse, pressure and thrust predictability, all of which are detrimental to the operation of chemical rockets in practice.

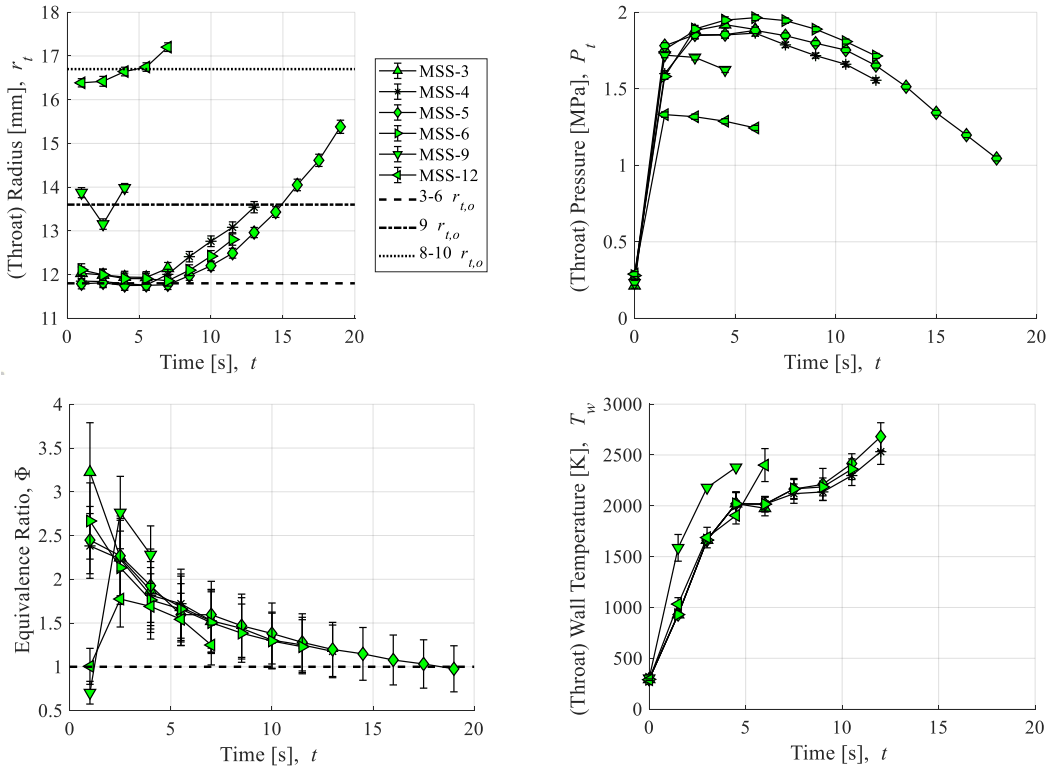

Figure 29. Results of CDR in the MSS series tests.

The CBX series tests were conducted concurrently with the MSS series tests. The CBX series was conducted at Hokkaido University, while the MSS series was conducted at Uematsu Electric Company. Essentially, the CBX tests are a repeat of the DNT series, using liquid N_2O as oxidizer rather than GOX. The results of the N_2O tests are broken down into two sub-groups of the same series: the lower CBX-series tests, and upper CBX-series tests. The lower CBX-series tests, i.e. CBX-4 thru -9, and upper CBX-series tests, i.e. CBX-10 thru -14 & 16, were conducted to test the repeatability of the $NTRT^+$ and observe

the progression of nozzle erosion in time when using N_2O as the oxidizer. The initial oxidizer mass flow rate was designed to be around 40 g/s, but increased in response to nozzle erosion, as explained in Section 1.2. The fuel grain of the upper CBX-tests was shorter than the lower CBX-tests for the same oxidizer mass flow rate to reduce the equivalence ratio. The results of these tests are shown in Figure 30 and Figure 31, respectively. The influence of equivalence ratio on nozzle erosion rate is evident by comparing the results in these two figures. The maximum increase in throat radius of the lower CBX tests, which have an equivalence ratio between 1.6 and 2, is roughly 0.4 mm, whereas the maximum increase in throat radius of the upper CBX tests, which have equivalence ratio between 0.8 and 1.4, is four times higher at 1.6 mm. Interestingly, the throat wall temperature histories are similar between tests. This may be explained by the fact that the mass flowrate is larger for the lower CBX tests even through the adiabatic flame temperature is slightly lower – the opposite being true for the upper CBX tests. CBX-7 shows an interesting result in that the nozzle throat radius appears to level-off near the end of firing. It is not clear if the erosion rate would increase again after this leveling-off, but, in the absence of additional nozzle heating, equivalence ratio shift and pressure increase, there should be no reason for the erosion rate to increase again. It is entirely possible that CBX-7 is a case where nozzle erosion is "self-terminating," such that the erosion results in a negative feedback to the conditions of erosion. Since it is hard to believe that the nozzle cooled down in the absence of external cooling, it is most likely that the decrease in P_t to 2 MPa was enough to slow the erosion rate to nearly zero. However, in CBX-16, erosion continues to occur even after P_t decreases to 1 MPa. Thus, the conditions of erosion onset/offset, clearly depend on some combination of T_w, P_t and Φ.

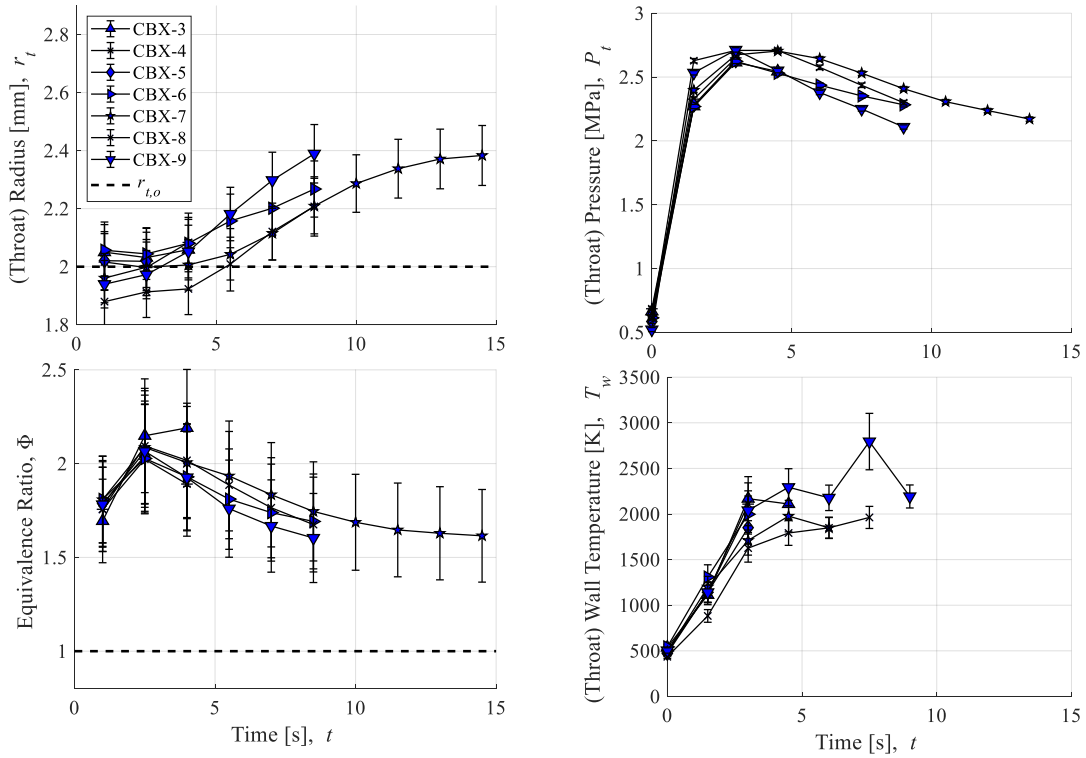

Figure 30. Results of CDR in the lower CBX series tests.

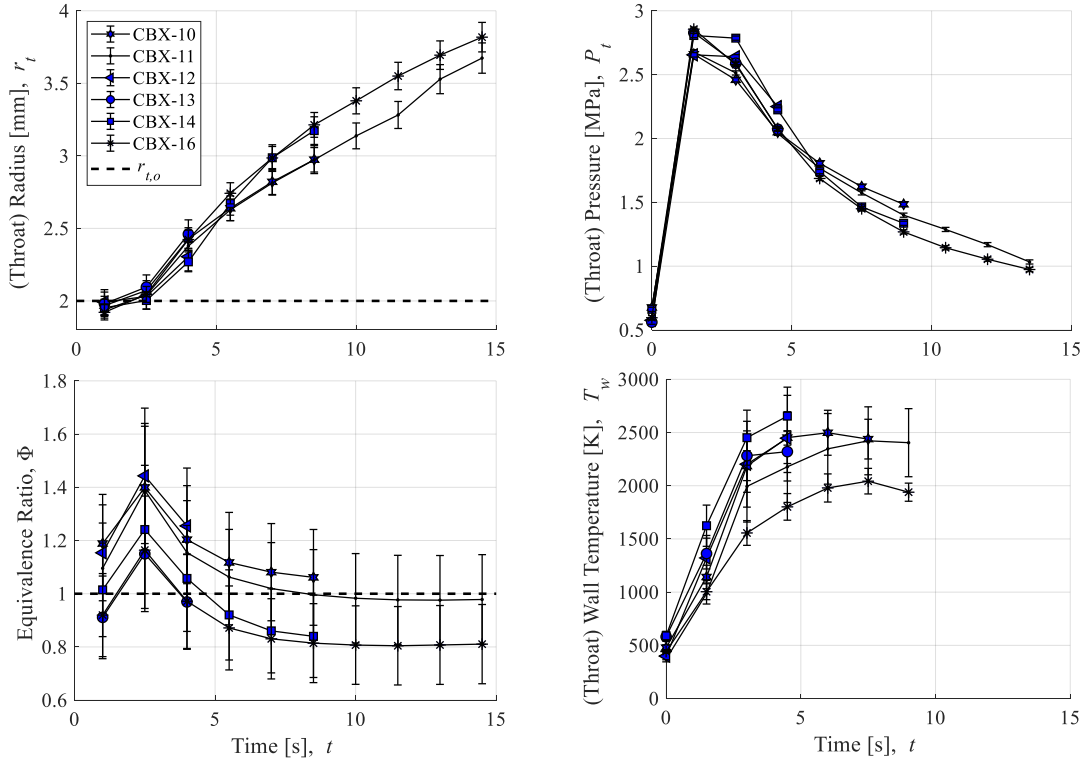

Figure 31. Results of CDR in the upper CBX series tests.

5.2 Comparison of Results of the NTRT and Analytical Model

Prior to this research, the only readily available tool for the prediction of graphite nozzle erosion in hybrid rockets were the governing equations and calculation methodology of Delaney et al. [28] and Ozawa et al. [46] that are introduced in CHAPTER 2. This research is the first time in open literature that the accuracy and applicability of these models will be rigorously examined against static firing test results. Since the model is indifferent to which oxidizer is used, all experimental data can be compared together. Recall that the model acts as a functional "black box", where the erosion rate is the output and the throat diameter, pressure, wall temperature, equivalence ratio and nozzle density are the inputs:

$$\dot{r} = f\left(d_t, P, \rho_n, T_w, \Phi\right)$$

Since the nozzle wall temperature histories tend to get cut short due to thermocouple failure during firing, an approximation of nozzle wall temperature had to be implanted in this analysis. The first thermocouple to fail due to overheating is the one placed closest to the nozzle throat. In the Hokkaido University tests, this depth is 5 mm from the throat, and in the Uematsu Electric Company tests, this is 10 mm from the throat. In either case, when the thermocouple fails, it is happening when the nozzle throat wall temperature has already exceeded 2000 K. Thus, numerical integration of the model predictions will be carried out for the entire burn time of a test, assuming the wall temperature remains at the highest value recorded before thermocouple failure for times beyond this failure. In this way, the overall nozzle throat erosion can be calculated using the model and compared with the measured result for each test, along with nozzle erosion histories.

5.2.1 Comparison of Measured and Predicted Erosion Histories in GOX Tests

The results of the GOX tests are shown in Figure 32, where the upper two figures are a comparison of the overall erosion before and after firing, and the lower four figures are the histories of erosion. The analytical model can predict roughly the correct erosion rate in tests where nozzle erosion rate is noticeably large, but is unable to predict the lack of erosion observed in DNT-16 thru -18. Recognizing that the diameters, pressures and equivalence ratios are very similar between all DNT tests, the only explanation is the effect of nozzle temperature. Either the nozzle temperature measurement is consistently inaccurate, or the model cannot account for the low erosion rates observed at lower temperatures.

The HK-series and SLY-series tests result is a large range of equivalence ratios, and an equally large variation in erosion rates. In the HK-series tests, as in the DNT-series tests, the analytical model never replicates the cases where erosion rate is relatively small. This problem is not as pronounced in the SLY tests, because the erosion rates are consistently high. A careful inspection of all erosion history plots reveals that although some model prediction plots line up well with an experimental measurement trace, the two plots may not be for the same test. For example, the SLY-1 model prediction agrees well with the measurement history of SLY-6, whereas this predicted erosion rate is twice as high as the measured value for SLY-1. The model predicts no variation in the QE series tests, which means either that the model is not sensitive enough to the conditions at the onset of erosion, or the large range of erosion rates observed in the tests is the result of experimental uncertainties, and slight variations in test conditions.

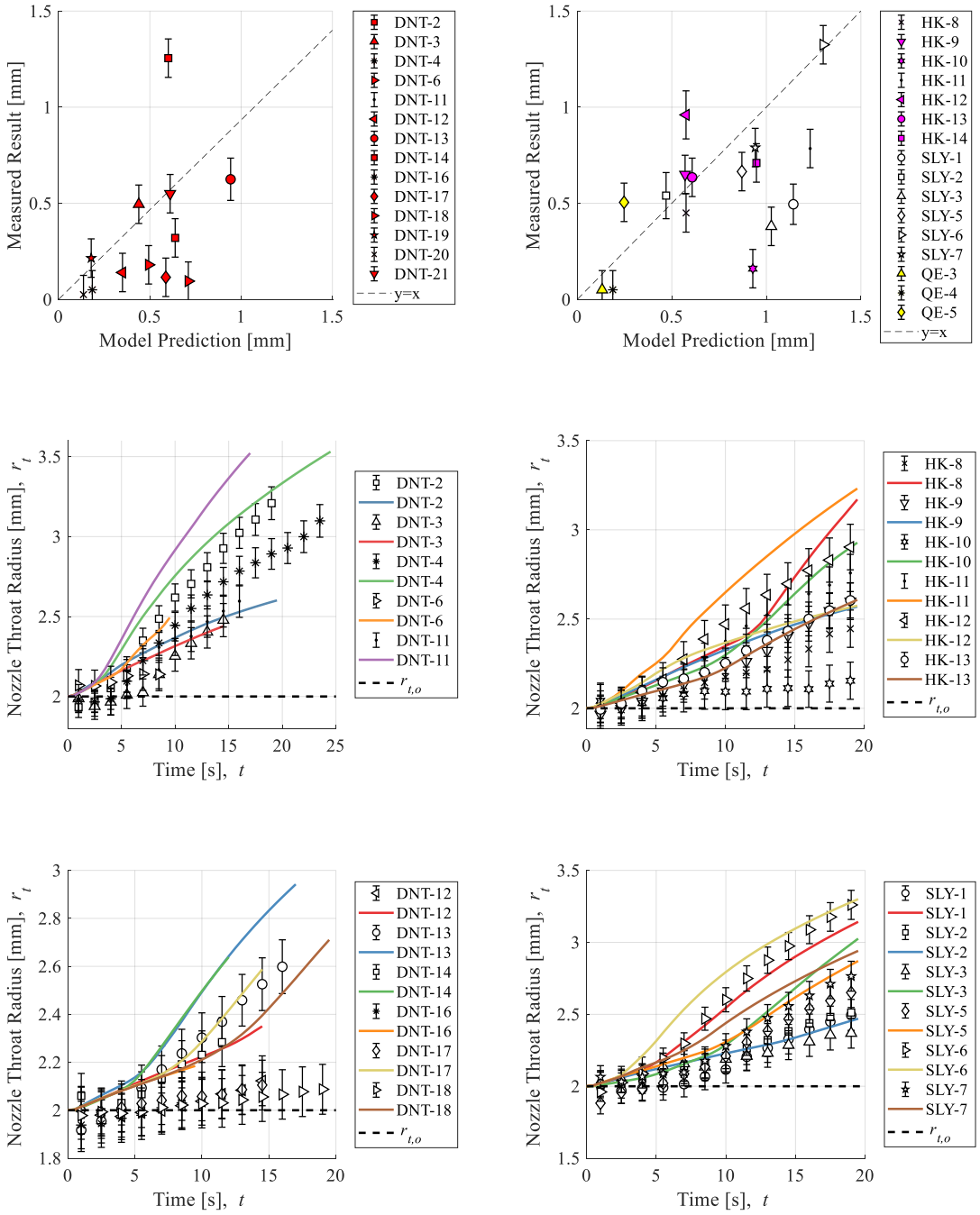

Figure 32. Model (solid lines) overpredicts measured erosion histories (markers) in GOX tests. *Upper left and right figures compare overall erosion, and the lower four figures compare erosion histories.*

5.2.2 *Comparison of Measured and Predicted Erosion Histories in N_2O Tests*

The model predictions (plotted by in colored solid lines) for the CBX-series tests are only slightly better correlated than the GOX tests, as shown in Figure 33. The general trends in erosion histories are similar between the model predictions and experiments, with a high erosion rate at the onset of erosion followed by a gradual decrease in erosion rate as chamber pressure decreases. However, with the exceptions of CBX-9 and CBX-14, there is poor agreement between the prediction and experimental result of any given test.

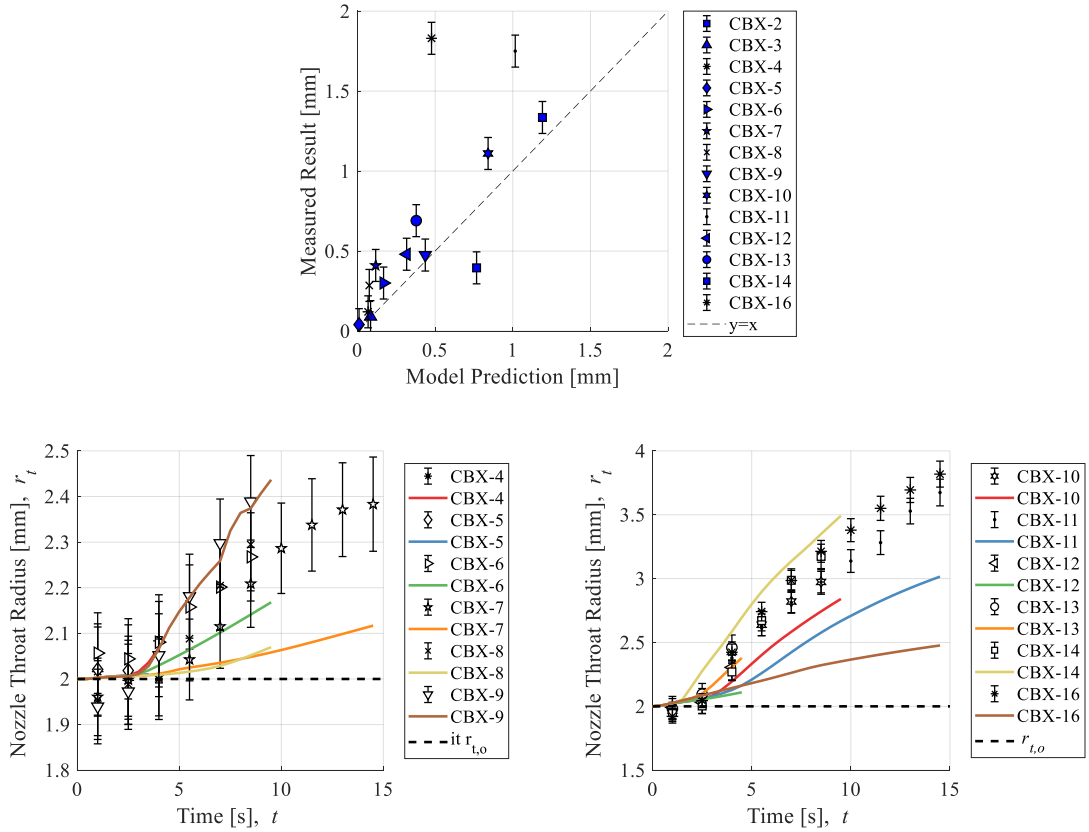

Figure 33. Model (solid lines) underpredicts measured erosion histories (markers) in N_2O tests. *Upper figure compares overall erosion, and the lower two figures compare erosion histories.*

5.2.3 Comparison of Measured and Predicted Erosion Histories in LOX Tests

The model predictions (plotted by in colored solid lines) for the LOX tests are worse than the N_2O tests, as shown in Figure 34. However, there are two interesting findings to point out of the LOX test results. First, the onset of erosion is well replicated, which suggests that it is the diffusion rate that is being underpredicted. Second, the underprediction by the model is well replicated between tests, such that doubling the predicted erosion rate would lead to good agreement with the measured values for overall erosion. This suggests that there is a fundamental flaw in the modeling of mass diffusion, particularly pertaining to this scale.

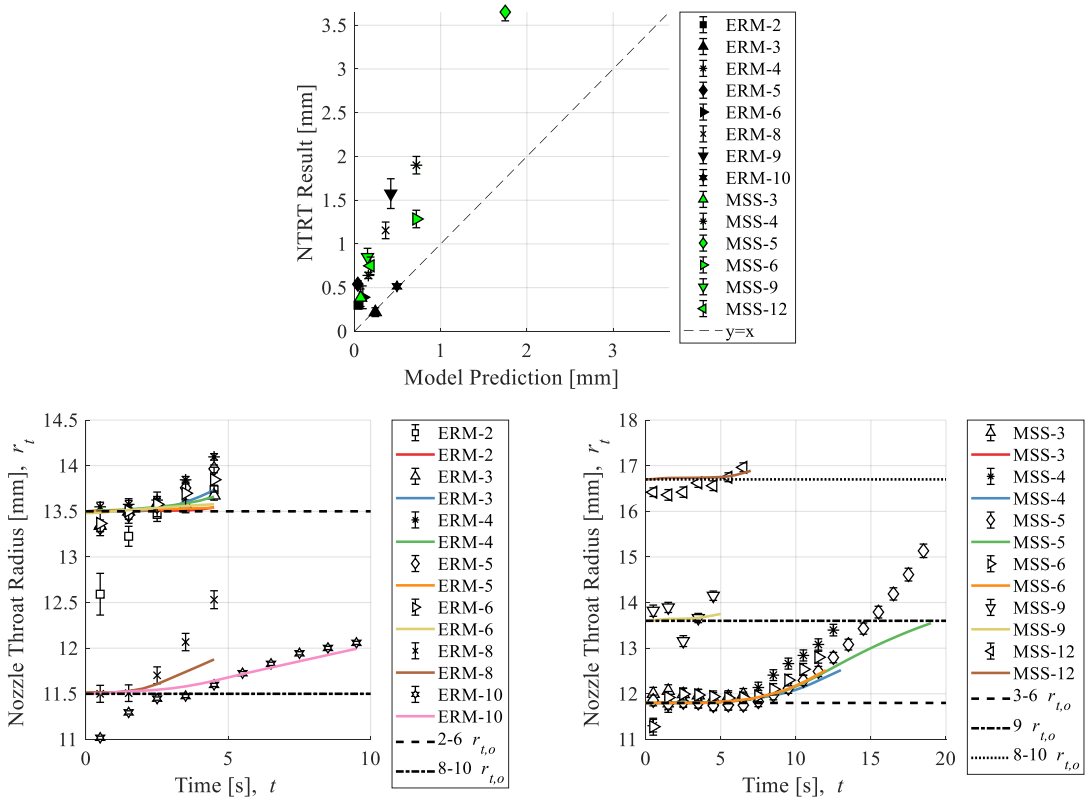

Figure 34. Model (solid lines) underpredicts measured erosion histories (markers) in LOX tests. *Upper figure compares overall erosion, and the lower two figures compare erosion histories.*

The model predictions for erosion history are less sporadic in the LOX tests than in the GOX or N_2O tests. Furthermore, the experimental histories are consistently underpredicted by the model. It is interesting to point out that the onset of nozzle erosion is generally well predicted. This is especially clear in the MSS-2 thru -6 tests, because the experimental erosion histories show a distinct time of erosion onset at around 6 seconds in the burn, after which time erosion rate sharply increases. Although the timing of this onset is replicated, the rate of the onset of erosion and subsequent erosion rate is not. Seeing as the GOX tests were generally overpredicted, and the LOX tests underpredicted, the discrepancy in the analytical model may be an issue related to scale, such as in the Sherwood number correlation for boundary layer thickness, or effect of size and mass on the thermal properties of the nozzle etc.

5.3 Empirical Formulations of Test Results

In this section, the large body of data from the static firing test campaign will be applied to the three novel empirical formulas developed in Section 2.3. Erosion rates are approximated from the NTRT results for nozzle throat radius history. This is done by taking the numerical derivative at intervals of 0.5 s. To avoid negative values for nozzle erosion due to start-up transients in the erosion histories, erosion onset times were specified manually through inspection of the NTRT results for nozzle throat history, and the nozzle throat radius were defined to be the initial value until the designated time at onset. This means that nozzle erosion rate is defaulted to zero until the specified erosion onset time. Note that the designated erosion onset times are listed in Table 8 as t_{on} [s].

For the sake of empirical correlation, data were separated into two groups, data from tests using oxygen as the oxidizer and data from tests using nitrous oxide as the oxidizer. For each of the three empirical formulas, correlations were carried out separately for these two groups of data. The results of correlation are summarized in Table 5.

Table 5. Results of empirical correlation.

Based on 773 data from O_2 tests	Based on 167 data from N_2O tests
The Analytical Model: R2 = 0.26	
Functional Formula (2-17): $\rho_n \dot{r} = \dfrac{\beta_1 \Phi^{\beta_2} \exp(\beta_3 \Phi) T_w^b P^n \left[1 - \ln(d_t)\right]}{1 + \exp\left(-(T_w - E_1)/E_2\right)}$	
Initial guess: $\beta_1 = 1; \beta_2 = 2; \beta_3 = -3; b = 0.6; n = 0.6; E_1 = 2300; E_2 = 180$	
R2 = 0.35	R2 = 0.77
$\beta_1 = 3.84 \times 10^{-7}; \beta_2 = 2.15; \beta_3 = -3.67;$	$\beta_1 = 2.99 \times 10^{-5}; \beta_2 = 4.32; \beta_3 = -5.40;$
$b = -1.59; n = 2.03; E_1 = 2184; E_2 = 188$	$b = 0.01; n = 0.88; E_1 = 1397; E_2 = 32.8$
Circuit Analog Formula (2-24): $\dfrac{\rho_n \dot{r} \delta}{(\rho D)_w} = \dfrac{Y_\delta / 2}{1 + \dfrac{\exp(E/T_w)}{\beta_1 \Phi^{\beta_2} \exp(-\beta_3 \Phi) T_w^b P^n} \dfrac{(\rho D)_w}{\delta}}$	
Initial guess: $\beta_1 = 1; \beta_2 = 2; \beta_3 = 3; b = -0.5; n = 0.5; E = 2000$	
R2 = 0.12	R2 = 0.73
$\beta_1 = 2.97 \times 10^{-4}; \beta_2 = -6.53; \beta_3 = -5.94;$	$\beta_1 = 0.0053; \beta_2 = -2.46; \beta_3 = 0.69;$
$b = -1.72; n = 1.49; E = 14514$	$b = -0.004; n = 0.76; E = 7313$
Modified Arrhenius Formula (2-25): $\dfrac{\rho_n \dot{r} \delta}{(\rho D)_w} = \beta_1 \Phi^{\beta_2} \exp(\beta_3 \Phi) T_w^b \exp(E/T_w) P^n$	
Initial guess: $\beta_1 = 1; \beta_2 = 1; \beta_3 = 1; b = 0; n = 0; E = -2300$	
R2 = 0.33	R2 = 0.81
$\beta_1 = 4.44; \beta_2 = -1.45; \beta_3 = 0.036;$	$\beta_1 = 2.23; \beta_2 = 0.84; \beta_3 = 2.68;$
$b = -2.34; n = 1.37; E = -8981;$	$b = -0.21; n = 0.20; E = -3155;$

These correlations were carried out using the method of least squares. This method can be problematic in that the initial guesses greatly change the results of correlation. Due to the large number of fitting constants, five in the circuit analog and seven in the functional formula, it is not clear if the best initial guesses were used or not. A brute force calculation was attempted, but since the magnitude of one of the constants always depends on that of another, the range of values that is needed to be tested was computationally unreasonable. One obvious finding is that the tests using N_2O as the oxidizer (i.e. CBX series tests) had relatively successful correlations for all three formulas. This is ascertained from the R2 value, known as the coefficient of determination. When R2 is unity, it means that the correlation infinitely outperforms the mean of the data set. A value of zero means that the mean of the data infinitely outperforms the correlation. Interestingly, the worst performing formula is the analytical model of Section 2.2. Even though the analytical model consists of a more detailed and elaborate consideration of the reaction-diffusion process of separate species, this model is outperformed by any one of the empirical formulas which treat the combustion gas as a single oxidizing agent. Of the empirical formulas, the modified Arrhenius-type formula originally suggested by Kamps et al. in [47] and the Functional formula performed satisfactorily. For the sake of brevity, only the results of modified Arrhenius formula will be shown graphically. Figure 35 has been added to demonstrate what the data set looks like following the least squares procedure, and how well the correlation minimizes the residual. The three independent variables are Φ, T_w, and P_t, and the dependent variable is the nondimensionalized erosion rate. The least squares method attempts to adjust the fitting constants such that the correlation results in blue overlap the

CDR results in red. Although the correlation appears to satisfactorily match the blue and red, as listed in Table 5, the R2 value is only 0.33 for this correlation.

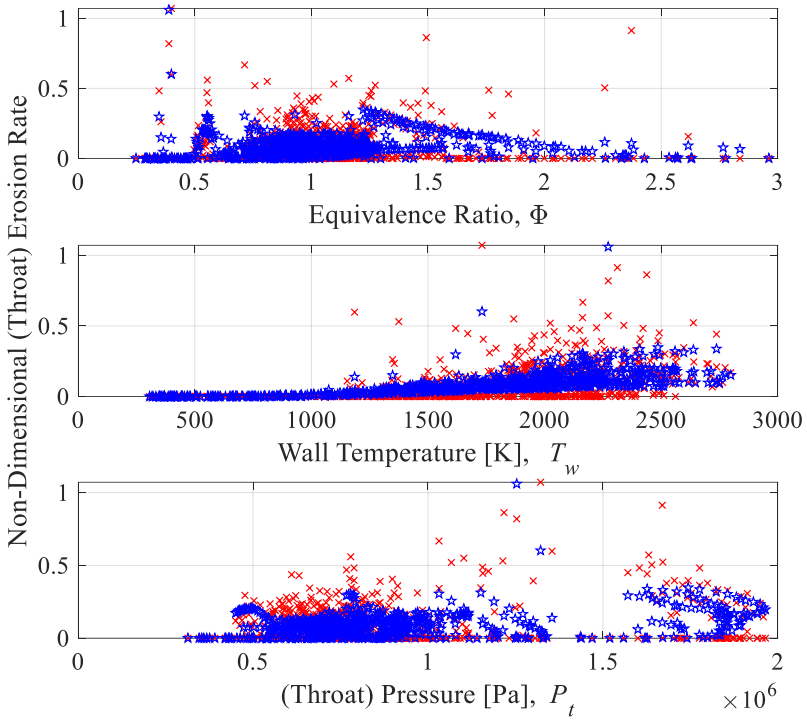

Figure 35. Correlation procedure: modified Arrhenius formula for O_2 tests. *CDR results in red; correlation results in blue.*

The plots in Figure 36 make it easier to visualize the discrepancy between measured and calculated values, as well as compare the results of the N_2O tests (i.e. CBX) and O_2 tests (i.e. all others). The solid black dots, which represent erosion rates from N2O tests, have a correlation along the $y = x$ (ideal) line, whereas the light red "x" markers, which represent O_2 tests, do not. This is reflected in the R2-values as previously mentioned.

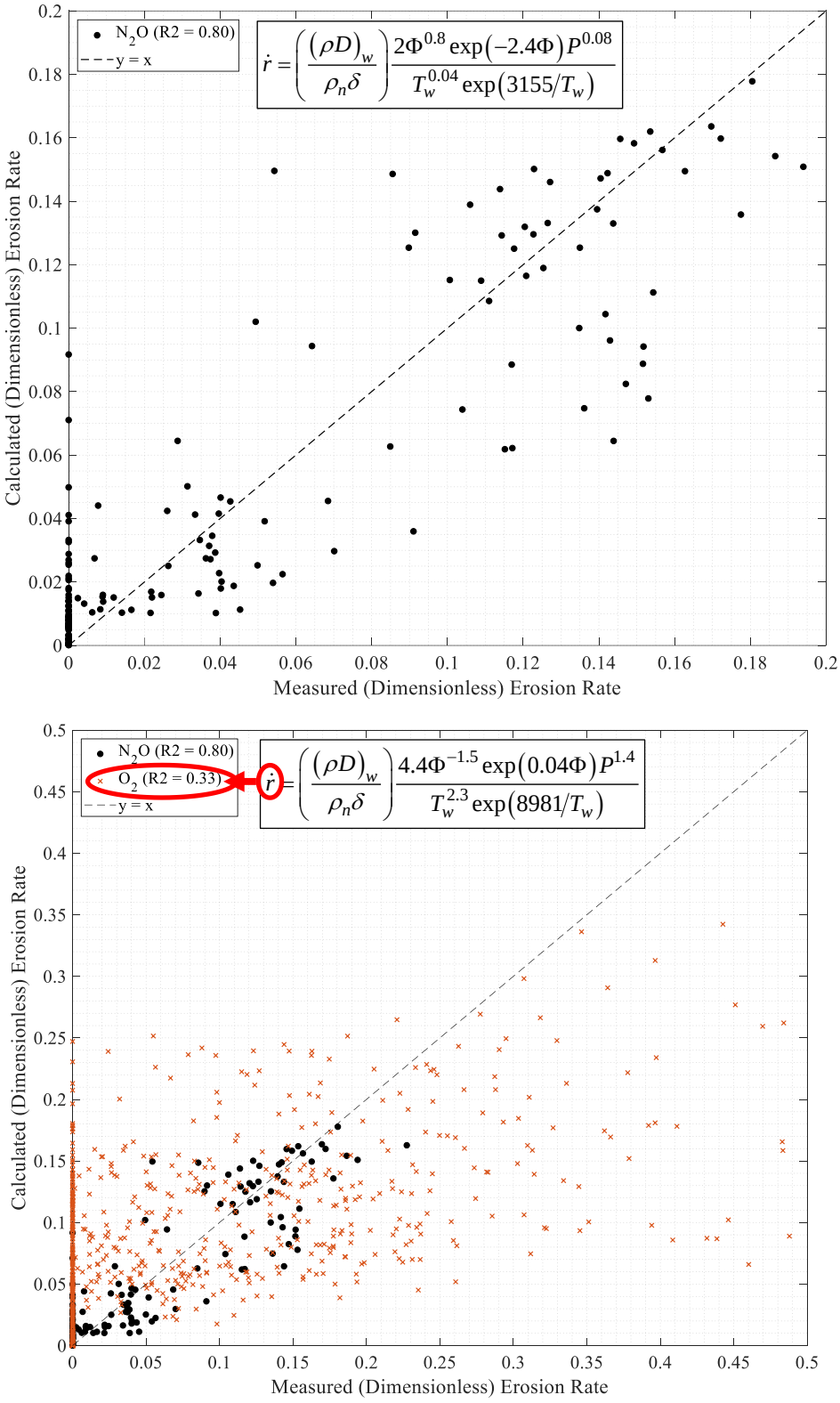

Figure 36. Erosion rate (modified Arrhenius) correlations: *(upper) N_2O tests only; and (lower) all tests.*

Figure 37 shows the agreement between measured values for overall erosion (in mm) and the results by integrating the modified Arrhenius formula in time, as was done in Section 5.2 using the analytical model. Considering that the numerical integrations relied on the projection of wall temperature data beyond the death of the thermocouples, the satisfactory correlation of overall nozzle throat erosion to an R2 value of 71% is quite remarkable. This agreement means that temporal oscillations in erosion rates as determined from the results of the NTRT can explain, in part, the scatter of plots in Figure 36.

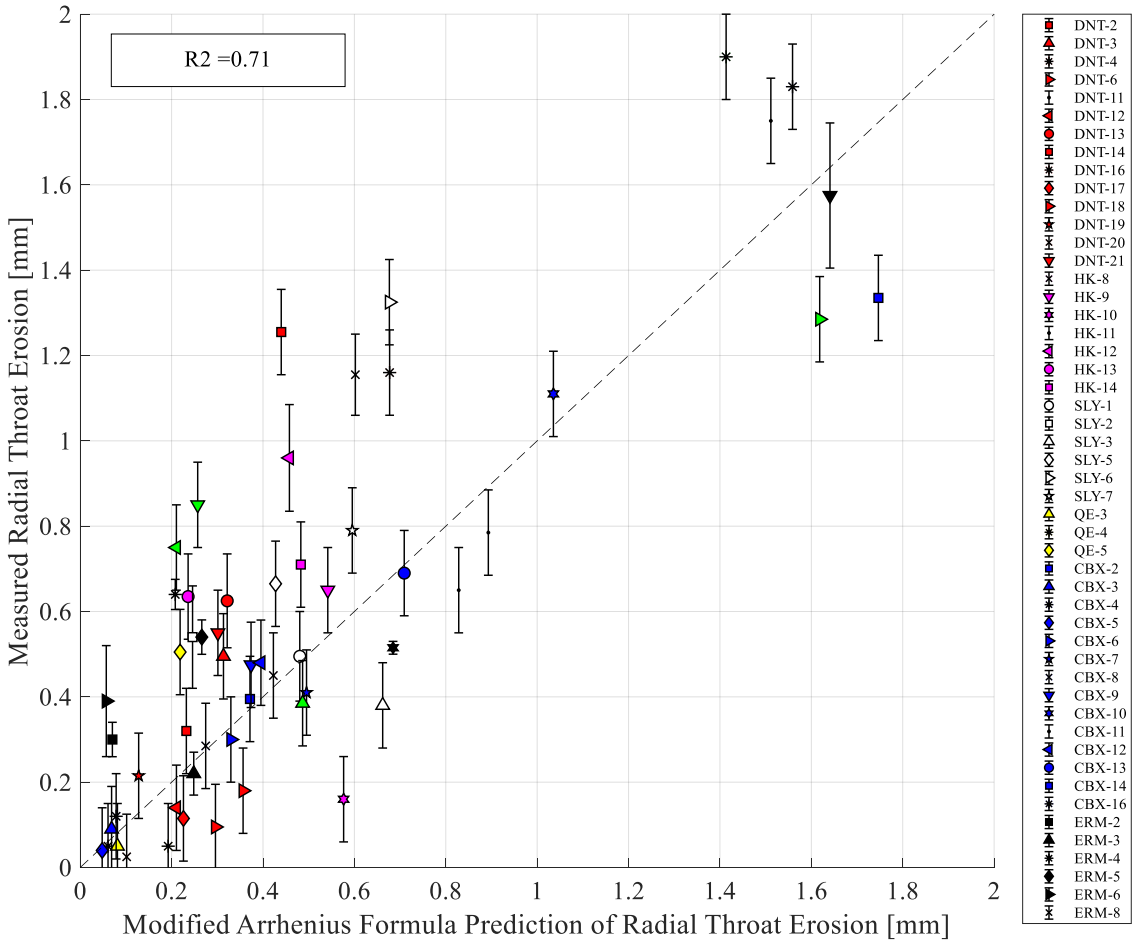

Figure 37. The modified Arrhenius formula results in the best correlation.

5.4 Discussion of Functional Dependencies and Erosion Onset Conditions

5.4.1 Functional Dependencies of Empirical Formulas

For the first time in open literature, hundreds of experimental data for graphite erosion rate were correlated with Φ, T_w, and P. An analytical model based on carbon combustion and gas diffusion theory was shown to be inadequate for the prediction of erosion. Three novel empirical correlations were carried out, showing satisfactory agreement with experimental results. Here the functional dependencies of erosion rate will be re-examined to discuss the meaning of these findings. The P-dependency of erosion is straight forward, it scales linearly with gas density, and to the power of exponent n. The dependencies of Φ and T_w are more convoluted. The relative magnitude and shape of Gamma distribution-type function $\beta(\Phi)$ is not intuitive, nor is the mass diffusion term $(\rho D)_w/\delta$. which is also expected to depend on Φ, T_w, and P. Figure 38 was created to examine these dependencies, and compare the results of empirical formulation.

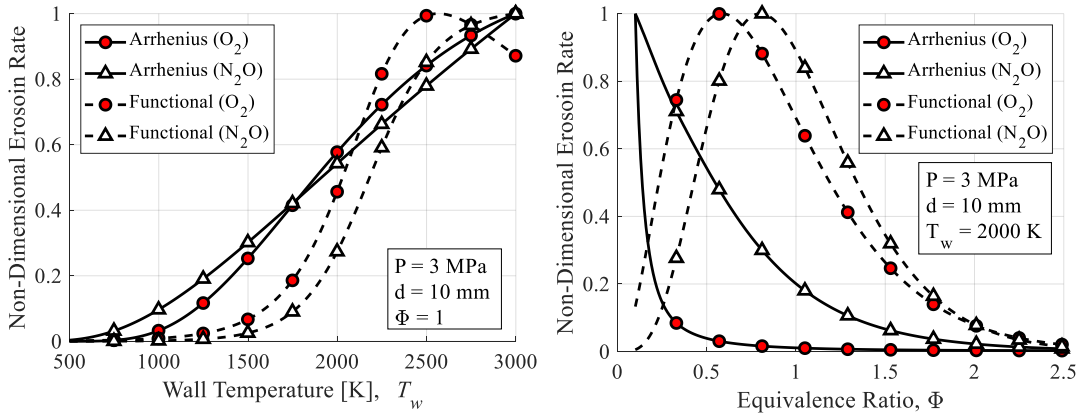

Figure 38. Review of functional dependencies in the empirical formulas.

In these figures, the functional formula and modified Arrhenius type formula are compared. The circuit analog formulas were not as highly correlated, and the functional form of the circuit analog is like the Functional formula, so the comparison of only these two formulas is satisfactory for the purpose of this review. The first noticeable difference between the formulas is the temperature at which nozzle erosion begins. The Functional formula predicts a sudden onset of erosion around $T_w \sim 1500$ K, whereas the Arrhenius type formula predicts a more gradual onset of erosion in the range of $1000 \text{ K} < T_w < 1500$ K. Both formulas reach 60% of the maximum erosion rate around 2000 K, and approach their maximums in the range $2500 \text{ K} < T_w < 3000$ K, although the modified Arrhenius formula shows less of a difference between the oxidizers than the Functional formula. Further research in the range of temperatures $1000 \text{ K} < T_w < 1500$ K seems most important for the prospect of nozzle cooling, seeing as that the Functional formula suggests that nozzle erosion is almost completely preventable for graphite cooled to less than 1500 K, while the modified Arrhenius formula requires cooling down to 1000 K. This difference of 500 K in cooling requirement is substantial given the high heat transfer rates in chemical rockets. The Functional formula also shows a dependency on Φ that matches the expectations of the analytical model and its analysis in Section 2.2. Here a major discussion point of the modified Arrhenius formula is revealed, because the formula contains no inherent limitation on erosion rate in very oxidizer rich conditions around $\Phi < 0.5$. In an actual hybrid rocket motor, the combustion gas temperature will not be hot enough to heat the nozzle wall to 2000 K in this region, as is evident in Figure 8 of Section 2.2. However, the modified Arrhenius predicts that if there were a super-rich combustion gas exposed to a graphite nozzle at 2000 K, exponential large reaction rates can be expected.

5.4.2 The Erosion Onset Factor

The discussion of results will conclude with the introduction of a new term, referred to as the "erosion onset factor," and designated by the Greek alphabet, Π. The erosion onset factor emerged from a correlation of temperature, pressure and mole fraction of oxidizing species at the time of the onset of erosion. The onset of erosion can be thought of as a chemical-kinetic-limited process. Referring to the circuit analog, the chemical-kinetic erosion resistance decreases must faster than diffusion resistance just after ignition in a chemical rocket. Combustion occurs rapidly after ignition, resulting in an energetic gas mixture at the throat, while nozzle heating occurs much less rapidly. The process of transient heating in a nozzle equates to a transition from chemical-kinetic-limited erosion towards diffusion-limited erosion. The same is true for the tests conducted in this study, which is evident from the plots of nozzle throat radius history in Section 5.1. In tests in which nozzle erosion occurs, nozzle erosion beings to occur at a measurable rate at some time (between 2-10s) after ignition.

The assumption that erosion is chemical-kinetic-limited at the time of onset allows for the approximation that the mass fraction of oxidizing species at the wall is the same throughout the concentration boundary layer, i.e. $Y_w \cong Y_\delta$. Thus, the modified Arrhenius formula becomes:

$$\rho_n \dot{r}\left(t_{on}\right) = \beta\left(\Sigma Y_{i,\delta,on}\right) T_{w,on}^{b} \exp\left(-E/T_{w,on}\right) P_{on}^{n}$$

Furthermore, the erosion rate at the onset of erosion is much lower than the erosion rate at subsequent times. Thus, variations in erosion rate between tests at the onset of erosion are

negligibly small, and the erosion rate can be treated as a constant. Thus, we can define the erosion onset factor to be Eq. (5-1.):

$$\Pi \equiv \frac{\rho_n \dot{r}\left(t_{on}\right)}{\beta\left(\Sigma Y_{i,\delta,on}\right)} = T_{w,on}^{b} \exp\left(-E/T_{w,on}\right) P_{on}^{n} \cong f\left(\Sigma Y_{i,\delta,on}\right) \qquad (5\text{-}1.)$$

Here, the Arrhenius-type constants *b*, *E* and *n*, as well as the functional form of $\Sigma Y_{i,\delta}$ are unknowns. Combinations of values: $-2 < b\&n < 2$, and $0 < E < 10{,}000$ were correlated with the mole fraction term, $\Sigma Y_{i,\delta}$, to find the bet fitting combination of constants. The result is shown in Figure 39, and the source data is listed in Table 8. The erosion onset factor at the time of erosion decreases with increasing mole fraction of oxidizing species, which means that erosion began at lower wall temperatures and pressures when the mass fraction of oxidizing species was larger. The erosion mitigation potential of N_2O is also reflected in these results. When O_2 is used as the oxidizer, there is no N_2 product gas, but when N_2O is used, N_2 can make up upwards of 60% of the mass fraction. According to the plot in Figure 39, a higher temperature and pressure were achieved before erosion occurred in the N_2O tests, which can be explained by the reduced mass fraction of oxidizing species compared with the O_2 tests. The solid black line can be thought of as a rough indicator of the value that the erosion onset factor must have for erosion to take place, which decreases with increasing mass fraction of oxidizing species. Thus, the region beneath the line can be considered the "pre-erosion" region, which exists for relatively values of T_w, and he region above the line can be considered the "erosion" region. The region of the line acts as a threshold, where the onset of erosion is likely to take place.

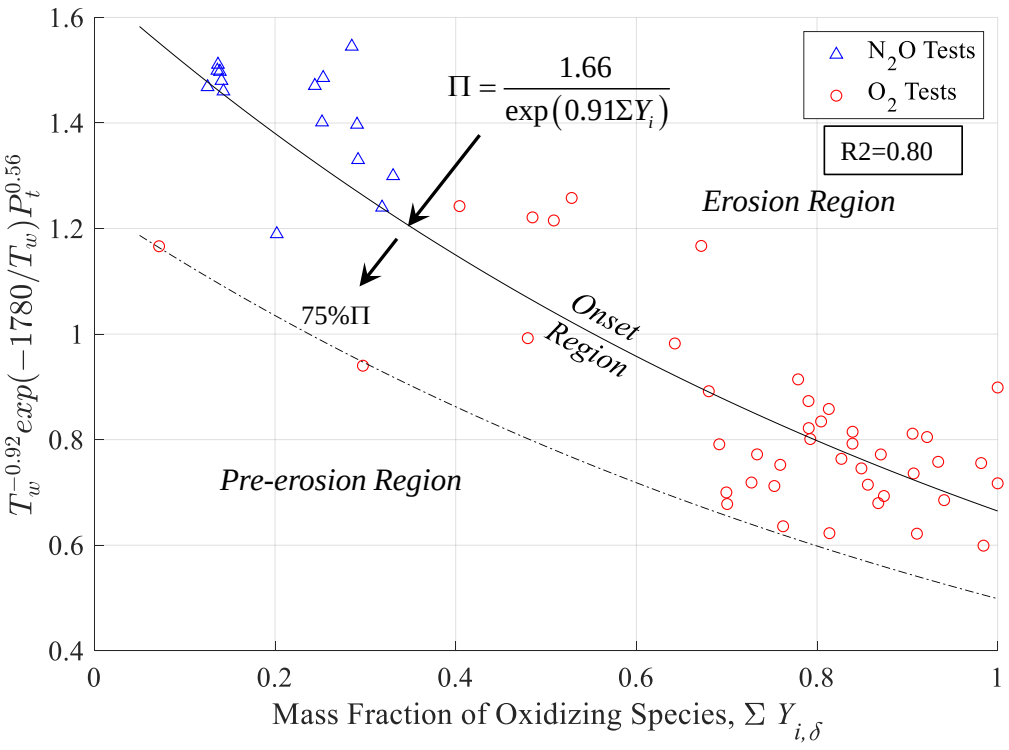

Figure 39. Erosion onset factor correlation.

According to this interpretation of the plot, for $\Sigma Y_{i,\delta} = 0.55$ (i.e. $\Pi = 1$) and $P_t = 3\times10^6$ Pa , erosion will occur when: $T_w^{-0.92} \exp(-1780/T_w) > 2.36\times10^{-4} \rightarrow T_w > 815$ K . However, if the value of pressure is lowered to $P_t = 1\times10^6$ Pa there is no value of T_w that satisfies the inequality: $T_w^{-0.92} \exp(-1780/T_w) > 4.37\times10^{-4} \rightarrow T_w$ DNE . This means that erosion will not occur when $\Sigma Y_{i,\delta} = 0.55$ and $P_t = 1\times10^6$ Pa , regardless of the value of T_w, so long as $\Pi = 1$ is the onset erosion threshold. When N_2O is used as the oxidizer, the mass fraction of oxidizing species cannot exceed $\Sigma Y_{i,\delta} \approx 0.4$ (see Figure 8), thus nozzle erosion will never occur in tests using N_2O as oxidizer when the pressure is 1 MPa. If we assume some

uncertainty in the threshold, and select a value of Π = 0.85 (i.e. 85%), nozzle erosion is predicted to occur when T_w = 1625 K: $T_w^{-0.92}\exp\left(-1780/T_w\right) > 3.71\times10^{-4} \rightarrow T_w$ >1625 K. The most compelling evidence in support of this interpretation of the results of Figure 39 would be the prevention of nozzle erosion through external cooling at the nozzle, forcing the erosion onset factor to remain below the solid line for a long duration firing test. However, as was seen in the review of results from CBX tests in Section 5.1.1, the leveling-off of erosion rate during a test in response to the decrease in pressure also supports the findings of Figure 39. In test CBX-7, nozzle erosion appears to wane at the following conditions: $P_t = 2\times10^6$ Pa, $T_w = 2000$ K, and $\Phi = 1.4$. From Figure 8(a) we can see that $\Phi = 1.4$ corresponds to $\Sigma Y_i \approx 0.25$, thus the erosion onset threshold inequality becomes:

$$\left(2000\right)^{-0.92}\exp\left(-1780/2000\right)\left(2\times10^6\right)^{0.56} = 1.27 \quad < \quad \Pi = 1.66/\exp\left(0.91\times0.25\right) = 1.32$$

Thus, the decrease in P_t in CBX-7 due to nozzle erosion can explain the end of nozzle erosion according to the erosion onset factor correlation. The main limitation of the nozzle erosion onset factor concept is that the rate of nozzle erosion upon onset is not postulated.

CHAPTER 6. IMPACT ON HYBRID ROCKET DEVELOPMENT

The main objectives of this research are to fill in knowledge gaps in chemical erosion theory, for which purpose the hybrid rocket motors were a useful tool. However, the use of hybrid rocket motors as a test apparatus comes with the consequence that a large range of combustion gas compositions tested in this study are only relevant to hybrid rocket motors. Furthermore, as discussed in Section 1.1.4, hybrid rocket engineers have the unique opportunity to combine cooling systems and technologies that traditionally could only be used in either liquid rockets OR solid rockets. Until now, there was no basis to include this kind of analysis into rocket development, because there was no data available to make an assessment of erosion, whether or not its onset can be postponed or prevented, and whether the selection of a low I_{sp} oxidizer, such as N_2O, outweighs the cost of using O_2, a high I_{sp} oxidizer that results from the increased nozzle erosion. Lastly, the data reduction method developed for and employed throughout this research is easily adaptable to hybrid rocket tests apparatus in general. In fact, of the numerous hybrid rocket research and development projects currently underway, there is a large possibility that all the data necessary for the type of analysis conducted in this study is readily available in the servers and hard drives of other researchers and simply not being taken advantage of. Thus, it is quite possible that widespread use of this data reduction and analysis would produce a vast repository of erosion data for various nozzle materials and operating conditions. These topics will be addressed in this chapter, with concluding remarks for future hybrid rocket development. First, the current state-of-the-art of hybrid rockets will be introduced to provide context to the discussion of the impact of this study in practice.

6.1 The State-of-the-Art of Hybrid Rockets

Hybrid rockets are currently the focus of countless aerospace propulsion projects worldwide. The most prominent example is Virgin Galactic Ltd.'s hybrid rocket-powered spaceplane, "SpaceShipTwo", which is projected to begin commercial operations this year (FY2019) [62]. The attention on hybrid rocket development is justified by the logistical cost savings and risk reduction during operations of hybrid rockets compared to their liquid bi-propellant and solid rocket counterparts [63][15]. There are two applications of hybrid rocket motors that currently dominate the field. The first is the use for the current state-of-the-art hybrid rockets is as apogee kick motors, the second is as the motor of Earth launch vehicles. The apogee kick motor application will give satellite operators a way to piggy-back on larger satellite buses to reach beyond conventional Earth-based orbits. Giving piggy-backed satellite operators a means of making orbital transfers independent of the primary satellite bus will increase launch opportunities, reducing wait times, and increasing freedom of movement to desired orbital placements. This is particularly attractive for the world's space agencies, which are looking for affordable ways to conduct deep space science and exploration missions.

6.1.1 Hybrid Rockets as Earth Launch Vehicles

One potential use for hybrid rockets is as small (Earth) launch vehicles, particularly for the delivery of small payloads to LEO. Numerous hybrid rocket development projects have reported their successes in recent years. These include the aforementioned SpaceShipTwo, as well as its predecessor vehicle, SpaceShipOne [64], the highly successful Stuttgart University student-based hybrid sounding rocket, HEROS 3, reported by Kobald et al. [65][66], the small launch vehicles of TiSPACE Inc. reported by Chen and Wu [67], the Peregrine sounding rocket project of NASA, Stanford University, and SPG

Inc. reported by Zilliac et al. [68], as well as the sounding rockets of Space Forest Ltd. reported by Gamal et al. [69].

In all these cases, N_2O is being, or has been, used as an oxidizer. Granted that the mini-launcher/sounding rocket spinoff of the HEROS3, named "HYPLOX75," by the company HyImpulse is now reportedly using LOX as the oxidizer in place of N_2O for the improvement in I_{sp} [70]. Although N_2O has some advantages over LOX because it is self-pressuring and can be stored and supplied at room temperature, the I_{sp} is nearly 10% lower. Based on the results of this study, it is clear that the superior I_{sp} of LOX will be harder to protect from nozzle erosion than that of N_2O, because erosion will begin at lower temperatures and pressures when using LOX than when using N_2O, and erosion rate is expected to be roughly twice as high. The only redeeming quality of LOX in the context of nozzle erosion prevention and mitigation is that it is cryogenic, and thus a potentially superior coolant for regenerative cooling.

The one attribute that is arguably most important for the success of an orbital launch vehicle is a high-thrust-to-weight ratio. This was the main challenge facing hybrid rocket developers until the dawn of the 21st century when two main strategies evolved towards improving thrust-to-weight ratios: through the use of innovative fuel grain designs; and through the use of fast-burning fuels. The former strategy was applied to SpaceShipOne/Two, and the hybrid rockets reported by Chen and Wu [67]. The latter strategy was applied to the hybrid rockets reported by Kobald et al. [65][66][70], Gamal et al. [69], and Zilliac et al. [68]. In the 5 kN thrust-class sounding rocket launch reported by Nagata et al., the former strategy was employed with great success using a high-density polyethylene (HDPE) fuel of the Cascaded Multistage Impinging-jet (CAMUI) design and liquid oxygen as the oxidizer [71], with an η^* of 99%, and a sustained acceleration during launch of 4 G to 5 G. This flight test was the predecessor to the 15kN-thrust class CAMUI rocket campaign that encountered the issue of excessive nozzle erosion and triggered the

current study. Interestingly, nozzle erosion does not lead to a large decrease in thrust in hybrid rockets, because the propellant mass flow rates do not depend on chamber pressure. This can be considered one strength of hybrid rockets compared with solid rockets. Even though the erosion rate may be higher in a hybrid rocket, the loss in performance will not be as great as in a comparable solid rocket. Nonetheless, the degree of nozzle erosion observed in the 15kN-thrust class CAMUI campaign was so severe that on two occasions the nozzles failed structurally and broke apart. This type of structural damage was also observed in the course of the current study, as is evident in the photographs of the ERM-9 nozzle in APPENDIX C. In ERM-9, the upper section of the nozzle separated from the lower half in a clean split. This was likely a combination of thermal stress and physical stress by the gas pressure at the throat. In CBX-16, are large longitudinal crack formed along the plane of the pressure measurement port. Thus, mitigation of nozzle erosion in hybrid rockets being used as Earth launch vehicles is largely a structural management problem, as well as a strategy to maintain optimal I_{sp}.

6.1.2 Hybrid Rockets as Apogee Kick Motors

The attribute of high thrust-to-weight ratio can be problematic in the application of hybrid rocket motors as apogee kick vehicles. For example, a piggy-back mission to GTO using the HII-A rocket operated by Mitsubishi Heavy Industries and the Japan Aerospace Exploration Agency (JAXA) rarely exceed an acceleration of 3 G [74]. Any acceleration beyond 3 G results in the overdesign of the satellite to withstand the forces that will result from the apogee kick. As an example, a transfer from GTO to Lunar orbit requires a change in velocity of roughly 800 m/s. Even at a constant acceleration of only 1 G, this apogee kick would require only a 90 s burn time. Kuo and Chiaverini summarize the advantages of hybrid rockets for upper-stage use, which includes the apogee kick concept, as having high specific impulse, throttling capability, safe manufacturing, and low cost [16](p. 632). Jens et al. reported extensively on the concept of a hybrid rocket-powered apogee kick

motor for placing CubeSats into deep space [75][76][77], selected the non-liquefying fuel, polymethyl methacrylate (PMMA), over a liquefying wax fuel for their hybrid rocket apogee kick motor development specifically to prevent acceleration from exceeding 3 G [77]. In short, achieving a high specific impulse, low manufacturing costs, and minimal combustion oscillations is more important than improving the fuel regression rate of a hybrid rocket being applied as an apogee kick motor. Therefore, the main benefit of mitigating nozzle erosion in hybrid rocket motors being used as satellite thrusters is that of preserving optimal I_{sp}.

6.1.3 Equivalence Ratio Shift and Its Mitigation

One major drawback inherent to most hybrid rockets is a shift in equivalence ratio during firing due to the transient nature of the burning surface area, fuel regression rate dependency on local mass flux, and the pressure feedback of oxidizer supply to the motor [78]. Nozzle erosion exacerbates this problem by reducing the chamber pressure, lowering the residence time of gas in the motor and altering the flow field. The result can be an accelerating equivalence ratio shift as seen in the MSS series tests of this study (refer to Figure 29). The Axial-Injection End-Burning (AIEB) hybrid rocket motor demonstrators reported by Saito et al. [79], and Hitt et al. [80], offer the possibility of eliminating equivalence ratio shifts, and/or throttling to maintain an optimal mixture ratio during firing through an innovative fuel grain design and oxidizer injection method. Although these projects are in the initial phases of development, the prospect of a fixed I_{sp} hybrid rocket is very attractive for both the launch vehicle and apogee kick applications mentioned above. One of the largest threats to the successful operation of AIEB hybrid rockets may be nozzle erosion. Based on the analysis presented in Section 1.2 of this thesis, nozzle erosion is especially problematic for the AIEB hybrid rocket.

6.2 Mitigation of Nozzle Erosion in Hybrid Rockets

The prediction and mitigation of nozzle erosion is important in the context of the development projects introduced in the previous section. Aside from the potential structural failure of a nozzle due to excessive nozzle erosion, the two main penalties of nozzle erosion are the loss in I_{sp}, and sharp decrease in P_c. The reduction in I_{sp} means that the propellant mass needed to accomplish a given mission will increase, and the reduction in P_c means that the motor will be overdesigned and heavier than it would otherwise need to be. For example, Kamps et al. recently reported the results of a feasibility study which showed that a CubeSat-size AIEB-type hybrid rocket apogee kick motor may lose up to 20% of its payload mass capability as a result of nozzle throat erosion [81]. Figure 5 showed that even in the case of miniscule nozzle throat erosion (0.05 mm/s), the I_{sp} of an AIEB-type hybrid rocket motor will be halved over a 100 s burn.

For hybrid rockets that use liquid oxidizers, the most practical and efficient nozzle erosion mitigation method may be a new type of regenerative cooling. Although the magnitude of nozzle erosion mitigation predicted by the Functional and modified Arrhenius formulas of Section 5.4 do not agree completely, there is a general agreement that nozzle erosion can be greatly reduced by keeping the nozzle wall temperature below 2000 K, and that nozzle erosion becomes diffusion-limited for temperatures greater than 2500 K. The concept of a combined regenerative/ablative cooling method that was briefly proposed in Section 1.3 (see Figure 3), will be elaborated further here.

A depiction of the conventional regenerative cooling system and new combined regenerative cooling/ablative system is shown in Figure 40. For a given convective mass

transfer coefficient, which is generally fixed by the scale and operating conditions of a given chemical rocket motor, the heat flux to the nozzle throat is proportional to the temperature difference between the nozzle throat wall and the combustion gas. In a conventional regenerative cooling system, the nozzle wall is a high-conductivity metal interface, such as copper, which must be maintained at a temperature of less than 900 K to prevent mechanical failure. However, if a graphite nozzle insert is placed between the metal interface and combustion gas, the temperature of the nozzle wall can be increased to without the risk of mechanical failure. Of course, one aim of this study is to find out how to predict the erosion rate that will result from this temperature increase. Based on the results of this study, it is now possible to quantify the tradeoff that will exist between these thermal management systems.

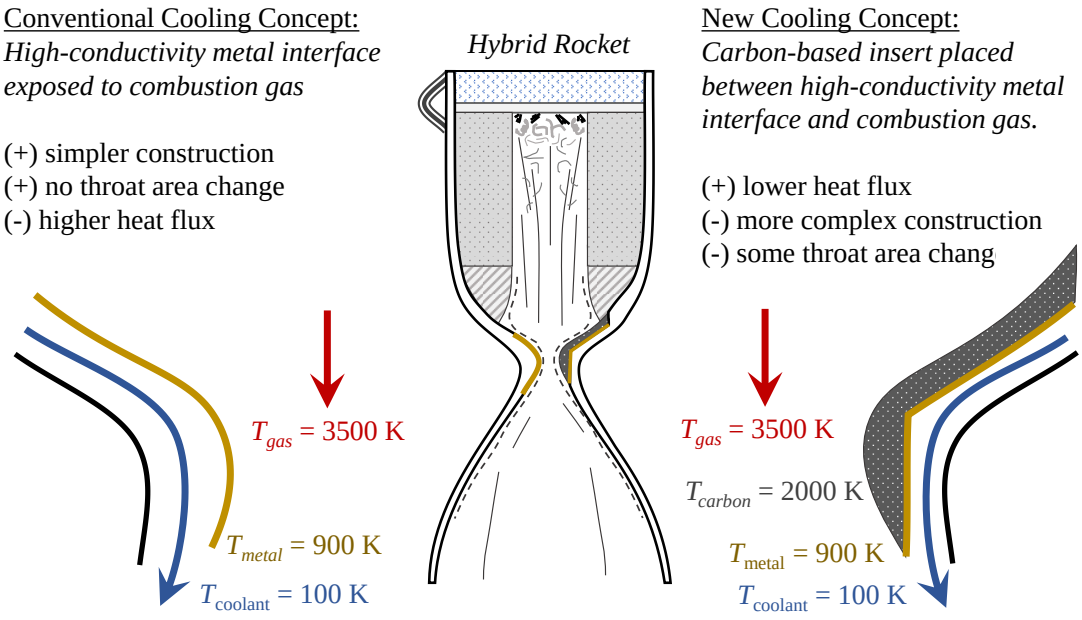

Figure 40. Combined regenerative cooling/ablative thermal management system.

For the simplified problem shown in Figure 40, the reduction in the cooling requirement at the nozzle is 42%:

$$1-\frac{q_{combined}}{q_{regenerative}}=1-\frac{h\left(3500-2000\right)}{h\left(3500-900\right)}=42\%$$

This may or may not be worth the increased complexity of nozzle construction, the point is that the erosion rate that will result at 2000 K can be calculated for the given firing conditions, and/or incorporated into a design algorithm to weigh the tradeoffs quantitatively.

CONCLUDING REMARKS

As hybrid rockets continue to increase in scale and performance, and capture the attention of the commercial sector as a safe and low-cost propulsion system, performance related issues such as nozzle erosion will become even more relevant. Until recently, there have been no detailed reports on the topic nozzle erosion characteristics specific to hybrid rockets, nor issues related to the direct comparison of hybrid rocket burning rates in motors with complex grain geometries or complex flow patterns. This study is one of the first of its kind. It draws from a rich background in ballistic reconstruction techniques to devise a "Comprehensive Data Reduction" procedure capable of solving for equivalence ratio, nozzle wall temperature and nozzle throat diameter history using experimental data typically measured in hybrid rocket static firing tests.

The results of Comprehensive Data Reduction are shown to agree well with initial nozzle throat diameter in numerous experiments of varying pressure, oxidizer flowrate and scale, while exhibiting acceptable experimental uncertainty. Although there appears to be some inconsistency in the experimental procedures or apparatus due to the large time span over which tests were conducted, the overall trend in the data clearly shows that empirical formulas for erosion rate adequately predict the timing at the onset of erosion and subsequent rate of erosion. Widespread use of the Comprehensive Data Reduction method by other researchers would quickly fill a void of experimental nozzle erosion data. Due to the large variety of materials, motor designs etc. there are several modifications that may be necessary to the basic empirical formulas introduced in this study. However, the only

way to develop such modifications is to build a larger body of data from experimental firing tests.

Now, there is no doubt that nozzle erosion begins at a time that correlates to basic thermodynamic properties of the combustion gas flow in the rocket, predominately pressure, temperature and concentration of oxidizing (gas) species. Tests such as DNT-16 thru -18 and MSS-2 and -3, prove that erosion can be mitigated for extended periods of time by operating in fuel rich conditions, at low Reynold's numbers and low pressures. Tests such as CBX-11 thru -16 show that operating in oxidizer rich conditions at high pressures can be detrimental, even in combustion gas containing a large mass fraction of inert gas – N_2 in the case of the CBX series tests. A new term has been introduced as the "erosion onset factor" to quantify the conditions that correlate with the onset of erosion, i.e. wall temperature, pressure and mass fraction of oxidizing species. It appears that this term may be used for the determination of the nozzle temperature and pressure that will prevent nozzle erosion form occurring. Based on these findings, an alternative thermal management system for hybrid rockets has been proposed which combines regenerative and ablative cooling. Until now, there was no way criteria to judge the cost-effectiveness of such a system. It is also expected that the incorporation of the (thermally) chemical-kinetic-limited regime of nozzle erosion into the empirical formulas will increase the accuracy and predictability of performance estimations of chemical rockets employing carbon-based nozzles. The potential applications of the findings in this study are far reaching, and it is with great enthusiasm that I conclude this first body of work.

APPENDIX A. TABLES OF FIRING TEST RESULTS

Table 6. Description of test campaign.

Series	Timeframe	Objective(s)	Strategy
Trigger Event: Excessive erosion in 15kN-thrust class CAMUI rockets (2014-15)			
ERM 9 x success 1 x failure	May 2015 thru Feb. 2016	Investigate dependency of nozzle erosion on equivalence ratio.	Use 2kN-thrust class CAMUI-type motors. Correlate time-averaged data.
HK 7 x success 7 x failure	June 2016 thru Oct. 2016	Develop method for determining nozzle throat erosion and equivalence ratio histories. Evaluate erosion dependency on equivalence ratio	Use conventional (tubular) fuel to simplify test design and reduce equivalence ratio shift during firing. Modify previous reconstruction techniques.
DNT 16 x success 5 x failure	Oct. 2016 thru July 2017	Investigate accuracy and repeatability of the NTRT. Observe progression of nozzle erosion in time. Create adjustable motor.	Repeat tests, prolonging time of shutdown, and confirm the results of the NTRT do not vary in time. Implement LEGO-like fuel blocks for fuel design.
SLY 6 x success 1 x failure	Oct. 2016 thru Feb. 2017	Observe erosion in fuel rich and very oxidizer rich conditions. Eliminate LF oscillations.	Mix and match fuel blocks to improve mixing, increase and/or reduce fuel consumption, and eliminate acoustic coupling.
MSS 8 x success 2 x failures	Dec. 2017 thru Aug. 2018	Investigate accuracy and repeatability of the NTRT+ for fuel rich O2 tests. Observe progression of nozzle erosion in time at a larger scale.	Mimic DNT series test procedure at a larger scale, using CAMUI-type motor to improve combustion efficiency.
QE 4 x success 1 x failure	May 2018 thru June 2018	Examine the conditions at the onset of erosion. Examine effect of erosion on heat transfer rate	Conduct short duration firing tests, increasing oxidizer mass flow rate between tests to identify the conditions at the onset of erosion.
CBX 14 x success 2 x failures	March 2018 thru Dec. 2018	Investigate accuracy of the NTRT+ for N2O tests. Observe progression of nozzle erosion in time. Evaluate erosion reduction through oxidizer selection	Mimic DNT series test procedure using liquid N_2O as oxidizer in place of GOX.

Table 7. Summary of direct measurements*.

Test	t_b	$d_{t,o}$	$d_{t,f}$	Δm_{fu}	$\bar{\dot{m}}_{ox}$	$\bar{P}_c$	$\bar{F}$	$\bar{T}_{n,1}$	$\bar{T}_{n,2}$	$\bar{T}_{n,3}$
	s	mm	mm	g	g/s	MPa	N	K	K	K
GOX Firing Tests (Conducted Using Hokkaido University Facilities)										
DNT-2	20	4.0	6.5	72	12	1.2	26	>1295	1190	
DNT-3	15	4.0	5.0	52	11	1.4	26	>1133	1030	
DNT-4	25	4.0	6.3	79	11	1.0	24	>1352	>1190	1109
DNT-6	10	4.0	4.4	33	12	1.5	25	970	765	715
DNT-11	17	4.0	5.3	63	11	1.4	25	>1290	984	907
DNT-12	15	4.0	4.3	41	9	1.2	20	946		709
DNT-13	17	4.0	5.3	52	9	1.1	20	>1230	926	896
DNT-14	12	4.0	4.6	34	8	1.1	19	>1112	804	758
DNT-15	5	4.0	4.0	12	8	1.0	17	592	555	528
DNT-16	10	4.0	4.1	26	8	1.2	18	837	754	705
DNT-17	15	4.0	4.2	41	8	1.1	20	1068	843	798
DNT-18	20	4.0	4.2	61	8	1.2	21	1071	860	780
DNT-19	5	4.0	4.4	14	11	1.4	19	751	543	529
DNT-20	5	4.0	4.1	15	12	1.5	19	716	560	527
DNT-21	10	4.0	5.1	31	12	1.3	25	1103	775	769
HK-8	20	4.0	4.9	71	13	1.5	27	1099	1067	981
HK-9	20	4.0	5.3	70	14	1.4	27	>1207	>1141	
HK-10	20	4.0	4.3	60	11	1.3	20	1090	893	810
HK-11	20	4.0	5.6	89	14	1.5	29	>1282	1146	1116
HK-12	20	4.0	5.9	95	14	1.3	33	>1269	>1141	1080
HK-13	20	4.0	5.3	61	12	0.9	23	>1226	1076	987
HK-14	20	4.0	5.4	72	13	1.1	27	>1204	>1189	1114
SLY-1	20	4.0	5.0	70	10	1.2	24	>1259	977	926
SLY-2	20	4.0	5.1	64	10	1.1	20	1116	941	870
SLY-3	20	4.0	4.8	41	12	0.9	15	1178	883	817
SLY-5	20	4.0	5.3	57	12	1.2	22	1171	967	953
SLY-6	20	4.0	6.6	56	11	1.0	23	>1347	1133	1056
SLY-7	20	4.0	5.6	59	11	1.1	23	>1200	1116	1060
QE-3	5	4.0	4.1	14	11	1.4	24	706	584	540
QE-4	5	4.0	4.1	16	13	1.6	29	756	553	535
QE-5	5	4.0	5.0	18	15	1.6	34	833	588	578
Liquid N_2O Firing Tests (Conducted Using Hokkaido University Facilities)										
CBX-2	10	4.0	4.8	44	27	2.9	58	1186	965	931
CBX-3	5	4.0	4.2	41	39	4.2	79	809	643	583
CBX-4	4	4.0	4.2	35	41	4.1	78	741	588	534
CBX-5	4	4.0	4.1	30	41	4.1	74	661	551	519
CBX-6	10	4.0	4.6	74	39	4.2	81	1110	1012	960
CBX-7	15	4.0	4.8	110	37	4.3	88	1171	1108	1019
CBX-8	10	4.0	4.8	73	38	4.4	89	1003	896	823
CBX-9	10	4.0	5.0	74	39	4.1	83	1121	902	869
CBX-10	10	4.0	6.2	55	44	3.4	95	1174	975	835
CBX-11	15	4.0	7.5	78	47	2.9	96	848	1145	1098

CBX-12	5	4.0	5.0	28	42	4.0	83	748	684	614
CBX-13	5	4.0	5.4	23	46	4.0	86	906	790	647
CBX-14	10	4.0	6.7	51	46	3.4	95	1188	1053	866
CBX-16	15	4.0	7.7	63	48	2.8	96	1256	1217	1101
LOX Firing Tests (Conducted Using Uematsu Electric Company Facilities)										
ERM-2	5	27.0	27.6	1155	415	2.0	1489	630	517	-
ERM-3	5	27.0	27.4	999	554	2.1	1556	607	406	-
ERM-4	5	27.0	28.3	785	565	2.0	1523	606	525	-
ERM-5	5	27.0	28.1	314	628	1.3	924	570	515	-
ERM-6	5	27.0	27.7	499	567	1.6	1183	611	>454	-
ERM-8	5	23.0	25.3	825	491	2.6	1492	679	540	-
ERM-10	10	23.0	24.0	477	310	1.3	721	827	671	-
MSS-2	4	23.6	23.6	1686	523	3.3	1925	502	366	321
MSS-3	7	23.6	24.4	2189	502	3.1	1923	673	448	367
MSS-4	13	23.6	27.4	3692	506	3.0	1937	929	588	454
MSS-5	19	23.6	30.9	4576	513	2.8	1880	1073	702	525
MSS-6	12	23.6	26.2	3543	504	3.1	1953	895	570	443
MSS-8	11	19.8	19.9	2434	324	2.7	1104	647	465	389
MSS-9	5	27.2	28.9	1955	627	2.9	2273	721	450	361
MSS-12	7	33.4	34.9	2450	729	2.2	2481	729	494	386

*Time-averages are taken for the entire burn time. Greater than symbols, >, mean that data was not available for the entire burn time.

Table 8. Summary of comprehensive data reduction results[*].

Test[**]	t_{on}	$\bar{\dot{r}}_t$	$\bar{\Phi}$	$\bar{P}_t$	$\bar{T}_w$	$\bar{\rho}_w$	$\bar{D}_w$	$\bar{\delta}$	$P_{t,on}$	$T_{w,on}$	$\Sigma Y_{i,\delta,on}$	η^*
	s	mm/s		Pa	K	kg/m^3	mm^2/s	μm	Pa	K		
GOX Firing Tests (Conducted Using Hokkaido University Facilities)												
DNT-2	3	0.07	1.1	0.6	>1973	0.9	86	39	1.0	1737	0.78	0.82
DNT-3	5	0.05	1.1	0.8	>1814	1.3	56	29	0.9	1449	0.81	0.79
DNT-4	4	0.06	1.0	0.5	>2407	0.7	136	46	0.9	2288	0.79	0.78
DNT-6	3.5	0.03	1.1	0.9	2100	1.2	62	27	0.9	1737	0.80	0.82
DNT-11	4.5	0.05	1.1	0.8	>2710	0.8	114	34	1.0	2400	0.72	0.85
DNT-12	7	0.02	1.2	0.7	1852	1.1	62	30	0.7	1636	0.72	0.80
DNT-13	4	0.05	1.2	0.6	>2565	0.7	131	40	0.8	1858	0.75	0.82
DNT-14	3	0.03	1.2	0.7	>2480	0.8	114	36	0.7	1786	0.73	0.81
DNT-15	-	-	-	-	-	-	-	-	-	-	-	0.72
DNT-16	6	0.01	1.2	0.7	1620	1.2	52	31	0.7	1507	0.69	0.77
DNT-17	3	0.01	1.2	0.7	2066	0.9	79	33	0.7	1405	0.75	0.78
DNT-18	7	0.01	1.4	0.7	2199	0.9	82	31	0.7	1764	0.70	0.79
DNT-19	2.5	0.09	1.0	0.9	2064	1.3	63	28	0.9	1821	0.82	0.79
DNT-20	1.5	0.01	1.0	0.9	1564	1.8	36	24	0.9	1399	0.84	0.80
DNT-21	3	0.08	1.0	0.7	2497	0.9	105	35	0.9	1890	0.82	0.81
HK-8	3	0.03	1.0	0.9	1490	1.7	36	25	0.9	1332	0.92	0.79
HK-9	3	0.04	0.90	0.8	>1577	1.6	44	28	0.9	1423	0.92	0.75
HK-10	3	0.01	1.0	0.7	1978	1.2	67	30	0.8	1393	0.85	0.75
HK-11	3	0.05	1.2	0.8	>2194	1.1	74	30	1.1	2064	0.77	0.79
HK-12	2	0.05	1.2	0.7	>1928	1.1	70	33	1.0	1620	0.79	0.68
HK-13	2	0.04	0.9	0.5	>1978	0.8	102	43	0.6	1500	0.90	0.58
HK-14	3	0.04	1.0	0.6	>2161	0.8	97	38	0.8	1755	0.84	0.62
SLY-1	2.5	0.03	1.3	0.7	>2376	0.8	99	34	0.8	1915	0.73	0.76
SLY-2	2	0.03	1.2	0.7	1827	1.1	69	33	0.8	1218	0.78	0.81
SLY-3	2.5	0.02	0.6	0.5	2217	0.8	119	42	0.6	1489	0.98	0.64
SLY-5	4.5	0.04	0.9	0.6	2019	1.1	85	36	0.8	1332	0.91	0.75
SLY-6	2	0.07	0.9	0.6	>2569	0.7	151	46	0.9	1963	0.91	0.85
SLY-7	3.5	0.05	0.9	0.6	>2139	0.9	93	37	0.8	1806	0.86	0.79
QE-3	2	0.02	1.0	0.9	1600	1.7	40	25	0.9	1423	0.83	0.78
QE-4	3	0.03	1.0	1.0	2047	1.4	53	25	1.0	1964	0.81	0.75
QE-5	1.5	0.15	0.9	0.9	2019	1.5	57	26	1.1	1487	0.88	0.77
Liquid N_2O Firing Tests (Conducted Using Hokkaido University Facilities)												
CBX-2$^+$	2.5	0.05	1.7	1.6	>2678	1.8	51	15	1.8	2407	0.20	0.87
CBX-3$^+$	2.5	0.04	2.2	2.6	2150	3.2	22	8	2.6	2064	0.12	0.77
CBX-4$^+$	2.5	0.07	2.0	2.6	2128	3.4	21	9	2.6	2005	0.14	0.72
CBX-5$^+$	-	-	-	-	-	-	-	-	-	-	-	0.69
CBX-6$^+$	2.5	0.04	1.8	2.4	>2024	3.4	21	10	2.6	1916	0.14	0.84
CBX-7$^+$	3.5	0.04	1.8	2.4	>1856	3.7	18	10	2.7	1854	0.14	0.89
CBX-8$^+$	3.5	0.04	1.8	2.5	>1893	3.8	18	9	2.7	1761	0.14	0.80
CBX-9$^+$	3	0.07	1.7	2.4	2211	3.1	25	10	2.7	2133	0.14	0.82
CBX-10	2.5	0.14	1.1	1.9	>2414	2.5	38	15	2.5	2083	0.27	0.82
CBX-11	2	0.14	1.1	1.6	2279	2.3	43	18	2.7	1784	0.26	0.81
CBX-12	2	0.16	1.3	2.6	2255	3.5	24	11	2.7	2003	0.25	0.78
CBX-13	1.5	0.20	1.1	2.5	2158	3.9	23	11	2.8	1655	0.30	0.80
CBX-14	2	0.17	1.0	2.0	>2615	2.5	44	15	2.8	2318	0.29	0.85
CBX-16	2	0.14	0.9	1.5	>1881	2.8	34	18	2.8	1352	0.30	0.85
LOX Firing Tests (Conducted Using Uematsu Electric Company Facilities)												
ERM-2	2.5	0.13	1.9	1.2	1982	1.4	42	24	1.2	1774	0.32	1.04
ERM-3	3	0.12	1.0	1.2	2413	1.5	58	30	1.2	2271	0.72	0.93
ERM-4	2	0.24	0.9	1.1	1818	2	40	29	1.2	1367	0.76	0.95
ERM-5	2.5	0.22	0.3	0.8	1619	1.7	47	33	0.8	1619	1	0.84

ERM-6	-	-	-	-	-	-	-	-	-	-	-	0.90
ERM-8	2	0.41	1.1	1.6	2253	2.1	39	23	1.7	2174	0.70	1.04
ERM-10	4	0.09	0.5	0.8	2149	1.2	75	39	0.8	2117	0.98	1.04
MSS-2^{+}	-	-	-	-	-	-	-	-	-	-	-	1.02
MSS-3^{+}	5	0.19	1.6	1.9	1993	2.4	26	18	1.9	1993	0.43	1.06
MSS-4^{+}	6.5	0.28	1.4	1.7	2260	2	37	22	1.8	2025	0.51	1.06
MSS-5^{+}	7.5	0.32	1.2	1.5	2589	1.7	55	26	1.8	2177	0.54	1.07
MSS-6^{+}	7	0.24	1.3	1.8	2288	2.2	34	20	1.9	2118	0.55	1.09
MSS-8	-	-	-	-	-	-	-	-	-	-	-	0.97
MSS-9	3	0.36	2.3	1.7	2311	1.5	39	15	1.7	2251	0.11	1.07
MSS-12	5	0.32	1.5	1.2	2285	1.4	52	29	1.3	2025	0.51	1.01

* Time-averages are taken for times after the onset of erosion. Greater than symbols, >, mean that data was not available for the entire burn time.

** The NTRT^{+} method was in tests with the superscript "+", all other tests the NTRT was used. Also, these tests shared the same thermocouple data from MSS-7 which is not included in this study

APPENDIX B. EXAMINATION OF CDR ASSUMPTIONS

The Comprehensive Data Reduction (CDR) method operates under two assumptions that may lead to uncertainties that cannot be quantified by the perturbation analysis method of Section 4.2. In all tests for which the NTRT was used (rather than the NTRT$^+$), the η^* is assumed to be constant. The DNT and MSS series tests were conducted in a way where this assumption can be tested by comparing the results of CDR for each test. This confirmation is possible through inspection of the table and plot of the results of η^* as shown in Figure 41. Tests were grouped by control group, which accounts for the motor and initial test conditions. The independent variable in each group is the burn time, t_b [s]. Thus, the standard deviation of η^* serves as a quantitative assessment of the validity of the assumption that η^* is constant in time. Since the standard deviation is 3% or below in these tests, this data supports the assumption that η^* can be treated as a constant.

Test Group	Mean	Standard Deviation
MSS-2 MSS-3 MSS-6 MSS-4 MSS-5	1.06	0.02
DNT-15 DNT-16 DNT-17 DNT-18	0.80	0.02
QE-3 DNT-6 DNT-3 DNT-2 DNT-4	0.77	0.03

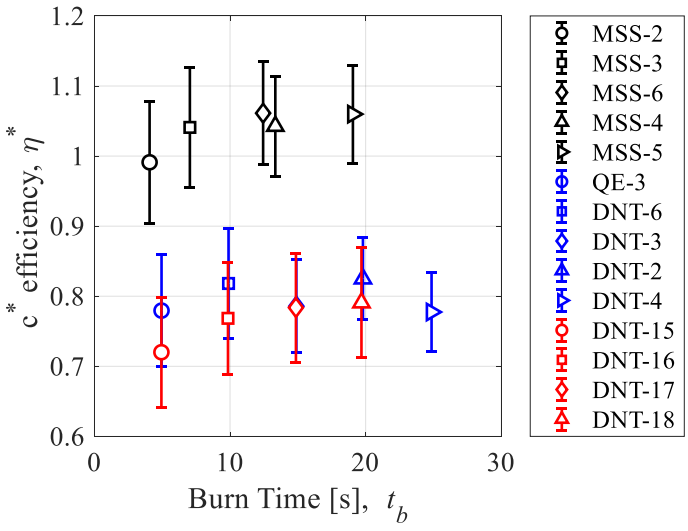

Figure 41. Verification of constant η^* assumption in DNT and MSS tests.

Furthermore, the CBX-3 thru -9 test results were determined using the NTRT+, which means that the histories of η^* are available. A review of these histories reinforces the assumption that η^* is relatively constant in time is valid, as shown in Figure 42. It is clear that after 3 s into the burn time, the values of η^* reach a steady state (and remain constant). This is true despite the fact that nozzle erosion is occurring at an average rate of just under 0.05 mm/s in these tests. Note that in the NTRT, the solution to η^* is determined by the final nozzle throat diameter only, and therefore represents the value of η^* at the end of the burn only. For this reason, the error due to a start-up transient does not appear in the results for η^*, but rather in the results for nozzle throat erosion history.

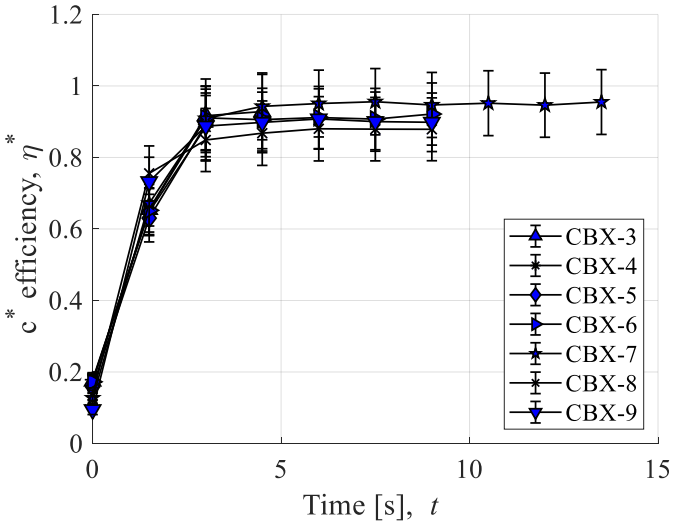

Figure 42. η^* reaches steady-state values in CBX tests.

The governing assumption of the TTRT is that heat transfer in the nozzle is one-dimensional in the radial direction. Since the nozzles in this study have sharp turns into the entrance region, it is necessary to examine this assumption quantitatively, and include a way to validate the assumption experimentally. First, Bartz's correlation [1] for convective

heat transfer coefficients can be used to estimate the convective heat mass flux profile in the axial flow direction between the nozzle entrance and exit. The results of this calculation are shown in Figure 43 for the two types of nozzle contours used in this study: sharp (90 deg) circular inlet used in all tests but MSS series tests; gradual conical inlet used in MSS series tests.

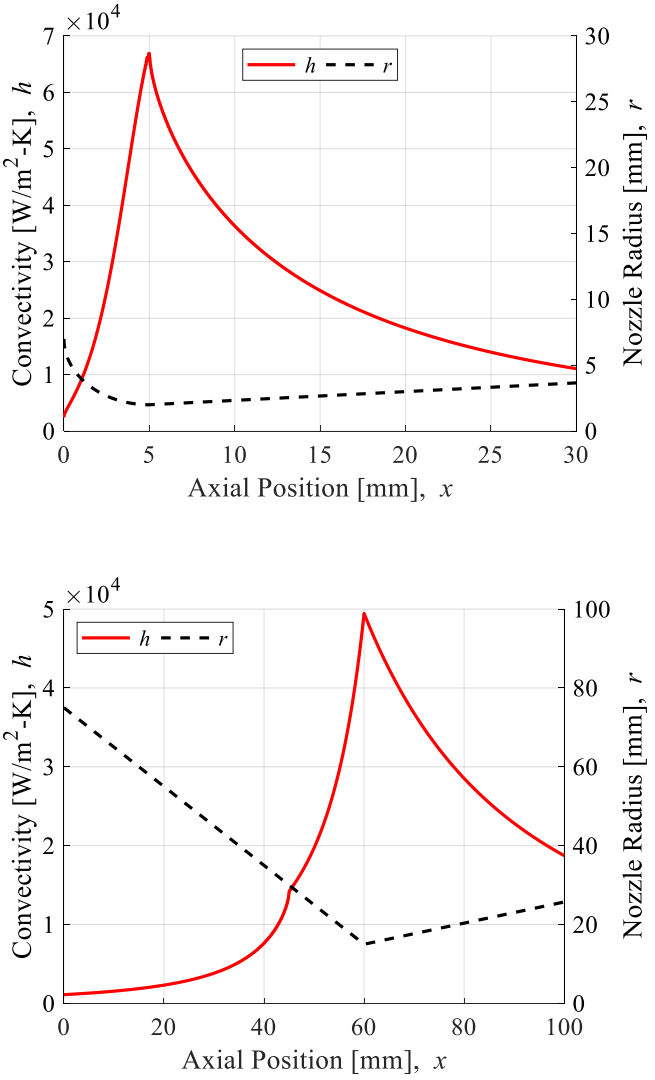

Figure 43. Sharp increase in heat transfer coefficient at the nozzle throat in: (upper) *sharp circular inlet;* (lower) *gradual conical inlet.* P_c = 3 MPa; Φ = 1; LOX/HDPE.

It is clear that when the nozzle radius, r [m], is smallest, i.e. at the throat, the heat transfer coefficient ("convectivity"), h [W/m^2-K], is between five and ten times larger than at the entrance of the nozzle. Furthermore, due to the circular rounding of the nozzle throat, as this sharp increase takes place, the surface vector approaches the radial direction. Thus, the approximation of radial heat transfer at the throat seems appropriate from the perspective of heat transfer coefficients. To verify this assumption, the use of a check thermocouple was implemented in tests whenever possible. The "check" thermocouple is placed at a depth between the two thermocouples used for the NTRT, and serves as a confirmation of the temperature at that position along the radial temperature profile. The use of a check thermocouple in MSS-5 is shown in Figure 44. The fact that the check thermocouple temperature matches the calculated temperature profiles at that position at all times during firing supports the assumption that heat transfer can be approximated as one-dimensional.

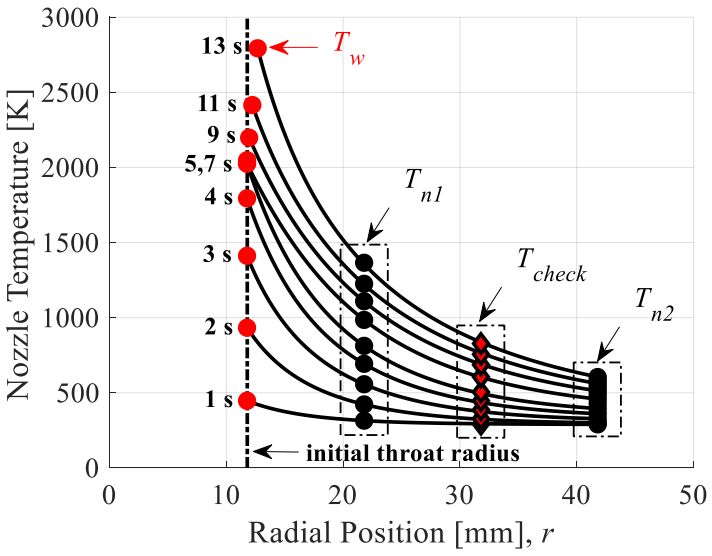

Figure 44. Check thermocouple supports TTRT results of MSS-5.

APPENDIX C. PHOTOGRAPHS OF NOZZLES POST-FIRING

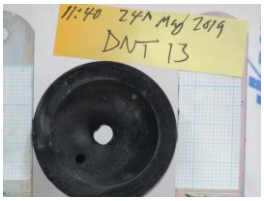

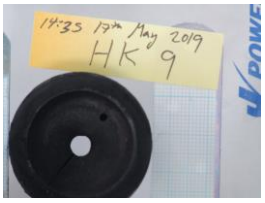

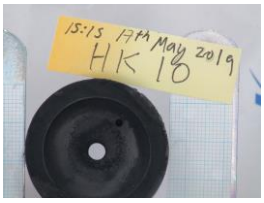

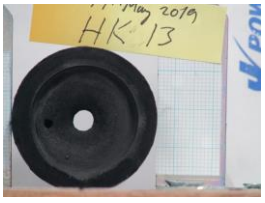

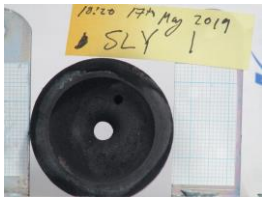


10:15 17th May 2019
SLY 3

09:50 17th May 2019
SLY 5
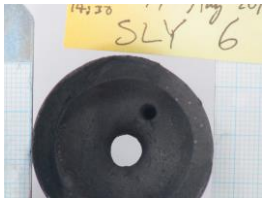
SLY 6
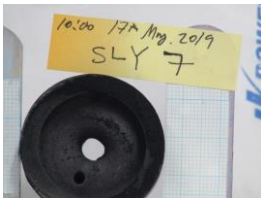
10:00 17th May 2019
SLY 7

15:30 17th May 2019
CBX 2

15:30 17th May 2019
CBX 3

15:35 17th May 2019
CBX 4

15:35 17th May 2019
CBX 5

15:40 17th May 2019
CBX 6

15:40 17th May 2019
CBX 7

CBX 8

15:45 17th May 2019
CBX 9
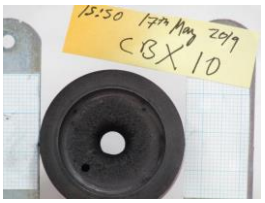
15:50 17th May 2019
CBX 10

CBX 11
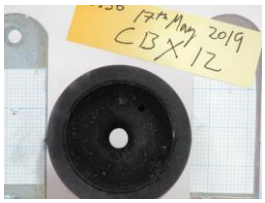
CBX 12
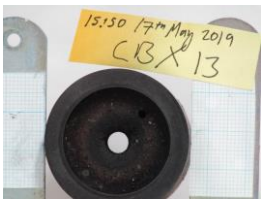
15:50 17th May 2019
CBX 13

CBX 14
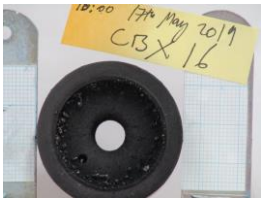
CBX 16


ERM 2
5th July 2019
ERM 2
ERM 2

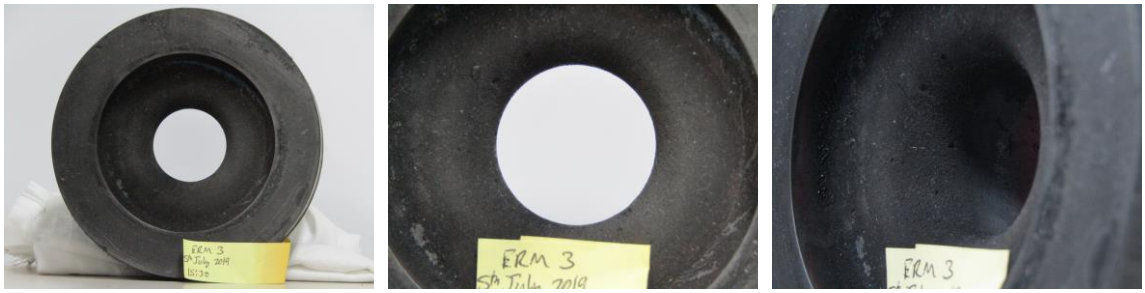
ERM 3
ERM 3
ERM 3

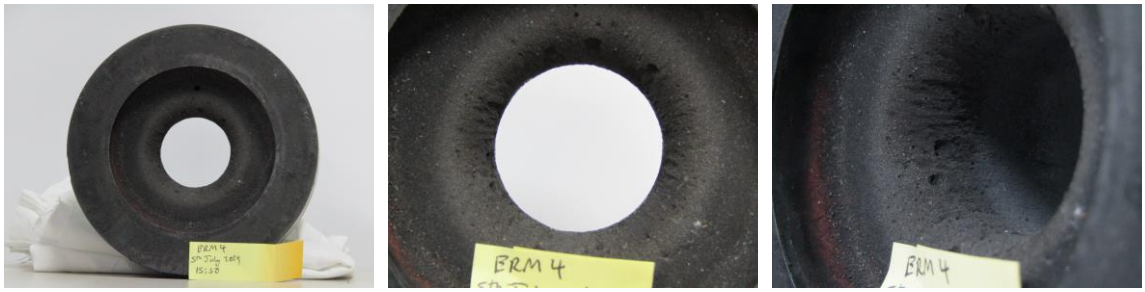
ERM 4
ERM 4
ERM 4


ERM5
ERM5
ERM5





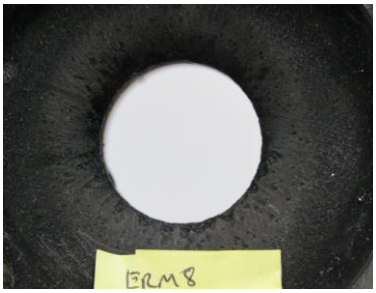


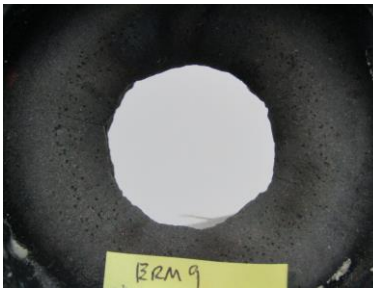



REFERENCES

[1] D. R. Bartz, “A Simple Equation for Rapid Estimation of Rocket Nozzle Convective Heat Transfer Coefficients,” *J. Jet Propuls.*, vol. 27, no. 1, pp. 49–51, 1957.

[2] D. R. Bartz, “Turbulent Boundary-Layer Heat Transfer from Rapidly Accelerating Flow of Rocket Combustion Gases and of Heated Air,” *Adv. Heat Transf.*, vol. 2, no. C, pp. 1–108, 1965.

[3] G. P. Sutton and O. Bibliarz, *Rocket Propulsion Elements*, 8th ed. John Wiley & Sons, Inc., 2010.

[4] H. G. Price, “Cooling of High-Pressure Rocket Thrust Chambers With Liquid Oxygen,” *J. Spacecr. Rockets*, vol. 18, no. 4, pp. 338–343, 1980.

[5] H. G. Price and P. A. Masters, “Liquid Oxygen Cooling of High Pressure LOX / Hydrocarbon Rocket Thrust Chambers,” 1986.

[6] E. Armstrong and J. Schlumberger, “Cooling of Rocket Thrust Chambers With Liquid Oxygen (NASA TM-103416),” 1990.

[7] S. Yuasa, K. Kitagawa, T. Sakurazawa, I. Kumazawa, and T. Sakurai, “Liquid Oxygen Vaporization Techniques for Swirling-Oxidizer-Flow-Type Hybrid Rocket Engines,” *Int. J. Energ. Mater. Chem. Propuls.*, vol. 10, no. 2, pp. 155–168, 2011.

[8] J. D. Batchelor and E. L. Olcott, “Failure Mechanisms in Dense Tungsten Alloy

Rocket Nozzles," *J. Spacecr. Rockets*, vol. 1, no. 6, pp. 635–642, 1964.

[9] J. R. Johnston, R. A. Signorelli, and J. C. Freche, "Performance of Rocket Nozzle Materials With Several Solid Propellants," Washington, D. C., 1966.

[10] W. D. Klopp, "Materials," in *Exploring in Aerospace Rocketry*, National Aeronautics and Space Administration, Washington, D.C., 1971, pp. 79–94.

[11] H. O. Pierson, *Handbook of Carbon, Graphite, Diamond and Fullerenes: Properties, Processing and Applications*. Park Ridge, New Jersey: Noyes Publications, 1993.

[12] R. L. Bailey and E. G. Parks, JR., "Evaluation of Concepts for Reuse of Large Booster Nozzles.," *J. Spacecr. Rockets*, vol. 5, no. 5, pp. 577–582, 1969.

[13] N. A. Kimmel, "Alternate Nozzle Ablative Materials Program (JPL Pub 84-58)," 1984.

[14] L. B. Powers and R. L. Bailey, "Shuttle Subscale Ablative Nozzle Tests," *J. Spacecr. Rockets*, vol. 19, no. 2, pp. 104–112, 1982.

[15] D. Altman, "Overview and History of Hybrid Rocket Propulsion," in *Fundamentals of Hybrid Rocket Combustion and Propulsion*, M. J. Chiaverini and K. K. Kuo, Eds. AIAA, 2007, pp. 1–36.

[16] K. K. Kuo and M. Chiaverini, "Challenges of Hybrid Rocket Propulsion in the 21st Century," in *Fundamentals of Hybrid Rocket Combustion and Propulsion*, M. J. Chiaverini and K. K. Kuo, Eds. AIAA, 2007, pp. 593–638.

[17] S. D. Eilers, S. Whitmore, and Z. Peterson, “Multiple Use Hybrid Rocket Motor,” US2014/0026537A1, 2014.

[18] N. Quigley and J. E. Lyne, “Development of a Three-Dimensional Printed, Liquid-Cooled Nozzle for a Hybrid Rocket Motor,” *J. Propuls. Power*, vol. 30, no. 6, pp. 1726–1727, 2014.

[19] P. Lemieux, “Nitrous Oxide Cooling in Hybrid Rocket Nozzles,” *Prog. Aerosp. Sci.*, vol. 46, no. 2–3, pp. 106–115, 2010.

[20] G. Ercole, E. Garofalo, P. Lemieux, M. M. Maglie, and D. Pastrone, “N2O-Cooled Aerospike for a Hybrid Rocket Motor: Nitrous Oxide Characterization and Additive Manufacturing,” in *53rd AIAA/SAE/ASEE Joint Propulsion Conference*, 2017, no. July, pp. 1–18.

[21] A. Kumar, V. Saini, P. R. Usurumarti, and R. S. Dondapati, “Feasibility Studies on the Cooling of Hybrid Rocket Nozzles Using Supercritical Nitrous Oxide,” *Energy Procedia*, vol. 109, pp. 338–345, 2017.

[22] D. Bianchi and F. Nasuti, “Numerical Analysis of Nozzle Material Thermochemical Erosion in Hybrid Rocket Engines,” *J. Propuls. Power*, vol. 29, no. 3, pp. 547–558, 2013.

[23] S. Gordon and B. J. McBride, “Computer Program for Calculation of Complex Chemical Equilibrium Compositions (NASA RP-1311),” 1994.

[24] L. Meyer, “The Surface Reaction of Graphite of Graphite With Oxygen Carbon

Dioxide and Water Vapour at Low Pressures," *Trans. Faraday Soc.*, vol. 34, no. 1056, pp. 1056–1061, 1938.

[25] R. F. Strickland-Constable, "The Oxidation of Carbon by Nitrous Oxide," *Trans. Faraday Soc.*, vol. 34, no. 1374, pp. 1374–1384, 1938.

[26] R. F. Strickland-Constable, "The Interaction Oxygen and Carbon Filaments at High Temperatures," *Trans. Faraday Soc.*, vol. 40, pp. 333–343, 1944.

[27] J. S. Binford and H. Erying, "Kinetics of the Steam-Carbon Reaction," *J. Phys. Chem.*, vol. 63, no. 5, pp. 693–696, 1959.

[28] L. J. Delaney, L. C. Eagleton, and W. H. Jones, "A Semiquantitative Prediction of the Erosion of Graphite Nozzle Inserts," *AIAA J.*, vol. 2, no. 8, pp. 1428–1433, 1964.

[29] A. J. McDonald and P. O. Hedman, "Erosion of Graphite in Solid-Propellant Combustion Gases and Effects on Heat-Transfer," *AIAA J.*, vol. 3, no. 7, pp. 1250–1257, 1965.

[30] J. L. Mayberry, J. W. Kordig, R. J. Zeamer, and S. C. Bro, "Correlation of Graphite Nozzle Throat Erosion in Solid-Rocket Motors.," *AIAA J.*, vol. 6, no. 11, pp. 2222–2224, 1968.

[31] S. R. Turns, *An Introduction to Combustion: Concepts and Applications*, 3rd ed. New York, NY: McGraw-Hill, 2012.

[32] S. T. Keswani, E. Andiroglu, J. D. Campbell, and K. K. Kuo, "Recession Behavior of Graphitic Nozzles in Simulated Rocket Motors," *J. Spacecr. Rockets*, vol. 22, no.

4, pp. 396–397, 1985.

[33] L. E. Jones, P. A. Thrower, and P. L. Walker, “Bulk Graphite Nozzle Recession-An analysis Based on the Carbon-Steam Reaction,” *Carbon N. Y.*, vol. 24, no. 1, pp. 43–49, 1986.

[34] V. Borie, J. Brulard, and G. Lengelle, “Aerothermochemical Analysis of Carbon-Carbon Nozzle Regression in Solid-Propellant Rocket Motors,” *J. Propuls. Power*, vol. 5, no. 6, pp. 665–673, 1989.

[35] R. Acharya and K. K. Kuo, “Effect of Chamber Pressure and Propellant Composition on Erosion Rate of Graphite Rocket Nozzle,” *J. Propuls. Power*, vol. 23, no. 6, pp. 1242–1254, 2007.

[36] P. Thakre and V. Yang, “Chemical Erosion of Carbon-Carbon/Graphite Nozzles in Solid-Propellant Rocket Motors,” *J. Propuls. Power*, vol. 24, no. 4, pp. 822–833, 2008.

[37] D. Bianchi, F. Nasuti, M. Onofri, and E. Martelli, “Thermochemical Erosion Analysis for Graphite/Carbon-Carbon Rocket Nozzles,” *J. Propuls. Power*, vol. 27, no. 1, pp. 197–205, 2011.

[38] L. Kamps *et al.*, “Method for Determining Nozzle-Throat-Erosion History in Hybrid Rockets,” *J. Propuls. Power*, vol. 33, no. 6, pp. 1369–1377, 2017.

[39] D. Bianchi, L. Kamps, F. Nasuti, and H. Nagata, “Numerical and Experimental Investigation of Nozzle Thermochemical Erosion in Hybrid Rockets,” in *53rd*

AIAA/SAE/ASEE Joint Propulsion Conference, 2017.

[40] B. Evans, "Nozzle Erosion Characterization and Minimization For High-Pressure Rocket Motor Applications," Pennsylvania State University.

[41] D. Bradley, G. Dixon-Lewis, S. El-din Habik, and E. M. J. Mushi, "The Oxidation of Graphite Powder in Flame Reaction Zones," *Symp. Combust.*, vol. 20, no. 1, pp. 931–940, 1985.

[42] H. K. Chelliah, A. Makino, I. Kato, N. Araki, and C. K. Law, "Modeling of Graphite Oxidation in a Stagnation-Point Flow Field Using Detailed Homogeneous and Semiglobal Heterogeneous Mechanisms with Comparisons to Experiments," *Combust. Flame*, vol. 104, no. 4, pp. 469–480, 1996.

[43] B. R. Bird, W. E. Stewart, and E. N. Lightfood, *Transport Phenomena*, 2nd ed. New York, NY: John Wiley & Sons, Inc., 2001.

[44] E. R. Gilliland and T. K. Sherwood, "Diffusion of Vapors into Air Streams," *Ind. Eng. Chem.*, vol. 26, no. 5, pp. 516–523, 1934.

[45] W. L. McCabe, J. C. Smith, and P. Harriott, *Unit Operations of Chemical Engineering*, 7th Ed. Singapore: McGraw-Hill, 2005.

[46] K. Ozawa and T. Shimada, "Effects of O/F Shifts on Flight Performances of Vertically Launched Hybrid Sounding Rockets," in *53rd AIAA/SAE/ASEE Joint Propulsion Conference*, 2017.

[47] L. T. Kamps *et al.*, "Investigation of Graphite Nozzle Erosion in Hybrid Rockets

Using O2/C2H4," *2018 Jt. Propuls. Conf.*, pp. 1–24, 2018.

[48] F. Cauty and D. Gramer, "Solid-Fuel Pyrolysis Phenomena and Regression Rate, Part 2: Measurement Techniques," in *Fundamentals of Hybrid Rocket Combustion and Propulsion*, 2012, pp. 167–206.

[49] E. J. Wernimont and S. D. Heister, "Reconstruction Technique for Reducing Hybrid-Rocket Combustion Test Data," *J. Propuls. Power*, vol. 15, no. 1, pp. 128–136, 1999.

[50] H. Nagata, H. Nakayama, M. Watanabe, M. Wakita, and T. Totani, "Accuracy and Applicable Range of a Reconstruction Technique for Hybrid Rockets," *Adv. Aircr. Spacecr. Sci.*, vol. 1, no. 3, pp. 273–289, 2014.

[51] C. Carmicino and A. R. Sorge, "Influence of a Conical Axial Injector on Hybrid Rocket Performance," *J. Propuls. Power*, vol. 22, no. 5, pp. 984–995, 2006.

[52] H. NAGATA, Y. Saito, T. Ishiyama, Y. Inaba, M. Wakita, and T. Totani, "Evaluations of Data Reduction Methods for Hybrid Rockets," *65th Int. Astronaut. Congr.*, p. IAC-14,C4,2,3,x24415, 2014.

[53] L. Kamps and H. Nagata, "Estimation of Nozzle Throat Wall Temperature History in Hybrid Rockets," in *1st Hybrid Rocket Symposium*, 2018.

[54] Y. Saito, T. Uematsu, H. Isochi, M. Wakita, T. Totani, and H. Nagata, "Estimation of Hybrid Rocket Nozzle Throat Erosion History," *Trans. Japan Soc. Aeronaut. Sp. Sci. Aerosp. Technol. Japan*, vol. 14, no. ists30, p. Pa_145-Pa_151, 2017.

[55] L. Kamps, K. Sakurai, Y. Saito, and H. Nagata, “Comprehensive Data Reduction for N2O/HDPE Hybrid Rocket Motor Performance Evaluation,” *Aerospace*, vol. 6, no. 4, p. 45, 2019.

[56] R. C. Mehta, “Estimation of Heat-Transfer Coefficient in a Rocket Nozzle,” *AIAA J.*, vol. 19, no. 8, pp. 1085–1086, 1981.

[57] P. Narsai, E. Momanyi, K. Venkataraman, B. J. Evans, and B. J. Cantwell, “Indirect Heat Flux Measurements at the Nozzle Throat of a Hybrid Rocket Motor,” in *51st AIAA/SAE/ASEE Joint Propulsion Conference*, 2015.

[58] “ISOTROPIC GRAPHITE: Typical Properties.” [Online]. Available: https://www.tokaicarbon.co.jp/en/products/fine_carbon/pdf/Isotropic_graphite.pdf. [Accessed: 13-Jun-2018].

[59] A. I. Lutcov, V. I. Volga, and B. K. Dymov, “Thermal conductivity, electric resistivity and specific heat of dense graphites,” *Carbon N. Y.*, vol. 8, no. 6, pp. 753–760, 1970.

[60] A. T. D. Butland and R. J. Maddison, “The Specific Heat of Graphite: An Evaluation of Measurements,” *J. Nucl. Mater.*, vol. 49, pp. 45–56, 1973.

[61] W. S. Rasband, “ImageJ.” U.S. National Institutes of Health, Bethesda, MD, USA, 1997.

[62] R. Pasztor, “Richard Branson’s Space-Tourism Company Rockets Out of Atmosphere for First Time,” *The Wall Street Journal*, 2018.

[63] A. Takahashi and T. Shimada, “Essentially Non-Explosive Propulsion Paving a Way for Fail-Safe Space Transportation,” *Trans. Japan Soc. Aeronaut. Sp. Sci. Aerosp. Technol. Japan*, vol. 16, pp. 1–8, 2018.

[64] G. Story and J. Arves, “Flight Testing of Hybrid-Powered Vehicles,” in *Fundamentals of Hybrid Rocket Combustion and Propulsion*, 2007, pp. 553–592.

[65] M. Kobald *et al.*, “Sounding Rocket ‘HEROS’ - A Low-Cost Hybrid Rocket Technology Demonstrator,” no. July, pp. 1–26, 2017.

[66] M. KOBALD, C. SCHMIERER, U. FISCHER, K. TOMILIN, and A. PETRAROLO, “A Record Flight of the Hybrid Sounding Rocket HEROS 3,” *Trans. Japan Soc. Aeronaut. Sp. Sci. Aerosp. Technol. Japan*, vol. 16, no. 3, pp. 312–317, 2018.

[67] Y.-S. Chen and B. Wu, “Development of a Small Launch Vehicle with Hybrid Rocket Propulsion,” in *2018 Joint Propulsion Conference*, 2018, no. July, pp. 9–11.

[68] G. Zilliac, B. S. Waxman, A. M. Karabeyoglu, B. Cantwell, and B. J. Evans, “Peregrine Hybrid Rocket Motor Development,” in *50th AIAA/ASME/SAE/ASEE Joint Propulsion Conference*, 2014, pp. 1–17.

[69] H. Gamal, A. Matusiewicz, R. Magiera, D. Hubert, and L. Karolewski, “Design, Analysis and Testing of a Hybrid Rocket Engine with a Multi-Port Nozzle,” pp. 1–15, 2018.

[70] “HyImpulse.” [Online]. Available: https://www.hyimpulse.de/en/projects/3-

project-hyplox75. [Accessed: 30-Sep-2019].

[71] H. Nagata, M. Wakita, T. Totani, and T. Uematsu, “Development and Flight Demonstration of 5 kN Thrust Class CAMUI Type Hybrid Rocket,” *Trans. Japan Soc. Aeronaut. Sp. Sci. Aerosp. Technol. Japan*, vol. 12, no. ists29, p. Ta_1-Ta_4, 2014.

[72] L. Kamps and H. Nagata, “Tubular Equivalent Regression Rate in Hybrid Rockets with Complex Geometries,” *Trans. Japan Soc. Aeronaut. Sp. Sci. Aerosp. Technol. Japan*, 2019.

[73] A. Mazzetti, L. Merotto, and G. Pinarello, “Paraffin-based hybrid rocket engines applications: A review and a market perspective,” *Acta Astronaut.*, vol. 126, pp. 286–297, 2016.

[74] U. Manual, “H-IIA,” no. February, 2015.

[75] E. T. Jens, B. J. Cantwell, and G. S. Hubbard, “Hybrid Rocket Propulsion Systems for Outer Planet Exploration Missions,” *Acta Astronaut.*, vol. 128, pp. 119–130, 2016.

[76] E. T. Jens, A. C. Karp, S. Contadin, A. Conte, B. Nakazono, and D. Vaughan, “Development Testing of Hybrid Rocket Motors Using Classical Fuels for Interplanetary CubeSats,” no. July, pp. 1–16, 2017.

[77] E. T. Jens, A. C. Karp, J. Rabinovitch, A. Conte, B. Nakazono, and D. A. Vaughan, “Design of Interplanetary Hybrid CubeSat and SmallSat Propulsion Systems,” pp.

1–18, 2018.

[78] A. Karabeyoglu, E. Toson, and B. Evans, “Effect of ‘O/F Shift’ on Combustion Efficiency of Hybrid Rockets,” in *50th AIAA/ASME/SAE/ASEE Joint Propulsion Conference*, 2014.

[79] Y. Saito, M. Kimino, A. Tsuji, Y. Okutani, K. Soeda, and H. Nagata, “High Pressure Fuel Regression Characteristics of Axial-Injection End-Burning Hybrid Rockets,” *J. Propuls. Power*, vol. 35, no. 2, pp. 328–341, 2019.

[80] M. A. Hitt and R. A. Frederick, “Testing and Modeling of a Porous Axial-Injection, End-Burning Hybrid Motor,” *J. Propuls. Power*, vol. 32, no. 4, pp. 834–843, 2016.

[81] L. Kamps, Y. Saito, T. Viscor, T. Totani, and H. Nagata, “Feasibility Study on the Application of Hybrid Rockets as Onboard CubeSat Thrusters,” in *32nd International Symposium on Space Technology and Science*, 2019, pp. 1–10.